Meson spectroscopy in Large-N QCD

Dissertation

zur Erlangung des Doktorgrades der Naturwissenschaften
(Dr. rer. nat.) der Fakultät für Physik
der Universität Regensburg

vorgelegt von

Luca Castagnini

aus Ivrea, Italien

May 2015

Promotionsgesuch eingereicht an: 27.01.2015
Die Promotionsarbeit wurde angeleitet von Prof. Dr. Gunnar Bali.
Das Promotionskolloquium fand am 23.06.2015 statt.

Prüfungsausschuss:

Vorsitzender	Prof. Dr. Christian Schüller
1. Gutachter	Prof. Dr. Gunnar Bali
2. Gutachter	Prof. Dr. Meinulf Göckeler
weiterer	Prof. Dr. Milena Grifoni

Contents

1 Introduction

Quantum Chromodynamics (QCD) is the commonly accepted theory of strong interactions. It is formulated in terms of elementary fields (quarks and gluons), whose interactions obey the principles of a relativistic quantum field theory, with a non-abelian gauge invariance based on the $\mathrm{SU}(3)$ group. It is described in the continuum Minkowski space by the Lagrangian:

$$\mathcal{L} = \bar{\psi}_q^i \left(i\gamma^\mu D_\mu^{ij} - m_q \delta^{ij} \right) \psi_q^j - \frac{1}{4} F_{\mu\nu}^a F^{a\mu\nu} \tag{1.1}$$

where ψ_q^i denotes the quark field with colour index $i = 1, \ldots, 3$ and D_μ^{ij} is the covariant derivative:

$$D_\mu^{ij} = \delta^{ij}\partial_\mu + i g_s A_\mu^a t^{a,ij} \tag{1.2}$$

A_μ is the gauge (gluon) field, g_s is the coupling constant while the traceless Hermitian matrices t^a (for $a = 1, \ldots, 8$) are the generators of the Lie algebra $su(3)$ with the normalization $\mathrm{Tr}\,(t^a t^b) = \delta^{ab}/2$ and $[t^a, t^b] = i\, f^{abc} t^c$. Lastly, $F_{\mu\nu}^a$ is the non-Abelian field strength defined as

$$F_{\mu\nu}^a = \partial_\mu A_\nu^a - \partial_\nu A_\mu^a + g_s\, f_{abc} A_\mu^b A_\nu^c \tag{1.3}$$

The theory is characterised by gauge invariance, i.e. given an element of the $su(N)$ algebra $\omega(x)$ the theory is invariant under the local transformation,

$$\begin{aligned} \psi(x) &\to \psi'(x) = \omega(x)\psi(x) \\ \bar{\psi}(x) &\to \bar{\psi}'(x) = \bar{\psi}(x)\omega^{-1}(x) \\ A_\mu(x) &\to A'_\mu(x) = \omega(x) A_\mu(x) \omega^{-1}(x) + \frac{i}{g_s} \left(\partial_\mu \omega(x)\right) \omega^{-1}(x) \end{aligned} \tag{1.4}$$

Non-abelian gauge theories behave in a peculiar way: the interactions weaken at short distances, or, equivalently, large momentum transfers. This is due to the running of the coupling constant g_s^2 which becomes smaller than 1 for energies larger than 1 GeV. In this regime, and for even larger energies such as in high energy proton-proton collisions, the coupling constant is small and the perturbative approach becomes a reliable tool. At low energies, however, the running coupling becomes large; in this regime many features of QCD are determined by non-perturbative phenomena, like confinement and chiral symmetry breaking. For this reason, the theoretical derivation of low energy QCD properties must rely on non-perturbative methods.

The standard non-perturbative definition of QCD is based on lattice regularisation [1], which makes the theory mathematically well-defined and amenable to analytical as well as to numerical studies. Thanks to theoretical, algorithmic and computer-power progress, during the last decade many large-scale dynamical lattice QCD (LQCD) computations have been performed at realistic values of the physical parameters, allowing one to obtain numerical predictions in energy regimes otherwise inaccessible. Although *brute force* brings evidence that the QCD is indeed the correct theory of strong interactions, numerical results may not provide an analytical understanding of the theory.

A different approach to QCD was suggested by Gerard 't Hooft in [2] which consists of studying an $\mathrm{SU}(N)$ based QCD, where the number of colours N is taken to infinity and the coupling g is sent to zero, keeping the product g^2N, as well as the number of flavour n_f, fixed. In this limit one finds that the amplitudes for physical processes are determined by a particular subset of (planar) Feynman diagrams, while other diagrams are suppressed by powers of $1/N$. Due to these mathematical simplifications, the low-energy spectrum consists of stable meson and glueball states, and the scattering matrix becomes trivial. Ideally one would then study the physical $N = 3$ case expanding around the $1/N \to 0$ limit, however the 't Hooft limit has proven so far to be still too complicated to be solved analytically.

Another non-perturbative approach to low-energy properties of strongly coupled non-Abelian gauge theories is based on the conjectured correspondence between gauge and string theories [3–5]. During the last decade, many studies have employed techniques based on this correspondence, to build models which reproduce (at least qualitatively) the main features of the mesonic spectrum of QCD. Remarkably, the large-N limit plays a technically crucial role also in the context of these holographic computations: the correspondence relates the strongly coupled regime of a gauge theory with an infinite number of colors to the classical gravity limit of a dual string model in an anti-de Sitter spacetime, a setup that can be studied with analytical or semi-analytical methods.

In order to understand whether predictions derived from approaches relying on the large-N limit can be relevant for the physical case of QCD with $N = 3$ colors, it is crucial to estimate the quantitative impact of finite-N corrections. For this reason, several lattice studies have recently investigated the dependence on N of various quantities of

interest—including, for example, string tensions [6–8], the glueball spectrum [9, 10] or the finite-temperature equation of state [11–14]—in different $\mathrm{SU}(N)$ Yang-Mills theories (see [15] for a recent review on large N lattice results). These works revealed precocious scaling to the large-N limit: up to modest $\mathcal{O}(N^{-2})$ corrections even the $\mathrm{SU}(3)$ and $\mathrm{SU}(2)$ theories appear to be "close" to the large-N limit.

The purpose of the present work is to further expand this line of research: by studying with numerical simulations the light mesons in gauge theories based on different $\mathrm{SU}(N)$ groups, we extract the dependence on the number of colors. In the past, only the pion and rho meson masses were studied in the large N limit [16–20]; while most of these works report a rho mass close to the real-world QCD, the authors of [20] found a rho mass which is approximately twice as large. To clarify this discrepancy, we extend the analysis by going to lighter quark masses, larger N, larger volumes and by increasing the statistics and the number of interpolators used to create a meson state.

Part of this work has been published in [21–23]. The results presented here include important improvements, namely the continuum limit extrapolation of the meson spectrum and the computation of non-perturbative large-N renormalization constants. This allow us to further restrict our systematic errors and to predict further quantities like the chiral condensate.

In chapter 2 we show how the large-N counting rules associated with the 't Hooft limit of QCD entail many phenomenological implications, providing intuitive explanations for poorly understood features of the real-world theory with $N = 3$ color charges. Lattice QCD is then formulated in chapter 3 where we explain in detail the methods used in this work. In chapters 4 and 5 we show the results of our simulations, first focusing for each particle mass on its dependence on the quark mass, then presenting the large-N meson spectrum with a discussion on systematic errors and continuum limit extrapolation. We conclude with a comparison between our results and those of other large-N approaches in chapter 6.

2 Phenomenology of large-N QCD

2.1. A simple example, the ϕ^4 theory

In order to easily understand the simplifications occurring in the large N limit, we first examine the $\mathrm{O}(N)$ version of the toy-model ϕ^4 theory, described by the Lagrangian,

$$\mathcal{L} = \frac{1}{2}\partial_\mu \phi_a \partial^\mu \phi_a - \frac{1}{2}m^2 \phi_a \phi_a - \frac{1}{8}g^2 \left(\phi_a \phi_a\right)^2 \tag{2.1}$$

where we have N scalar fields ϕ_a ($a = 1, \ldots, N$) and the sum over the repeated a-indexes is implied. In the standard perturbation theory approach, one would choose a regime where the coupling is small, evaluate the contribution of the leading Feynman diagrams and study the quantities as an expansion of g^2. In fig. 2.1 we show the first diagrams up to g^4 of a $2 \to 2$ scattering amplitude.

For fixed initial and final fields ϕ_a and ϕ_b, the central diagram in fig. 2.1 will appear N times more often than the other two, due to the extra free choice in the loop index c. If one studies the theory in a particular limit where N is taken to infinity and g^2 to zero, while keeping the product $\lambda = g^2 N$ finite, the diagram in fig. 2.1-c become $1/N$ suppressed with respect to the first two diagrams, so that in the large-N limit it can simply be ignored. A similar approach can be employed for QCD where g^2 is the running coupling, N is the number of colours and λ is commonly known as the 't Hooft parameter. In the case of QCD, as we show below, the theory becomes much simpler and only a special class of diagrams survives, however large-N QCD is far from trivial and has not been analytically solved yet.

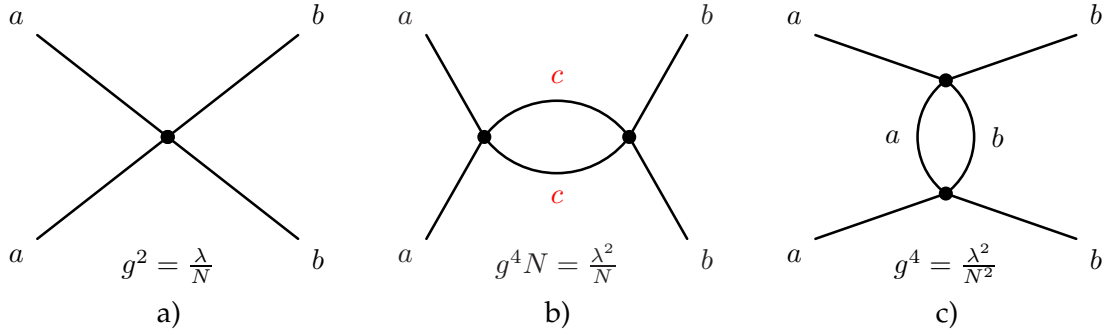

Figure 2.1.: Three possible $\mathcal{O}(g^2)$ Feynman diagrams for a given couple of input/output fields ϕ_a and ϕ_b. The diagram in the center occurs N times, due to the free index c.

2.2. The double-line notation

Although large-N QCD is far from been analytically solved, one can say a lot about its phenomenology just by studying the type of diagrams that survive. In order to simplify the discussion, we rescale the gluon and fermion fields as,

$$A_\mu \to \frac{1}{g} A_\mu, \quad ; \quad \psi \to \sqrt{N}\psi \quad ; \quad \not{D} \to \gamma_\mu \left(\mathbb{1}\partial^\mu + iA^\mu\right) \tag{2.2}$$

so that the Lagrangian of one flavour QCD reads,

$$\mathcal{L} = N\left[-\frac{1}{4\lambda} F^a_{\mu\nu} F^a_{\mu\nu} + \bar{\psi}(i\not{D} - m)\psi\right] \tag{2.3}$$

where the 't Hooft parameter $\lambda = g^2 N$ assumes the role of the coupling. Since the gluon fields carry two colour indexes, counting powers of N might become confusing in very complicated diagrams. One way to solve this problem is introducing the double-line notation, which is, one draws graphs with one line per colour index rather than per particle. In a gluon-fermion vertex (see fig. 2.2), the gluon is thus replaced by two lines that are attached to the single fermion line with which they interact.

In order to establish which diagrams survive and which ones are suppressed, we need to count the powers of N associated to them. For any complicated diagram, each vertex carries a factor N due to the coupling and for each propagator we have a factor $1/N$. With the double line notation, we can easily count the closed colour loops, to each of which a factor N is associated, due to the free choice of the internal colour index (see figs. 2.3-2.4). Let us examine a generic vacuum diagram, i.e. a diagram with no external legs, like those of fig 2.3. We can think of such a diagram as a surface made of polygons,

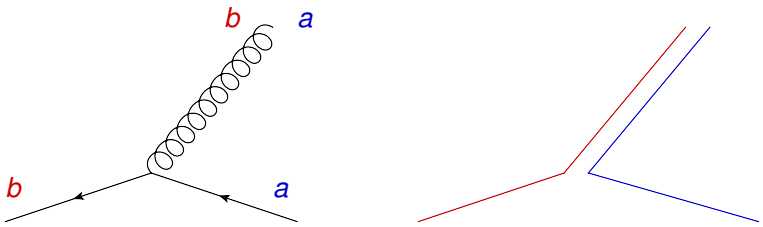

Figure 2.2.: Double line notation for a fermions-gluon vertex. The gluon carries two color indexes.

which correspond to the colour loops, whose edges (E) and vertexes (V) cut the surface into many faces (F). The total N factor carried by such a diagram will thus be:

$$N^{F+V-E} = N^{\chi}. \tag{2.4}$$

χ is the well known Euler characteristic, it is a topological invariant and does not depend on the way we cut the surface.

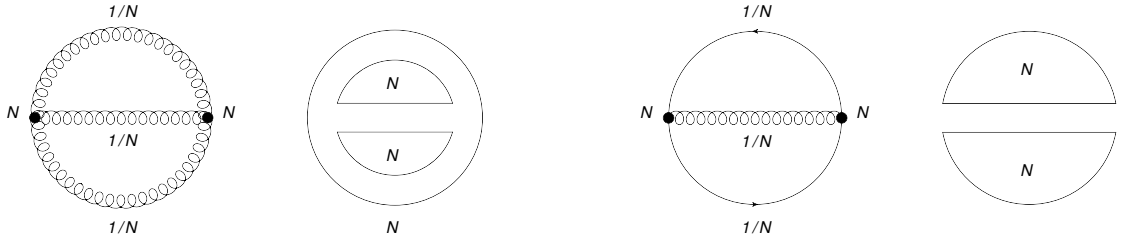

Figure 2.3.: Double line notation for a gluonic (left) and fermionic (right) excitation of the vacuum. The former is proportional to N^2 while the latter to N.

Generally any complicated surface can be thought as a sphere with some handles (H) and some holes (or boundaries, B) and its characteristic reads,

$$\chi = 2 - 2H - B. \tag{2.5}$$

It is then clear that the maximum value of χ is 2, corresponding to a sphere, and the leading diagrams in the large-N limit will be those $\propto N^2$, or, which is equivalent, those diagrams that can be drawn on the surface of a sphere without intersection of the lines (planar diagrams). In figs. 2.3 and 2.4 one can see how a fermionic loop correspond to a hole in the surface, i.e. one face is missing ($B = 1$) with respect to a gluon loop. This is particularly important, it means that any insertion of a fermionic loop in a given

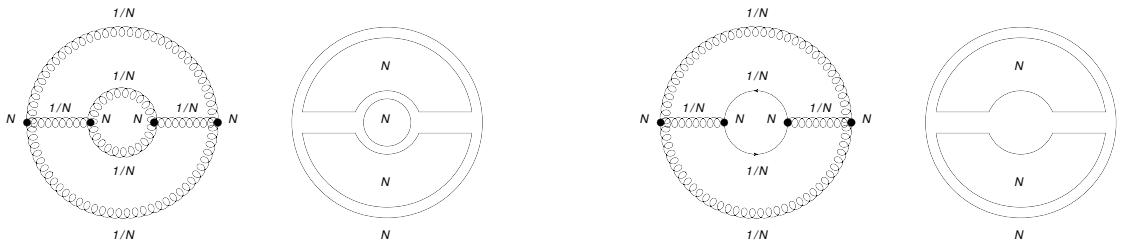

Figure 2.4.: One loop correction to a vacuum diagram. The insertion of a fermion loop (right) is $1/N$ suppressed with respect to a pure gluonic loop (left).

diagram is suppressed by a factor $1/N$. In other words, the large-N QCD is a theory where all internal quark loops can be ignored as long as the number of flavour n_f is kept fixed, or, in lattice terms, the theory is quenched. One can still analyse diagrams with fermionic lines (for instance, when studying mesons) but they will be present only at the external boundaries.

2.3. Mesons and glueballs

So far we described only vacuum diagrams, however all the considerations hold when we study mesons and glueballs. The diagrams involved are similar to the leading vacuum-to-vacuum diagrams of fig. 2.3, where the glueball and meson operators appear as insertions on the external lines. In particular the leading diagrams for pure gluonic processes are constructed from gluonic vacuum-to-vacuum diagrams and carry a N^2 factor, while processes involving quarks will be constructed from the leading fermionic vacuum-to-vacuum diagrams, which carry a factor N.

In order to describe the behaviour of mesons and glueballs, we first introduce a generating functional Z_J, which depends on the QCD Lagrangian $\mathcal{L} = N\tilde{\mathcal{L}}$ given in eq. (2.1) and on operators O_a which create the desired states,

$$Z_J = \int \mathcal{D}A\mathcal{D}\overline{\psi}\mathcal{D}\psi \exp\left\{ iN \int \mathrm{d}^4\mathrm{x} \left(\tilde{\mathcal{L}}[\mathrm{A}, \psi, \overline{\psi}] + \mathrm{JO} \right) \right\}. \tag{2.6}$$

We can construct a generic correlator by the use of functional derivatives,

$$\langle O_1 \dots O_n \rangle = (iN)^{-n} \frac{\delta}{\delta J_1} \dots \frac{\delta}{\delta J_n} \ln Z_J \Big|_{J=0}, \tag{2.7}$$

where $O_i = O(x_i)$ and $J_i = J(x_i)$. For example an n-points function of pure gluonic operators G_i will go as,

$$\langle G_1 \dots G_n \rangle \propto N^{2-n} \tag{2.8}$$

As a consequence, in the 't Hooft limit glueballs are stable objects and processes that involve a glueball decaying into other glueballs or mesons are suppressed.

Mesons are states usually created on the vacuum by bilinear operators $B_i = \bar{\psi}\Gamma_i\psi$, however these operators are ill-defined, since the leading fermionic vacuum diagrams are only $\propto N$, so that in the large-N limit a two-point function would be,

$$\langle B_1 B_2 \rangle \propto N^{1-2=-1} \xrightarrow[N\to\infty]{} 0. \tag{2.9}$$

To avoid this problem, we use the operator $\tilde{B}_i = \sqrt{N} B_i$ and the n-point meson correlators become,

$$\langle \tilde{B}_1 \dots \tilde{B}_n \rangle \propto N^{(2-n)/2} \tag{2.10}$$

which means that interactions between 3 or more mesons are suppressed by powers of $1/\sqrt{N}$. A similar conclusion could be drawn from correlators of mesons and glueballs, thus we can say that in the $N \to \infty$ limit QCD consists of stable non-interacting mesons and glueballs, while at large (but finite) N-values QCD is a theory of weekly interacting hadrons.

Another interesting phenomenological property of the 't Hooft limit is that the Okubo, Zweig and Iizuka (OZI) rule becomes exact when $N \to \infty$. This rule states that processes associated to diagrams which can be divided into two sets of quark lines by cutting only gluon lines are suppressed. These processes involve the annihilation and creation of quarks, thus at least two quark loops must be involved and the amplitude obtains an extra $1/N$ factor with respect to processes which have only one quark loop (see fig. 2.5).

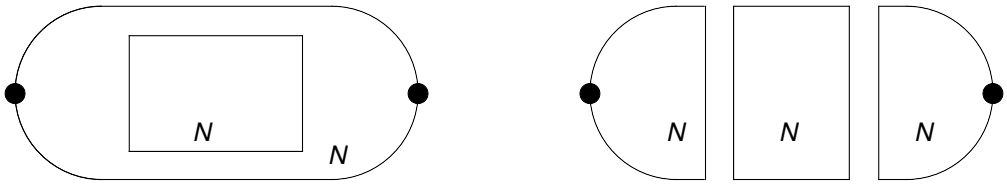

Figure 2.5.: OZI rule. The diagram at the left goes into a stage where only gluon appear and is suppressed by a factor $1/N$.

2.4. Baryons

Baryons are colourless observables (i.e. they are in a completely antisymmetrised color state) made of N quarks,

$$\epsilon_{i_1,\dots,i_N} q^{i_1} \dots q^{i_N}. \tag{2.11}$$

For this reason, diagrams involve a number of lines increasing with N and drawing them becomes impossible in the 't Hooft limit. Nonetheless, one can derive a few scaling laws, as initially indicated by Witten in [24]. One can imagine to split a generic baryon diagram into two parts, one made of n interacting quark lines and one of $N-n$ freely propagating quarks (fig. 2.6). The part with n interacting quarks can be thought

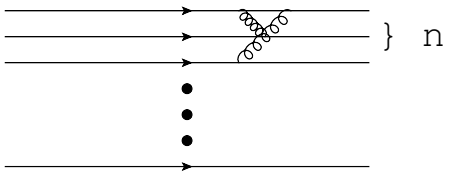

Figure 2.6.: A baryon interaction with an n-lines connected component.

of as the result of breaking open n quark lines into a vacuum-to-vacuum graph, which is proportional to N. Since the baryon must be in a total antisymmetric color state, each of the n lines must carry a different color, i.e. for each quark cut we loose a sum over color and thus a generic n-body diagram will be of order N^{1-n}. Nonetheless, there are $\mathcal{O}(N^n)$ ways to choose n quarks from a N-quark baryon, so that the net effect of an n-body interaction is of order N. We can think that the total energy of a baryon receives contributions from the mass of the constituent quarks, their kinetic energies and from the quark interactions, all of which scale as $\mathcal{O}(N)$ too. Baryons in the large-N limit thus become infinitely heavy objects and the usual way to study them is to treat them as non-relativistic bound states of weakly interacting quarks[1]. In this approximation each quark moves independently in a common background potential resulting from the interaction with all the other quarks in the baryon (see [25,26]) and it can be shown that baryon-baryon scattering is of $\mathcal{O}(N)$ while baryon-meson scattering is of $\mathcal{O}(1)$.

More refined models [27,28] result in a prediction on the masses of baryons of different spin J which should match those described in terms of a rotor spectrum,

$$M = c_1 N + c_2 \frac{J(J+1)}{N}. \tag{2.12}$$

This has been recently verified on the lattice in [29] for $N = 3, 5, 7$.

[1] Unfortunately, an elegant relativistic formalism has not yet been found or developed.

3
QCD on the lattice

3.1. Introduction to lattice QCD

The lattice is a mathematical tool that provides a natural cut-off (the lattice spacing) to remove the ultraviolet infinities that we get in quantum field theory. Physical quantities can be extracted from the lattice only in the continuum limit, where the lattice spacing is taken to zero. By virtue of asymptotic freedom, this can be done easily in lattice simulations, as the coupling constant is an input parameter, and we can force it to take smaller and smaller values, corresponding to a finer and finer lattice spacing. Even if we cannot directly set the coupling constant to zero we can make a fit and extrapolate the physical quantities to their continuum limits.

The lattice formulation emphasizes the close connection between field theory and statistical mechanics and makes it possible to use statistical simulation methods, usually called Monte Carlo programs, to "measure" physical quantities. In this chapter we discuss how to formulate QCD on the lattice, while in the next one we discuss our simulations.

3.2. The connection between quantum field theory and statistical mechanics

In a quantum field theory the Feynmann path integral formulation makes it possible to define a "generating functional Z" as:

$$Z[J] = \int \mathcal{D}\phi \, e^{i \int dt \int d^3x \mathcal{L}(\phi) + J\phi} \tag{3.1}$$

The standard way to obtain n-point Green functions of the theory is by differentiating $\log Z[J]$ with respect to J, as already done in eq. (2.7). If we imagine the Z function as a "sum" over every configuration of the field ϕ, we immediately recognise the analogy to the usual expression of the partition function of the canonical ensemble:

$$Z = \sum_{\{\phi\}} e^{-\beta H[\phi]}, \tag{3.2}$$

the only difference being that here we have a real weight in the exponential, while above we had an oscillatory term. We can bridge this difference with an analytic continuation of the QFT Z function to imaginary values of the time. This is the well known "Wick rotation" ($x_0 \to ix_4$) that leads to the Euclidean form of the action S_E and the Z function becomes:

$$Z[J] = \int \mathcal{D}\phi e^{-S_E[\phi] + \int d^4x J(x)\phi(x)} \tag{3.3}$$

Introducing a discrete spacetime (the lattice), made of N_μ nodes separated by a lattice spacing "a" in each direction μ, it is possible to map consistently quantum field theory and statistical field theory with the use of the following identifications:

QFT	Statistical Mechanics
Functional integral: $\int \mathcal{D}\phi$	Partition function $\sum_{conf}$
Euclidean action	Hamiltonian
Energy of the vacuum	Free energy
Green functions $\langle 0\|T[\mathcal{O}_1...\mathcal{O}_n]\|0\rangle$	Correlators: $\langle \mathcal{O}_1...\mathcal{O}_n\rangle$
Mass M	Correlation length $\xi = 1/M$
Regularization cut-off : Λ	inverse lattice spacing a^{-1}
Renormalization: $\Lambda \to \infty$	Continuum limit: $a \to 0$

Each field of the continuum theory can be mapped to the lattice as,

$$\begin{array}{lcr} \text{scalar} & \to & \text{node} \\ \text{vector} & \to & \text{link} \\ F_{\mu\nu} & \to & \text{plaquette.} \end{array}$$

Lastly, we need a way to introduce the temperature. The partition function of a statistical field theory is given by:

$$Z = \sum_{\{\phi\}} \langle \phi | e^{-\beta \hat{H}} | \phi \rangle = \text{Tr}\left(e^{-\beta \hat{H}}\right), \tag{3.4}$$

where β is the inverse of the physical temperature. If we impose periodic (antiperiodic) boundary[1] conditions in the temporal direction for bosonic (fermionic) fields on the

[1] The antiperiodic boundary conditions are necessary for fermion fields due to an extra minus sign in the definition of the trace of eq. (3.4), as shown in appendix A.

lattice,

$$\langle \phi_2 t_2 | \phi_1 t_1 \rangle \equiv \langle \phi_2 | e^{-i(t_2-t_1)\hat{H}} | \phi_1 \rangle \longrightarrow \int d\phi \langle \phi | e^{-i(t_2-t_1)\hat{H}} | \phi \rangle \tag{3.5}$$

we can identify the lattice size in the temporal direction with the inverse of temperature:

$$i(t_2 - t_1) = (\tau_2 - \tau_1) = N_t\, a \to \beta \tag{3.6}$$

with N_t being the lattice size in the temporal directions in units of the lattice spacing a. Using natural units we can then identify:

$$T = \frac{1}{N_t\, a} \tag{3.7}$$

For practical reasons, in a lattice simulation one imposes periodic boundary conditions in all the d directions, taking care of choosing lattice extensions much larger than typical correlation lengths of the theory, so as to make the effect of the boundary conditions negligible. In our work we study the meson masses in the limit of zero temperature, which would require $T \to 0$. In practice, we employ a temporal extension twice as large as the spatial extension $N_t = 2N_s$ and we check that the finite size effects are negligible (see section 4.9), thus demonstrating that the $T = 0$ limit is effectively reached.

3.3. Yang-Mills theories on the lattice

We split the description of how to reproduce QCD on the lattice in two parts, one related to the fermionic action and the other, described in this section, related to the gluonic one. One can pass from the elements of the algebra to the elements of the gauge group $\mathbf{G}$ by introducing on every link n_μ the gauge fields:

$$U_\mu(n) \approx e^{i\, a\, g\, A_\mu(n)} \tag{3.8}$$

that are the parallel transporters of the theory, i.e. they connect two different reference frames in the internal space of the theory, E_n and $E_{n+\widehat{\mu}}$, which are defined at two different points. For consistency, we must impose:

$$U_{-\mu}(n + \widehat{\mu}) = U_\mu^{-1}(n) = U_\mu^\dagger(n). \tag{3.9}$$

In this framework a gauge transformation $V(n) \in \mathbf{G}$ acting on E changes a scalar field as in the continuum,

$$\psi(n) \to V(n)\, \psi(n), \tag{3.10}$$

while the gauge field $U_\mu(n)$ transforms as,

$$U_\mu(n) \to V(n)\, U_\mu(n)\, V^{-1}(n + \widehat{\mu}) \tag{3.11}$$

in order to leave the product $\bar{\psi}(n)U_\mu(n)\psi(n+\widehat{\mu})$ gauge invariant. In this way, eqs. (3.10)-(3.11) can be seen as the lattice equivalent of the continuum expression eq. (1.4).

Another gauge invariant observable can be built out of the gauge variables $U_\mu(n)$ by defining the trace of the path-ordered product of the $U_\mu(n)$'s around a closed path γ ("Wilson loop"); the simplest such paths are the elementary squares $U_{\mu\nu}$ ("plaquettes") on the lattice:

$$W = \mathrm{Tr}\, U_{\mu\nu} \tag{3.12}$$

where we define:

$$U_{\mu\nu} = U_\mu(n)U_\nu(n+\widehat{\mu})U_{-\mu}(n+\widehat{\mu}+\widehat{\nu})U_{-\nu}(n+\widehat{\nu}). \tag{3.13}$$

To construct the action we sum over all the plaquettes of the lattice:

$$\frac{1}{2}\sum_{n,\mu,\nu} \mathrm{Tr}\, U_{\mu\nu}(n) = \sum_{\square} \mathrm{Re}\,\mathrm{Tr}\, U_{\mu\nu}(n).$$

What we get is a real quantity, because every link is counted with both orientation ($\mathrm{Tr}\,(U + U^\dagger) \in \mathbf{R}$). Notice that since the sum over μ and ν is unrestricted all the plaquettes are counted twice. This is why we put the factor $1/2$ in front of the sum or, alternatively, we just write $\sum_\square$.

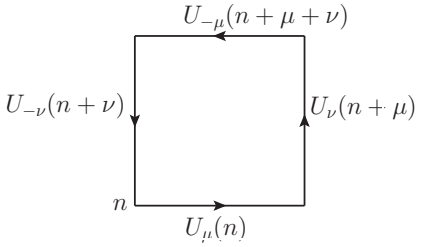

Figure 3.1.: The simplest Wilson loop: the plaquette.

We can formulate the "Wilson action" for a generic $\mathrm{SU}(N)$ gauge group as:

$$S_W = \beta\sum_{\square}\left(1 - \frac{1}{N}\mathrm{Re}\,\mathrm{Tr}\, U_{\mu\nu}(n)\right). \tag{3.14}$$

By defining the discretized lattice derivative as:

$$\nabla_\mu f(x) \equiv \frac{f(n+\widehat{\mu}) - f(n)}{a}, \tag{3.15}$$

which in the limit $a \to 0$ reduces to $\partial_\mu f(x)$, and by using the Baker-Hausdorff formula[2] it is possible[3] to expand $U_{\mu\nu}$ up to $O(a^2)$ terms,

$$U_{\mu\nu}(n) \sim e^{ia(\nabla_\mu A_\nu(n) - \nabla_\nu A_\mu(n) - [A_\mu(n), A_\nu(n)])} \equiv e^{ia^2\, g\, F_{\mu\nu}(n)}. \tag{3.16}$$

[2] At first order the Baker-Hausdorff reads $e^x e^y = e^{x+y+\frac{1}{2}[x,y]+\ldots}$

[3] A step by step calculation can be found in [30]

The exponential can in turn be expanded, however the linear term in $A_\mu \equiv t_a\, A^a_\mu$ cancels due to the trace $\mathrm{Tr}(t_a) = 0$ so that the first term of the Wilson action reads,

$$S_W = \frac{\beta\, a^4 g^2}{8\, N} \sum_{n,\mu\nu} F^i_{\mu\nu}(n) F^{i\,\mu\nu}(n) + O(a^6) \tag{3.17}$$

This reproduces in the continuum limit the standard Yang-Mills action after identifing,

$$\sum_n \to \int \frac{d^d x}{a^d} \quad ; \quad \beta = \frac{2N}{a^{4-d} g^2} \tag{3.18}$$

3.4. Fermions on the lattice

The discretization of the fermionic action is more subtle. Starting with the simplest formulation of the free continuum action,

$$S = \int \mathrm{d^4x}\, \overline{\psi}(\mathrm{x})\, (\mathrm{i}\gamma^\mu \partial_\mu - \mathrm{m})\, \psi(\mathrm{x}), \tag{3.19}$$

we can write an equivalent action on the lattice by introducing a discretised derivative,

$$\partial_\mu \psi(x) = \frac{\psi(x + a\hat{\mu}) - \psi(x - a\hat{\mu})}{2a} \tag{3.20}$$

that leads to the naïve fermion action,

$$S = a^4 \sum_{i,j} \overline{\psi}(i) D(i|j) \psi(j) = a^4 \sum_{i,j} \overline{\psi}(i) \left[\frac{1}{2a} \sum_\mu \gamma_\mu \left(\delta_{i+\hat{\mu},j} - \delta_{i-\hat{\mu},j}\right) - m \right] \psi(j) \tag{3.21}$$

$D(i|j)$ is a lattice Dirac operator and γ are the Euclidean version of the Minkowski gamma matrices:

$$\gamma_0^E = \gamma_0^M \quad ; \quad \gamma_i^E = -i\gamma_i^M \quad ; \quad \{\gamma_\mu^E, \gamma_\nu^E\} = \delta_{\mu,\nu}. \tag{3.22}$$

Using Wick's theorem, we can compute any correlation function in terms of the inverse of the Dirac operator,

$$\left\langle \psi(i) \overline{\psi}(j) \right\rangle = D^{-1}(i|j) \tag{3.23}$$

In momentum space the free Dirac operator can be written as,

$$\tilde{D}(p|q) = \delta(p-q) \tilde{D}(p) \tag{3.24}$$

$$\tilde{D}(p) = m\mathbb{1} + \frac{i}{a} \sum_\mu \gamma_\mu \sin\left(p_\mu a\right) \tag{3.25}$$

and its inverse becomes,

$$\tilde{D}^{-1}(p) = \frac{m\mathbb{1} - ia^{-1}\sum_\mu \gamma_\mu \sin(p_\mu a)}{m^2 + a^{-2}\sum_\mu \sin(p_\mu a)^2}. \tag{3.26}$$

This expression reproduces the continuum propagator when $a \to 0$, but a problem arises if we consider the case of massless fermions $m = 0$ (chiral limit). In this case in fact, together with the correct pole in $p = (0,0,0,0)$, which is the one expected in the continuum, we have also other 15 unwanted poles (called doublers) within the fundamental Brillouin domain when $p = (\pi/a, 0, 0, 0), \ldots, (\pi/a, \pi/a, \pi/a, \pi/a)$.

A famous no-go theorem by Nielsen and Ninomiya proves that the doublers are unavoidable for a lattice Dirac operator D that satisfies the chiral symmetry

$$\{D^{-1}, \gamma_5\} = 0 \quad \text{for} \quad m = 0 \tag{3.27}$$

and which is ultralocal (i.e. the action only involves couplings between fields localized in a spacetime region). In this work we fix this problem in the way proposed by Wilson: adding to the Dirac operator a term which breaks chiral simmetry but cancels the doublers:

$$\tilde{D}(p) \;=\; m\mathbb{1} + \frac{i}{a}\sum_\mu \gamma_\mu \sin(p_\mu a) + \mathbb{1}\frac{1}{a}\sum_\mu (1 - \cos(p_\mu a)). \tag{3.28}$$

The effect of the extra term is to replace the mass m in eq. (3.26) with a momentum dependent mass $m(p)$,

$$m(p) = m + \frac{2}{a}\sum_\mu \sin^2\left(\frac{p_\mu a}{2}\right), \tag{3.29}$$

so that in the continuum limit the doublers become infinitely heavy and decouple from the theory. The price to pay however is that in order to recover the chiral limit a fine tuning of the mass is required.

So far we discussed only the free fermionic action. In the continuum the prescription to introduce the interaction with the gauge fields is to replace the derivative ∂_μ with the covariant derivative $D_\mu = \partial_\mu + igA_\mu(x)$. On the lattice this is implemented as,

$$D_\mu\psi(x) = \frac{U_\mu(x)\psi(x+\hat{\mu}) - U_{-\mu}(x)\psi(x-\hat{\mu})}{2} \tag{3.30}$$

so that the complete Wilson action and operator for fermions, with explicit spin-colour

indexes[4], can be rewritten as,

$$S_f^W = a^4 \sum_{i,j,a,b,\alpha,\beta} \overline{\psi}_\alpha^a(i) D^W_{\substack{\alpha\,\beta \\ a\,b}}(i|j) \psi_\beta^b(j) \tag{3.31}$$

$$D^W_{\substack{\alpha\,\beta \\ a\,b}}(i|j) = \left(m + \frac{4}{a}\right) \delta_{a,b}\delta_{\alpha,\beta}\delta_{i,j} - \frac{1}{2a} \sum_{\mu=\pm1}^{\pm4} (\mathbb{1} - \gamma_\mu)_{\alpha\beta} U_\mu(i)_{a,b} \delta_{i+\hat{\mu},j}. \tag{3.32}$$

The parameter m is traditionally set into lattice programs in the form of the hopping parameter κ,

$$\kappa = \frac{1}{2(a\,m + 4)} \tag{3.33}$$

which is related to the bare quark mass m_q via:

$$a m_q = \frac{1}{2}\left(\frac{1}{\kappa} - \frac{1}{\kappa_c}\right). \tag{3.34}$$

κ_c denotes the critical value, corresponding to a massless quark. The additive constant is given by $\kappa_c^{-1} = 8 + \mathcal{O}(\beta^{-1})$ and its non-perturbative determination is discussed in section 4.2.

3.5. The quenched approximation

In constructing the generating funtional Z we have to address the problem of the integration measure. The integrals involved in the construction of Z are site by site (or better, in the case of a gauge theory, link by link) ordinary integrals (or integrals over Grassmann variables in the case of fermions). For the links we have a natural choice for the integration measure: the Haar measure, i.e. the invariant measure over the group manifold $dU_\mu(n)$. An important consequence of this is that, since the integration is made over the whole group manifold *all* the gauge equivalent configurations are automatically included in the sum. So, as opposed to the continuum case, on every finite lattice the integration over the pure gauge degrees of freedom does not make quantum averages ill defined: in the lattice formulation there is no need to fix a gauge.

To summarize the parts discussed in the previous sections, we can write:

$$Z = \int \left(\prod_{n,\mu} dU_\mu(n)\right) \left(\prod_n d\psi(n)\right) \left(\prod_n d\overline{\psi}(n)\right) e^{-S_g[U] - S_f[U,\psi,\overline{\psi}]} \tag{3.35}$$

[4]We use latin and greek letters respectively for colour and spin indexes.

and we can perform the integration over the Grassmann variables (see appendix A), reducing the partition function to,

$$Z = \int \left(\prod_{n,\mu} dU_\mu(n) \right) \det(D_W[U])\, e^{-S_g[U]}. \tag{3.36}$$

The determinant above is the only term that includes information on the quark dynamics, thus it is responsible for the contribution of the fermionic loops. Unfortunately, the Dirac operator is a large matrix and the computation of its determinant is computationally expensive. One possibility is to simply neglect this term, the so called quenched approximation, by setting $\det(D_W) = 1$. This is equivalent to assuming an infinite mass for the valence quarks and, as we have already seen, is the correct choice for the large-N limit.

3.6. Monte Carlo simulations

Although the lattice formulation reduces path integrals to multidimensional ordinary integrals, an attempt to numerically evaluate the partition function fails due to thigh dimensionality of the problem. The goal of the Monte Carlo approach is to provide a small number of configurations which are typical of the thermal equilibrium of the system, as the partition function at the thermal equilibrium is strongly dominated by only a very small subset of configurations which are the most likely ones.

A Monte Carlo program starts with some initial configuration of the fields stored in the computer memory and then sequentially makes pseudo-random changes on these variables in such a manner that the probability density for encountering any configuration C is proportional to the Boltzmann factor:

$$p(C) \propto e^{-\beta S(C)}, \tag{3.37}$$

where $\beta S(C)$ is the action associated with the given configuration. In this way one can generate a sequence of n_c configurations that forms an ergodic trajectory over the phase space and at the thermal equilibrium one can substitute the canonical ensemble mean with an arithmetic mean over configurations:

$$\langle \mathcal{O} \rangle = \frac{\int \mathcal{D}U \mathcal{O}(U)\, e^{-\beta S(U)}}{Z} \equiv \lim_{n_c \to \infty} \frac{1}{n_c} \sum_{i}^{n_c} \mathcal{O}(C_i) \tag{3.38}$$

In order to have a correct estimate of the errors, one needs to average the measurements over a set of thermalised and uncorrelated configurations. We applied the techniques explained in detail in appendix B to generate ensembles of configurations for each $\mathrm{SU}(N)$ gauge group, volume and lattice spacing. We based most of our code on the Chroma suite [31], which we have adapted to work for a generic N.

3.7. Meson correlators

We use bilinears of the form,

$$B = \overline{u}\Gamma d \tag{3.39}$$

as operators which reproduce the iso-triplet meson spectrum for an appropriate choice of Γ, as summarized in table 3.1.

Particle	π	ρ	a_0	a_1	b_1
Bilinear	$\bar{u}\gamma_5 d$	$\bar{u}\gamma_i d$	$\bar{u}d$	$\bar{u}\gamma_5\gamma_i d$	$\frac{1}{2}\epsilon_{ijk}\bar{u}\gamma_i\gamma_j d$
J^{PC}	0^{-+}	1^{--}	0^{++}	1^{++}	1^{+-}

Table 3.1.: List of the studied channels and their bilinear operators used in the correlation functions.

After performing the Wick contractions, we can express the meson correlators in terms of single quark propagators:

$$\begin{aligned}
\langle B(x)\overline{B}(y)\rangle &= \left\langle \overline{d}(x)\Gamma u(x)\overline{u}(y)\Gamma(y)\right\rangle && (3.40)\\
&= \Gamma_{\alpha\beta}\Gamma_{\delta\epsilon}\left\langle \overline{d}^a_\alpha(x)u^a_\beta(x)\overline{u}^b_\delta(y)d^b_\epsilon(y)\right\rangle \\
&= -\Gamma_{\alpha\beta}\Gamma_{\delta\epsilon}\left\langle u^a_\beta(x)\overline{u}^b_\delta(y)\right\rangle\left\langle d^b_\epsilon(y)\overline{d}^a_\alpha(x)\right\rangle \\
&= -\Gamma_{\alpha\beta}\Gamma_{\delta\epsilon}D_u^{-1}(x|y)\;{}^{\beta\,\delta}_{a\,b}\;D_d^{-1}(y|x)\;{}^{\epsilon\,\alpha}_{b\,a} \\
&= -\mathrm{Tr}\left(\Gamma D_u^{-1}(x|y)\Gamma D_d^{-1}(y|x)\right) && (3.41)
\end{aligned}$$

In this study, we discard iso-singlet operators like $(\overline{u}\Gamma u + \overline{d}\Gamma d)/\sqrt{2}$, as the Wick contractions produce disconnected pieces (i.e. terms proportional to $\mathrm{Tr}\,(\Gamma D^{-1})$) which are very noisy and are known to require much more statistics.

In addition, we use degenerate quark masses, i.e. $m_u = m_d$, which leads to a further simplification: if $D_d^{-1} = D_u^{-1}$ in fact, we can use the property,

$$\gamma_5 D^{-1}(x|y)\gamma_5 = \left(D^{-1}(y|x)\right)^\dagger \tag{3.42}$$

so that only one of the two propagators of eq. (3.41) needs to be computed.

3.8. Point sources

Ideally one would evaluate eq. (3.41) for each couple of $(x|y)$ points and average over the appropriate $x - y$ distances. This would require to invert the complete Dirac operator, a large sparse matrix, resulting into what is generically called *all-to-all* propagator.

Unfortunately this matrix scales like the volume squared (and, in our case, also like N^2) and the inversion becomes computationally too expensive, both from a memory and from a computer-time perspective. While some techniques exist to estimate *all-to-all* propagators, the simplest solution is to fix the source x to a single value of coordinates x_0, so that one deals with *point-to-all* propagators, and to replace the average over all source points with just one single source point. This approach still leads to the correct result for the correlators once the average over many configurations is performed. With this trick, the cost of the inversion scales only like the volume and the computations become feasible.

From the numerical point of view, this is achieved by introducing a point source,

$$\psi^{(x_0,b_0,\beta_0)}(x)_b^\beta = \delta(x-x_0)\delta_{b\,b_0}\delta_{\beta,\beta_0} \tag{3.43}$$

and solving the equation $Dx = \psi$, the solution x being only one column of the full inverted Dirac operator,

$$D^{-1}{}_{\substack{\alpha\,\beta_0\\ a\,b_0}}(y|x_0) = \sum_{x,b,\beta} D^{-1}{}_{\substack{\alpha\,\beta\\ a\,b}}(y|x)\delta(x-x_0)\delta_{b\,b_0}\delta_{\beta,\beta_0}. \tag{3.44}$$

This quantity, which must be calculated for the $4\,N$ possible values of β_0 and b_0, is calculated in practice by means of iterative numerical methods, like the Conjugate Gradient (CG) or a more advanced version of it (BiCGStab), explained in appendix C.

3.9. Mass extraction

In order to study the mass of the mesons, we first perform a Fourier transformation on the bilinear to set the hadron operator into a state of a definite spatial momentum $\vec{p}$:

$$\tilde{B}(\vec{p},t) = \frac{1}{V_s}\sum_{\vec{x}\in V_s} B(\vec{x},t)\exp(-i\vec{x}\cdot\vec{p}) \quad ; \quad V_s = a^3N_s^3 \tag{3.45}$$

and then we impose the condition $\vec{p}=\vec{0}$.

The source term $\overline{B}(\vec{0},0)$ in eq. (3.40) is left in real space; it does not require momentum projection, as states with different momenta are orthogonal.

By using zero-momentum operators, the meson correlator of eq. (3.40) can be replaced by

$$C(t) = \frac{1}{V_s}\sum_{\vec{x}\in V_s}\langle B(\vec{x},t)\overline{B}(\vec{0},0)\rangle, \tag{3.46}$$

which depends only on the time t, due to the averaging over the spatial position. To better understand the behaviour of this function, we insert in the correlator[5] a complete

[5] We drop the tilde and p from the notation.

sum over the eigenstates $|n\rangle$ of the Hamiltonian,

$$\mathbb{1} = \sum_n |n\rangle\langle n|. \tag{3.47}$$

While in principle $|n\rangle$ can represent any state (particle) of the theory, an operator B will overlap with states of the same quantum numbers, so that in practice the sum above can be interpreted as a sum over all the radial and internal excitations of a given particle. After the insertion, since $E_n = m_n$, it is clear that the correlator is a sum of exponentially suppressed terms,

$$\begin{aligned} C(t) &= \langle 0|B(t)B(0)|0\rangle = \sum_n \langle 0|B(t)|n\rangle\langle n|B(0)|0\rangle = \\ &= \sum_n \langle 0|e^{Ht}B(0)e^{-Ht}|n\rangle\langle n|B(0)|0\rangle = \sum_n e^{-t\,E_n}\,\|\langle 0|B(0)|m\rangle\|^2 = \\ &= \sum_n a_n e^{-t\,E_n} = a_0 e^{-t\,m_0} + a_1 e^{-t\,m_1} + \ldots, \end{aligned} \tag{3.48}$$

where for large values of t only the ground state (i.e. the particle of smallest mass) survives. This allows us to extract the mass value with an exponential fit over $C(t)$, which will behave like a $\cosh$ due to the periodic boundary conditions in time:

$$C(t) = A\left(e^{-t\,m_0} + e^{-(N_t - t)\,m_0}\right) \tag{3.49}$$

To summarize, the steps to extract the mass of a ground state meson are,

- generate a number n_c of configuraton.
- for each $i \in n_c$ create $4\,N$ point sources.
- invert the Dirac operator over the sources to get D^{-1}.
- contract numerically $\mathrm{Tr}\,\left(\Gamma D^{-1}\Gamma D^{-1}\right)$ as in eq. (3.41).
- for each time-slice average over the spatial volume to get the correlators.
- average over the configurations.
- fit the data.

While this method is in principle sufficient to obtain the mass of a ground state meson, in the practice the presence of excited states can contribute significantly to the signal, in a way that requires large lattice extension in the temporal direction. Moreover, except for the lightest (pseudosclar) meson, the signal to noise ratio deteriorates

exponentially with the Euclidean time separation. To overcome this problem we use the techniques explained in the next two sections.

As a last remark, we stress how this entire procedure depends on two parameters: β, which ultimately is related to the physical lattice spacing, and κ, which tunes the mass of the quarks and ultimately the mass of the hadrons, which are made of quarks. One needs to repeat the whole analysis for many κ, β, N and V-values, in order to approach and fit the limit of infinite volume, large N, zero (or small) mass and zero lattice spacing. Computing accurate correlators tends to be more and more expensive in the chiral ($m_q = 0$) and the continuum limits. However, the noise to signal ratio becomes better in the large N limit and for bigger volumes.

3.10. Extended sources

From eq. (3.48) it is clear that in order to have a good signal for the correlation functions one needs to employ operators B which have a strong overlap with the desired hadron state. Since composite particles are usually not point-like, i.e. they have some smeared distribution over space, one can assume that replacing point-like sources with Gaussian-shaped ones improves the signal. Moreover, one can vary the width of the Gaussian to tune the operators.

In order to mimic a Gaussian shape, we employ several steps of Wuppertal smearing [32] which, starting from a point source ψ^0, iteratively modifies a fermion field as:

$$\psi^{n+1} = \frac{1}{1+6\,\omega}\left(\psi^n + \omega \sum_{j=\pm 1}^{\pm 3} U'_j(x)\psi^n(x+a\hat{j})\right), \tag{3.50}$$

where n denotes the number of iterations, ω is the smearing parameter (we used $\omega = 0.25$). The practice has shown that smoother signals can be obtained by using a smeared U' gauge field with respect to the standard one U. In this case we employ 10 iterations of the so called APE smearing routine [33]:

$$\begin{aligned} U'_i(x) = \mathrm{Proj}_{\mathrm{SU}(N)}\Big[\alpha\, U_i(x) + \sum_{i\neq j} U_j(x)U_i(x+a\hat{j})U_j^\dagger(x+a\hat{i}) \\ + U_j^\dagger(x-a\hat{i})U_i(x-a\hat{j})U_j(x+a\hat{i}-a\hat{j})\Big], \end{aligned} \tag{3.51}$$

with smearing parameter $\alpha = 2.5$.

Smearing can be applied both at the source and the sink, the latter requiring to apply the same iterative routine in eq. (3.50) to the inverted propagator. The Wuppertal smearing is designed so that the Gaussian shape becomes wider the more iteration one performs. Unfortunately, there is no a-priori knowledge of how many steps to take

for the best signal in terms of its ground state overlap, the choice depending on the operator, the lattice spacing, etc.

To quantify the quality of the smearing method, we introduce an "effective" mass m_{eff},

$$a\, m_{\text{eff}}(t) = \operatorname{arccosh}\left[\frac{C(t+a)+C(t-a)}{2C(t)}\right]. \tag{3.52}$$

For negligible excited state contributions one would expect eq. (3.49) to hold exactly, i.e. m_{eff} should be a constant. A deviation from a constant will reveal the presence of excited state contamination. In fig. 3.2 we plot the effective mass for a pion, where the operators have been smeared both at source and sink, for an increasing number of steps.

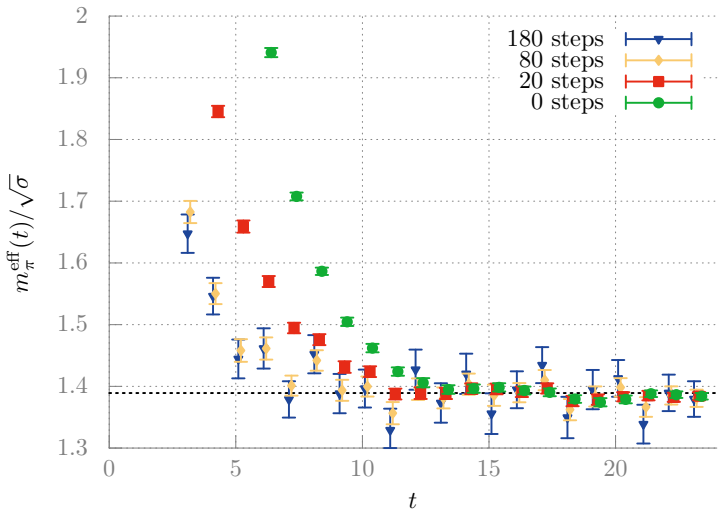

Figure 3.2.: Effective mass for an SU(7) pion with $m_\pi \approx 620$ MeV. Different choices of smearing steps are shown.

While all the curves tend to the same plateau, the most smeared ones reach it earlier (i.e. for smaller values of t), though at the price of larger statistical errors. For this reason, both non-smearing and over-smearing are not advisable. To get rid of the higher states contribution, we look at the effective mass to establish the safe fitting region (see the next section) but we fit the correlator to eq. (3.49), instead of fitting the effective mass.

3.11. Variational method

The methods described so far allow to extract only the ground state from a given correlator, with a precision that depends on the overlap between the operator and the physical state. In order to extract the ground state and the first excited level we employ the variational analysis discussed in refs. [34–36]. For each channel, we computed the cross-correlation matrix,

$$C_{ij}(t) = \langle O_i(t)\overline{O}_j(0)\rangle \tag{3.53}$$

where i and j correspond to the number of iterations (0, 20, 80 or 180 steps in our case) of Wuppertal smearing, for the sources and the sinks.

Then we solved the generalized eigenvalue problem:

$$C(t)\mathbf{v}^\alpha = \lambda^\alpha(t)C(t_0)\mathbf{v}^\alpha \tag{3.54}$$

to extract the eigenvalues λ^α which, as shown in ref. [35], behave as,

$$\lambda^\alpha(t) = \lambda_0^\alpha e^{-tE_\alpha}\left(1 + \mathcal{O}(e^{-t\Delta E_\alpha})\right) \tag{3.55}$$

for $t \ll N_t a$ with $E_\alpha = m_\alpha$ for $\vec{p} = 0$ and ΔE_α being the mass gap to the next state (higher α-values indicating higher states). For the largest and second largest eigenvalues, λ^0 and λ^1, we apply the same techniques explained in the previous section for $C(t)$, i.e. we extract the mass m performing hyperbolic-cosine fits in $[t_{\min}, t_{\max}]$ ranges ($t_{\max} \leq aN_t/2$) according to,

$$\lambda(t) = A\left(e^{-mt} + e^{-m(aN_t - t)}\right). \tag{3.56}$$

All statistical uncertainties were estimated using a jackknife procedure. With four different operators O_i, in many cases we were able to extract the first three states, however we regard the second excited states as unreliable at the present statistics. Using a subset of three operators out of the four mentioned above leads to compatible mass values within errors.

Varying t_0 in the range $[0, 2a]$ gives compatible results, so we used $t_0 = a$. To select the best fit ranges, for each particle we first studied the effective mass defined in eq. (3.52), replacing $C(t)$ with $\lambda(t)$. We determined $t_{\min}$ as the Euclidean time separation at which m_{eff} reaches a plateau (within statistical uncertainties), so that the contribution from higher states is negligible, while $t_{\max} \leq aN_t/2$ is the value where m_{eff} becomes too noisy for stable fits. The signals become more precise at larger N, lower κ-values (i.e. larger quark masses) and are most precise for the pion and rho channels. Typically we fit $\lambda(t)$ in the range $[5a, aN_t/2]$ for the ground states and in the range $[5a, 10a]$ for the first excited states, adjusting these ranges (by one or two lattice spacings) on a case-by-case basis. Fitting to eq. (3.56) with this procedure leads to reduced χ^2-values which are well below one.

The cost of inverting the propagator increases at lower quark masses, with the signal becoming noisier at the same time. For this reason, for the lowest two quark masses of each $\mathrm{SU}(N)$ group, we focused only on the ground states and instead of using the variational method we computed the two point functions using 80 steps of smearing for the sources/sinks[6]. We then applied the same analysis for $\lambda(t)$ directly to the correlator $C(t)$.

3.12. String tension σ

Phenomenologically, we can model mesons by assuming that the valence quark and antiquark in a meson are tied together by a linearly rising potential. The simplest way to describe such a behaviour is to assume that the infrared regime of QCD is described by an "effective" string which joins together quark and antiquark.

In the real world the best set up to extract experimental information on the string tension σ is represented by the spectrum of the heavy quarkonia where the quark-antiquark spectrum can be studied with non-relativistic techniques thanks to the large masses of the quarks. Suitable potential models can be used to fit the spectrum and in this way a phenomenological estimate for $\sigma \approx 1$ GeV/fm can be extracted.

On the lattice the simplest way to mimic a static quark-antiquark pair is by studying the expectation value of a large rectangular Wilson loop of sizes $R \times T$ as shown in fig. 3.3. The physical interpretation of the expectation value $\langle W(R,T)\rangle$ is that it represents the variation of the free energy due to the creation a the time t_0 of a quark and an anti-quark which are separated by a distance R from each other, evolve for a time T, and finally annihilate at the instant $t_0 + T$.

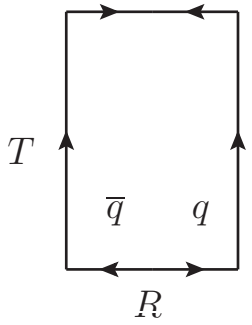

Figure 3.3.: The Wilson loop around a $R \times T$ rectangle.

According to this description we expect that for large T:

$$\langle W(R,T)\rangle \sim e^{-T\,V(R)} \tag{3.57}$$

where $V(R)$ is the potential energy of the quark-antiquark pair. A way to estimate its value is:

$$V(R) = -\lim_{T\to\infty} \frac{\partial}{\partial T} \log\langle W(R,T)\rangle \tag{3.58}$$

In numerical simulations of non-Abelian Yang-Mills theory at zero temperature, Wilson loops of asymptotically large sizes are always found to obey an "area law":

[6]Usually one has to smear more at smaller lattice spacing. In the section related to the continuum limit, we used 180 smearing steps and slightly larger $t_{\min}$ values for the very smallest lattice spacing.

$$\langle W(R,T)\rangle = e^{-\sigma RT+\ldots} \tag{3.59}$$

The area law for the Wilson loops is responsible for a linear rise of the potential: $V(R) \simeq \sigma R$, which implies linear confinement of static color sources, and the quantity σ takes the name "string tension".

The string tension σ is an important quantity in lattice QCD, as it can be used to "set the scale" in pure gauge lattice simulations, i.e. to connect the values read on the lattice (pure numbers) to real-world quantities. In fact any quantity on the lattice is expressed in units of the lattice spacing a, which needs to be converted in physical units (fm). On the lattice we can measure:

$$a\sqrt{\sigma} = F_\sigma(\beta) \tag{3.60}$$

where $F_\sigma(\beta)$ is a pure number depending on β. If we assume the *ad hoc* value $\sigma = 1$ GeV/fm $\approx (444\text{ MeV})^2$ and if we remember that into natural units $\hbar c \simeq 197\text{ MeV}\cdot\text{fm}$ is defined to be 1, we can extract the value of a:

$$a = \frac{F_\sigma(\beta)}{\sqrt{\sigma}} = \frac{F_\sigma(\beta)}{444\text{ MeV}} = \frac{F_\sigma(\beta)}{444} 197\text{ fm} \tag{3.61}$$

In the literature the numerical quantity $F_\sigma(\beta)$ is usually known with a very good precision, for most of the used gauge group in 3 and 4 dimensions. It is important to notice that the physical value $\sigma \approx (444\text{ MeV})^2$ is extrapolated from real-world phenomenology, so, strictly speaking, it should be used only for $\mathrm{SU}(3)$ QCD in 4d. It is a common practice however to use this number for different theories and dimensions. Alternatively, it is always possible to convert lattice results to physical units using ratios of dimensionful quantities, as we will do below.

4
Simulations and results

This chapter is focused on the results obtained at one single lattice spacing to illustrate the techniques and analysis used for each particle. Results at different lattice spacing, as well as continuum limit extrapolations, will be detailed in chapter 5.

4.1. Setting the scale

In this work, we study theories with $\mathrm{SU}(N)$ internal color symmetry with $N = 2$, 3, 4, 5, 6, 7 and 17 color charges; in each case we choose the coupling

$$\beta = \frac{2N}{g^2} = \frac{2N^2}{\lambda}, \tag{4.1}$$

such that the (square root of the) string tension in lattice units $a\sqrt{\sigma} \simeq 0.2093$ is the same for each N. This could be done with high accuracy for $N = 2$, 3, 4 and 6, using the string tension calculations of ref. [6,7], and for $N = 5$ and 7, using those of ref. [8]. Using the *ad hoc* value $\sigma = 1$ GeV/fm, our lattice spacing corresponds to $a \approx 0.093$ fm or $a^{-1} \approx 2.1$ GeV. We stress again that in the real world where experiments are performed, i.e. $n_f > 0$, $N = 3 \neq \infty$, the string tension is not well defined. This means that any absolute scale setting in physical units will be arbitrary and is just meant as a rough guide.

For the theory with $\mathrm{SU}(17)$ gauge group, there are unfortunately no string tension calculations available, so we extracted a β-value from a fit of the QCD Λ-parameter in

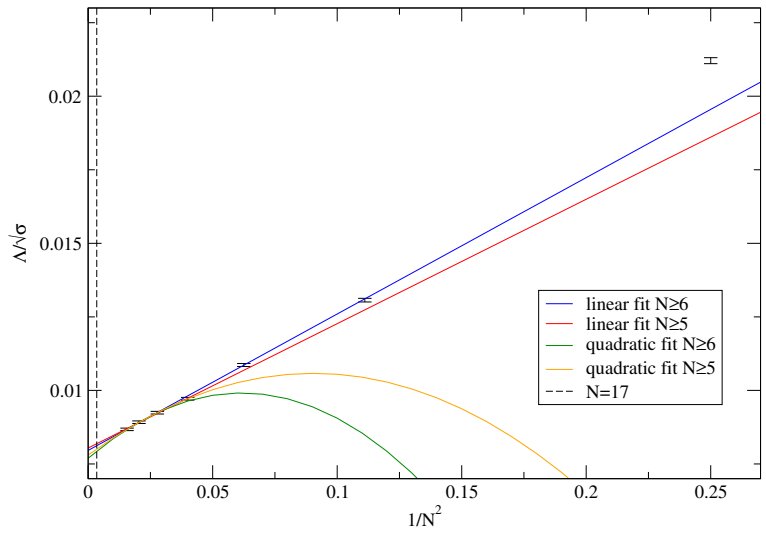

Figure 4.1.: Λ-parameter estimates of eq. (4.2), in units of the square root of the string tension. The errors shown are propagated from those of $a\sqrt{\sigma}$.

Fit	3 points	4 points
linear	208.45	208.16
quadratic	209.04	208.77

Table 4.1.: Fit results for β at $N = 17$.

the lattice scheme:

$$\Lambda \approx a^{-1} \exp\left[-\frac{1}{2b_0\lambda(a^{-1})}\right] \cdot \left[b_0\lambda(a^{-1})\right]^{-\frac{b_1}{2b_0^2}} \cdot \left[1 + \frac{1}{2b_0^3}\left(b_1^2 - b_2^L b_0\right)\lambda(a^{-1}) + \dots\right], \quad (4.2)$$

with [37,38]

$$\lambda = \frac{2N^2}{\beta}, \quad b_0 = \frac{11}{3\,(4\pi)^2}, \quad b_1 = \frac{34}{3\,(4\pi)^4}, \quad b_2^L = \frac{1}{(4\pi)^6}\left(-366.2 + \frac{1433.8}{N^2} - \frac{2143}{N^4}\right). \quad (4.3)$$

$\Lambda/\sqrt{\sigma}$ was calculated from the data presented in refs. [6–8] for $\mathrm{SU}(2 \leq N \leq 8)$ and is shown in figure 4.1. Using the data for $N = 6$, 7 and 8 and a linear fit in $1/N^2$, we obtained $\beta = 208.45$ for $N = 17$. Adding further values of $N \geq 4$ or using a quadratic fit in $1/N^2$ changed this value by less than 0.3% (see table 4.1).

Table 4.2 summarizes the essential technical information of our computations. The $N \leq 7$ results presented in the fits and plots here are obtained from the $24^3 \times 48$ lattices,

N	$N_s^3 \times N_t$	β	λ	$10^5\kappa$	n_{conf}
2	$16^3 \times 32$	2.4645	3.246	14581, 14827, 15008, 15096	400
	$24^3 \times 48$			14581, 14827, 15008, 15096, 15195.9 ,15249.6	200
	$32^3 \times 64$			14581, 14827, 15008, 15096, 15195.9 ,15249.6	100
3	$16^3 \times 32$	6.0175	2.991	15002, 15220, 15380, 15458	200
	$24^3 \times 48$			15002, 15220, 15380, 15458, 15563.8, 15613	200
	$32^3 \times 64$			15002, 15220, 15380, 15458, 15563.8, 15613	100
4	$16^3 \times 32$	11.028	2.902	15184, 15400, 15559, 15635	200
	$24^3 \times 48$			15184, 15400, 15559, 15635, 15717.3, 15764	200
5	$16^3 \times 32$	17.535	2.851	15205, 15426, 15592, 15658	200
	$24^3 \times 48$			15205, 15426, 15592, 15658, 15754.8, 15835.5	200
6	$16^3 \times 32$	25.452	2.829	15264, 15479, 15636, 15712	200
	$24^3 \times 48$			15264, 15479, 15636, 15712, 15805.1, 15884.5	200
7	$16^3 \times 32$	34.8343	2.813	15281.6, 15496.7, 15654.7, 15733.9	200
	$24^3 \times 48$			15281.6, 15496.7, 15654.7, 15733.9, 15827.3, 15906.2	200
17	$12^3 \times 24$	208.45	2.773	15298, 15521, 15684, 15755, 15853.1, 15931	80

Table 4.2.: Parameters of the main set of lattice simulations used in this work, β denotes the gauge action parameter, while κ is the hopping parameter appearing in the quark propagator. All configurations were separated by 200 combined heatbath and overrelaxation Monte Carlo sweeps and found to be effectively statistically independent. For orientation we also include the bare 't Hooft parameter.

corresponding to $L_s = aN_s \approx 2.2$ fm. In order to study finite size effects (FSE), we also performed additional simulations, both using smaller and (for $N = 2$ and 3) larger volumes—see the discussion in section 4.9. For $\mathrm{SU}(17)$ we employed a smaller $12^3 \times 24$ volume. The corresponding extent $L_s = 12a \approx 2.512/\sqrt{\sigma}$ is well above the inverse critical temperature [8] $T_c^{-1} \approx 1.681/\sqrt{\sigma} \lesssim L_c$.

The κ-values were selected to keep one set of six pion masses approximately constant across the different $\mathrm{SU}(N)$ theories. To achieve this, we combined the results reported in ref. [17] for the groups studied therein with initial estimates for the groups that had not been studied before. We vary the "pion" mass down to $m_\pi/\sqrt{\sigma} \approx 0.5$ for groups with $N \geq 5$, and to $m_\pi/\sqrt{\sigma} \approx 0.75$ for $N < 5$. We also simulated a smaller quark mass for $\mathrm{SU}(N < 5)$ but found significant numbers of "exceptional configurations" [39] (up to 15 % of the total); we leave these data out of this work. For $N = 5$, at the lowest quark mass, only two exceptional configurations were encountered and we removed them from the analysis.

4.2. The PCAC mass and the critical hopping parameter κ_c

As already stated, the expectation value of a local operator O is given by,

$$\langle O \rangle = \frac{1}{Z} \int \mathcal{D}[\psi, \bar{\psi}, U] O[\psi, \bar{\psi}, U] e^{-S[U]}. \tag{4.4}$$

For an infinitesimal symmetry transformation $\psi \to \psi + \delta\psi, \bar{\psi} \to \bar{\psi} + \delta\bar{\psi}$, and for a non-anomalous transformation of the integration measure, the linear change in eq. (4.4) is

$$0 = \langle \delta O \rangle - \langle \delta S \, O \rangle. \tag{4.5}$$

In the case of an infinitesimal chiral transformation $\delta\psi(x) = \epsilon(x)\gamma_5\psi(x)$; $\delta\bar{\psi}(x) = \epsilon(x)\bar{\psi}\gamma_5(x)$, where $\epsilon(x)$ vanishes outside some bounded region, the variation to the action reads,

$$\delta S = \int d^4x \epsilon(x) \left[-\partial_\mu A_\mu(x) + 2mP(x) \right], \tag{4.6}$$

where $A^\mu(x) = \bar{u}(x)\gamma_\mu\gamma_5 d(x)$, $P(x) = \bar{u}(x)\gamma_5 d(x)$. For an operator O which creates a pion state on the vacuum, this leads to the formulation of the partially conserved axial current (PCAC) relation,

$$\langle 0 | \partial_\mu A^\mu | \pi \rangle = 2m_{\mathrm{PCAC}} \langle 0 | P | \pi \rangle, \tag{4.7}$$

which we use to determine our non-perturbative κ_c value.

On the lattice we compute $m_{\mathrm{PCAC}} = \lim_{t\to\infty} m_{\mathrm{PCAC}}(t)$ as:

$$a\, m_{\mathrm{PCAC}}(t) = \frac{C_{\gamma_0\gamma_5,\gamma_5}(t+a) - C_{\gamma_0\gamma_5,\gamma_5}(t-a)}{4C_{\gamma_5,\gamma_5}(t)}, \tag{4.8}$$

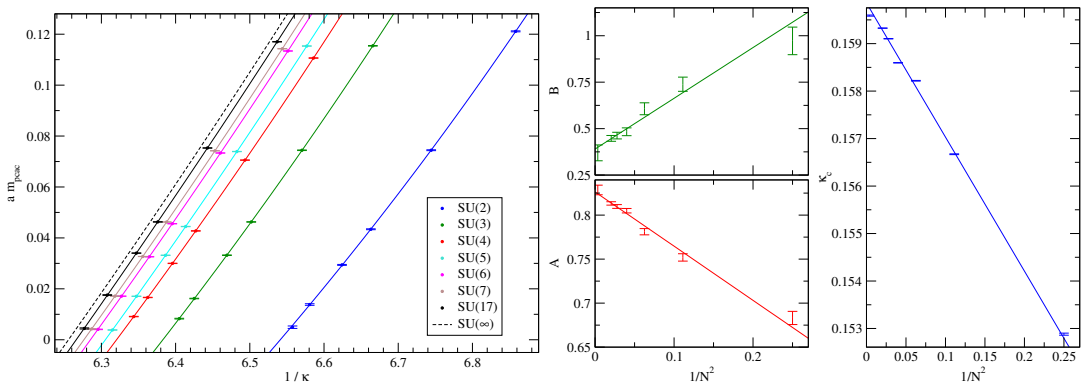

Figure 4.2.: Fit of the PCAC mass to eq. (4.10) (left), together with the $1/N^2$ fit of the parameters A, B and κ_c (right). We plot systematic errors for κ_c.

using smeared pion sources, and fit the plateau in t to a constant. This quantity is related to the vector quark mass am_q defined in eq. (3.34) by renormalization constants:

$$m_{\text{PCAC}} = \frac{Z_P}{Z_A Z_S} m_q. \tag{4.9}$$

Taking into account the leading lattice corrections $(1 + b_X a\, m)$ to renormalization constants Z_X and the currents themselves, we can fit our lattice results to the expression:

$$a\, m_{\text{PCAC}} = A\,(1 + B\, a\, m_{\text{PCAC}} + \dots)\,\frac{1}{2}\left(\frac{1}{\kappa} - \frac{1}{\kappa_c}\right), \tag{4.10}$$

from which we extract κ_c, A and B (see table F.1 of appendix F). The fits are plotted in figure 4.2.

The (unrenormalized) PCAC mass can be determined very precisely (see tables F.3-F.9), so we will expand every meson mass as a function of this variable.

We expect the parameters A, B and κ_c to have $\mathcal{O}(1/N^2)$ corrections, hence we fit them to

$$\alpha_1 + \frac{\alpha_2}{N^2}, \tag{4.11}$$

as shown in figure 4.2. With this analysis, we obtain good fits for A and B, with values of the reduced χ^2 close to 1, while for κ_c, although qualitatively the behavior looks very promising, we get a χ^2 per d.o.f. of 300, indicating that uncertainties in our data are underestimated. In fact κ_c can be considered a function of β only, which was chosen to match the string tension among the different groups. This process introduces a systematic error which propagates to κ_c. A qualitative way to estimate this propagation

is to consider finite differences between the values of κ_c, β and $a\sqrt{\sigma}$ from refs. [6–8, 18] and to compute

$$\delta\kappa_c = \frac{\Delta\kappa_c}{\Delta\beta}\frac{\Delta\beta}{\Delta(a\sqrt{\sigma})}\delta(a\sqrt{\sigma}). \tag{4.12}$$

The r.h.s factors of the equation above are listed in table F.2, together with $\delta\kappa_c$ for the groups available in refs. [17,18]. These systematic uncertainties due to the matching of β are ten to twenty times larger than the statistical ones and, since they are approximately constant across the N-values, we used the same errors for the remaining groups. Taking this into account, the reduced χ^2-value of the κ_c fit becomes 1.6.

The $1/N^2$ fit results are:

$$A = 0.8291(20) - \frac{0.699(45)}{N^2}, \tag{4.13}$$

$$B = 0.390(13) + \frac{2.73(26)}{N^2}, \tag{4.14}$$

$$\kappa_c = 0.1598555(33)(447) - \frac{0.028242(68)(394)}{N^2}, \tag{4.15}$$

where in the κ_c-case the second error is the systematic one, due to the slight mismatch in the string tension, detailed above. We find the values of $A \approx Z_P/(Z_A Z_S)$ to be consistent (up to 10% difference) to the non-perturbative renormalization constants calculated in appendix D. As discussed there, the systematics associated to Z_P are hard to assess and would require a dedicated work. For $\mathrm{SU}(3)$ we find a value of $A = 0.75$, which is consistent with the non-perturbative result 0.82(11) of [40] obtained at $\beta = 6.0$, close to our value $\beta = 6.0175$.

4.3. The pion mass

The pion masses are shown in figure 4.3 and presented in tables F.3–F.9 of appendix F as dimensionless ratios, dividing them by the square root of the string tension $\sqrt{\sigma}$. Quenched chiral perturbation theory [41], an effective low-energy theory that describes the dynamics of the lightest mesons, predicts

$$(am_\pi)^2 = A\,(am_q)^{\frac{1}{1+\delta}} + \ldots, \tag{4.16}$$

where the exponent δ is due to the presence of chiral logarithms. The theory predicts δ to be positive, $\mathcal{O}(10^{-1})$ for $\mathrm{SU}(3)$, and suppressed as $1/N$ at large N. However, it is known that data in the region where $m_\pi/\sqrt{\sigma} > 1$ are not very sensitive to chiral logarithms [42], and fitting larger pion masses according to eq. (4.16) would lead to values of δ with even the wrong sign. For this reason, we included a subleading term

of the quark mass expansion, performing fits according to:

$$\frac{m_\pi^2}{\sigma} = A\left(\frac{m_{\rm PCAC}}{\sqrt{\sigma}}\right)^{\frac{1}{1+\delta}} + B\frac{m_{\rm PCAC}^2}{\sigma}. \tag{4.17}$$

In these fits, the δ exponent is, essentially, determined by the lowest pion masses—which, unfortunately, are the points with the largest uncertainties. This leads to rather large relative errors for δ. Nevertheless, we find clear evidence that δ gets smaller when N is increasing. Within our precision, δ is found to be consistent with zero for all $N \geq 6$. In fact, for larger N one can omit δ completely from the formula and still obtain a good fit. Conversely, for $N \leq 3$ we find $\mathcal{O}(10^{-1})$ values of δ, where for $\mathrm{SU}(3)$ we get results consistent with those reported in ref. [43], in which Wilson and clover actions were used, and also consistent with table 3 of ref. [42], where different values of δ were calculated, using different actions. This suggests a small $1/N$ coefficient and thus we include the next higher order into the $1/N$ fit.

The N dependence of δ and the expansion of A and B in powers of $1/N^2$ (see figure 4.3) give a χ^2 per degree of freedom close to 2 and read:

$$A = 11.99(0.10) - \frac{8.7(1.6)}{N^2}, \tag{4.18}$$

$$B = 2.05(0.13) + \frac{5.0(2.2)}{N^2}, \tag{4.19}$$

$$\delta = \frac{0.056(19)}{N} + \frac{0.94(21)}{N^3}. \tag{4.20}$$

In order to assess the systematics on the exponent δ, we performed a combined fit $(m_{\rm PCAC}, N)$ of our data to eq. (4.17), using all the N-values at once and excluding the two highest masses for each group. Since the Wilson action explicitly breaks the chiral symmetry, we include in the fit also a constant term which however is found to be consistent with zero. The resulting curve has $\chi^2/\mathrm{d.o.f.} = 1.6$ and reads,

$$\begin{aligned}\frac{m_\pi^2}{\sigma} &= 0.0015(36) + \left(11.67(15) - \frac{8.1(5.4)}{N^2}\right)\left(\frac{m_{\rm PCAC}}{\sqrt{\sigma}}\right)^{\frac{1}{1+\delta}} + \\ &\quad + \left(2.95(42) - \frac{1(15)}{N^2}\right)\frac{m_{\rm PCAC}^2}{\sigma}\end{aligned} \tag{4.21}$$

$$\delta = \frac{0.093(27)}{N} + \frac{1.00(52)}{N^3}. \tag{4.22}$$

Note that the $m_{\rm PCAC}^2$ term is now less well determined, due to the exclusion of high mass points. However, the δ-parametrisation is consistent with the one of eq. (4.20).

In figure 4.4 we plot for each group the pion mass according to eq. (4.21) divided by the PCAC mass, in order to emphasise the deviations from a linear behaviour, due to the exponent δ.

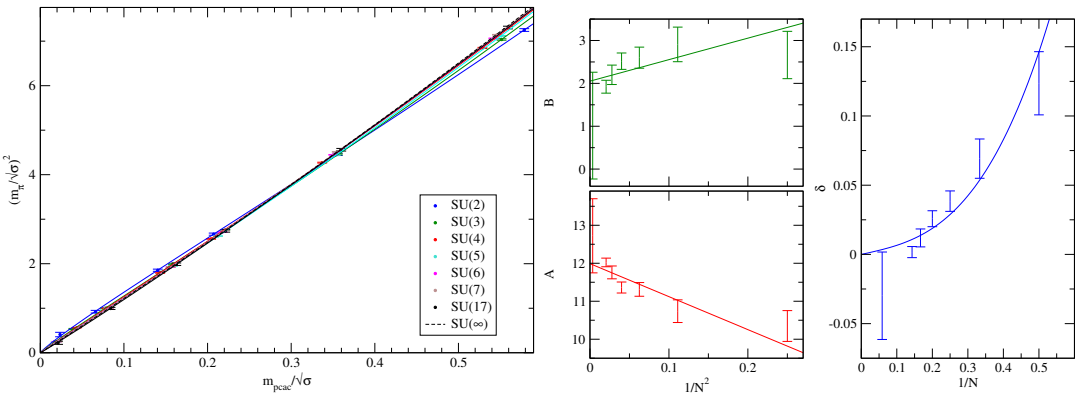

Figure 4.3.: Fit of the squared pion mass, in units of the string tension, to eq. (4.17) (left panel), N dependence of the fit parameters eq. (4.18)–(4.20) (right).

Below, we expand all the remaining meson masses as functions of m_{PCAC}. These can easily be translated into dependencies on m_π^2 through eq. (4.17) above.

4.4. The ρ mass

Quenched chiral perturbation theory predicts a dependence of m_ρ on the square root of the quark mass m_q [44], in contrast to the unquenched theory, where the leading behavior is linear in m_q. Thus the expansion of m_ρ takes the form:

$$m_\rho = m_{\rho,0} + C_{1/2} m_q^{1/2} + C_1 m_q + C_{3/2} m_q^{3/2} + \dots , \tag{4.23}$$

where the $C_{1/2}$ coefficient is expected to be negative and to vanish as $1/N$ in the large-N limit [44], restoring the linear behavior.

The masses of the ρ states are listed in tables F.3 to F.9 and plotted in figure 4.5 against the PCAC mass. For each group we fit:

$$\frac{m_\rho}{\sqrt{\sigma}} = A + B\left(\frac{m_{\text{PCAC}}}{\sqrt{\sigma}}\right)^{1/2} + C\frac{m_{\text{PCAC}}}{\sqrt{\sigma}} + D\left(\frac{m_{\text{PCAC}}}{\sqrt{\sigma}}\right)^{3/2} , \tag{4.24}$$

and then expand A, C and D in powers of $1/N^2$, while fitting B linearly in $1/N$. Note that D should vanish like $1/N^2$ in the large-N limit. The parameter B is found to be compatible with zero for $N > 5$ while the parameter D has unexpectedly a finite value: this effect is due to contamination from higher orders in the quark mass, as we show below.

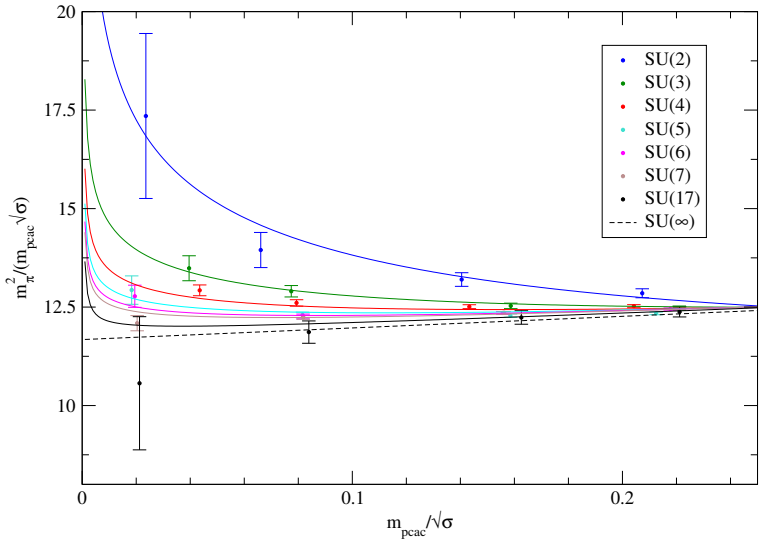

Figure 4.4.: Combined fit of $m_\pi^2/\left(m_{\mathrm{PCAC}}\sqrt{\sigma}\right)$. The solid curves are calculated using eq. (4.21), for each N.

The large-N expansion of the parameters reads:

$$\begin{aligned}\frac{m_\rho}{\sqrt{\sigma}} &= \left(1.504(51)+\frac{2.19(75)}{N^2}\right)-\frac{2.47(94)}{N}\left(\frac{m_{\mathrm{PCAC}}}{\sqrt{\sigma}}\right)^{1/2} \\ &+\left(3.08(53)+\frac{16.8(8.2)}{N^2}\right)\left(\frac{m_{\mathrm{PCAC}}}{\sqrt{\sigma}}\right) \\ &+\left(-0.84(31)-\frac{9.4(4.8)}{N^2}\right)\left(\frac{m_{\mathrm{PCAC}}}{\sqrt{\sigma}}\right)^{3/2}. \end{aligned} \tag{4.25}$$

To address the question of the non-vanishing large-N value of D, we interpolated the data with an alternative fit (figure 4.6) of the form:

$$\begin{aligned}\frac{m_\rho}{\sqrt{\sigma}} &= \left(1.5382(65)+\frac{0.51(11)}{N^2}\right)+\left(2.970(34)-\frac{3.39(55)}{N^2}\right)\left(\frac{m_{\mathrm{PCAC}}}{\sqrt{\sigma}}\right) \\ &+\left(-0.706(43)+\frac{3.00(68)}{N^2}\right)\left(\frac{m_{\mathrm{PCAC}}}{\sqrt{\sigma}}\right)^2. \end{aligned} \tag{4.26}$$

Although the $1/N$ counting of eq. (4.26) is not consistent, because of the missing square root term, one should notice that eq. (4.25) and eq. (4.26) share the same $N\to\infty$ behaviour. In fact the $N=\infty$ coefficients of eq. (4.25) agree within the errors with those of eq. (4.26). In particular, we stress that the non-vanishing term $0.84(31)\left(m_{\mathrm{PCAC}}/\sqrt{\sigma}\right)^{3/2}$ is

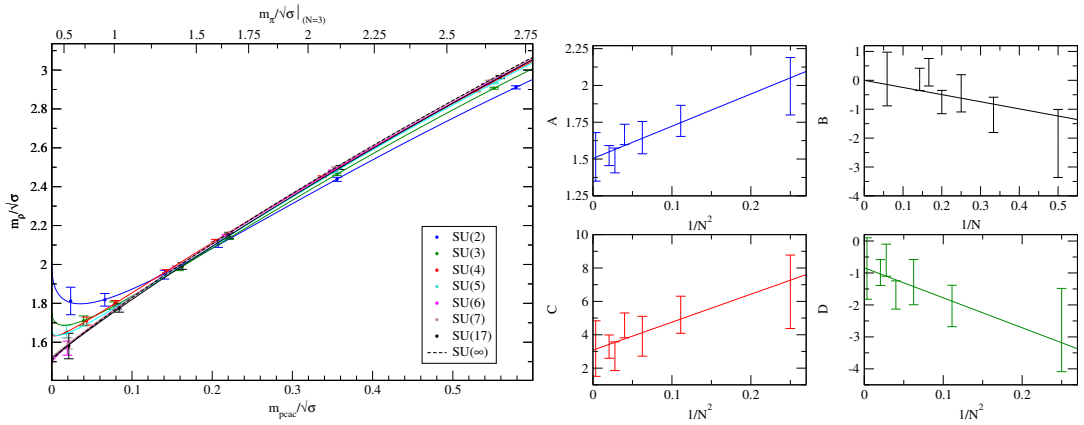

Figure 4.5.: Fit of the ρ mass to: $m_\rho/\sqrt{\sigma} = A + B \cdot (m_{\rm PCAC}/\sqrt{\sigma})^{1/2} + C \cdot m_{\rm PCAC}/\sqrt{\sigma} + D \cdot (m_{\rm PCAC}/\sqrt{\sigma})^{3/2}$ (left). $1/N^2$ fits of the parameters A, C and D and $1/N$ fit of B (right).

consistent with $0.706(43)\,(m_{\rm PCAC}/\sqrt{\sigma})^2$, for the range of $m_{\rm PCAC}$ studied. In principle one should introduce a quadratic term into eq. (4.25), in practice however, such a fit to six points with five free parameters becomes unstable and does not allow us to study the $1/N$ behaviour of the coefficients.

A possible solution is to fit the data for all groups at once using a combined fit, where we fix the $(m_{\rm PCAC}, N)$ functional form up to the second order term in the quark mass (figure 4.7). With this approach we obtain:

$$\begin{aligned}\frac{m_\rho}{\sqrt{\sigma}} &= \left(1.5395(83) + \frac{0.92(21)}{N^2}\right) - \frac{0.06(14)}{N}\left(\frac{m_{\rm PCAC}}{\sqrt{\sigma}}\right)^{1/2} \\ &+ \left(2.994(44) - \frac{13.9(48)}{N^2}\right)\left(\frac{m_{\rm PCAC}}{\sqrt{\sigma}}\right) + \left(\frac{27(11)}{N^2}\right)\left(\frac{m_{\rm PCAC}}{\sqrt{\sigma}}\right)^{3/2} \\ &+ \left(-0.739(50) - \frac{15.1(73)}{N^2}\right)\left(\frac{m_{\rm PCAC}}{\sqrt{\sigma}}\right)^2, \end{aligned} \tag{4.27}$$

with a $\chi^2/\text{d.o.f.} = 2$. The drawback of this approach is that data at small (m_q, N) have less weight in the combined fit, leading to a smaller coefficient for the $m_{\rm PCAC}^{1/2}$ term.

In order to compare our results with the holographic prediction (see section 6.2) it is useful to study m_ρ as a function of the pion mass, paying particular attention to the linear term of $m_\rho(m_\pi^2)$. Since the results of eqs. (4.25)–(4.27) tend to agree in the large-N limit and considering that our extrapolation relies on small N, which might be affected by quenched deviations, we quote eq. (4.25) as our best phenomenological

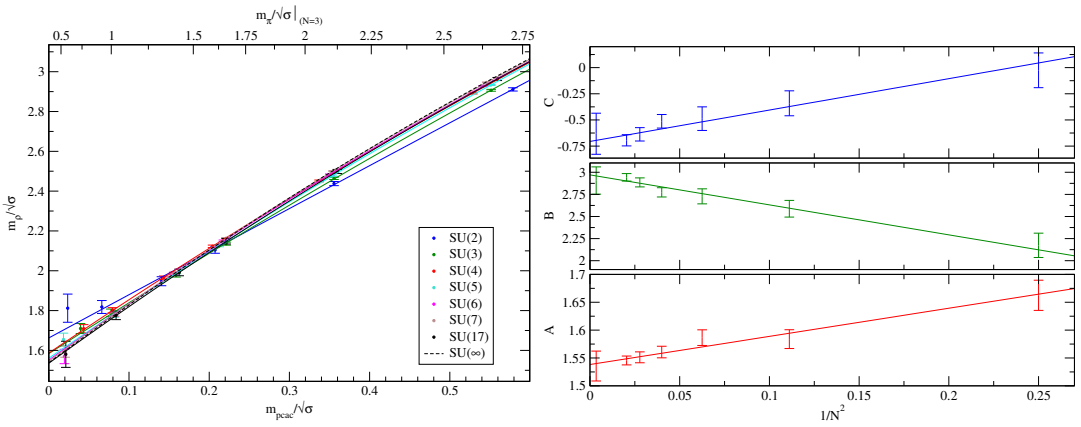

Figure 4.6.: Quadratic fit of the ρ mass in units of the square root of the string tension, according to eq. (4.26).

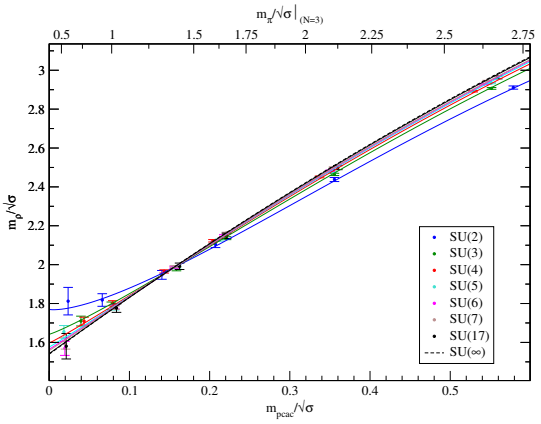

Figure 4.7.: Combined fit of the ρ mass in units of the square root of the string tension. The solid curves are calculated from eq. (4.27) for the different N.

parametrization of the data. To avoid further propagation of errors, we fit for each N the ρ data directly to the π masses using the fit form of eq. (4.25), with the substitution $m_{\text{PCAC}} \to m_\pi^2$. Then we extrapolate the fitted slope to $N \to \infty$, obtaining:

$$\frac{m_\rho(m_\pi)}{m_\rho(0)} = 1 + 0.360(64) \left(\frac{m_\pi}{m_\rho(0)}\right)^2 + \dots . \tag{4.28}$$

As a consistency check, we can omit the data corresponding to the largest quark masses and repeat the analysis using only the smallest three masses and a simple linear fit. This leads to:

$$\frac{m_\rho^{\text{lin}}(m_\pi)}{m_\rho(0)} = 1 + 0.317(2) \left(\frac{m_\pi}{m_\rho(0)}\right)^2 + \dots , \tag{4.29}$$

where the smaller error may be unreliable because the fit has two free parameters for only three data points. We quote eq. (4.28) as our final result. As already pointed out in ref. [17], the results for the slope are close to the holographic prediction obtained in the context of the model presented in ref. [45] (see ref. [46] for a detailed discussion).

4.5. The scalar particle

The analysis of the scalar mesons a_0 requires special attention. In the quenched theory, in which η' also becomes a Goldstone boson violating unitarity, the scalar correlator shows a long-range negative contribution, in addition to the standard short-range exponential decay. In ref. [47] it was shown that this effect, which is dominant and clearly visible only at the lowest quark masses, is caused by loop diagrams corresponding to an intermediate $\eta' - \pi$ state, which is light and has negative norm in the quenched approximation. Our approach consists in fitting the a_0 two-point functions as:

$$C(t) = C_0 e^{-m_{a_0} t} - C_1 e^{-\mu t}, \tag{4.30}$$

where the "unphysical" quantities C_1 and μ are fixed using the values at large t only. This approach works very well for $N \geq 5$, where the noise in the central region of the correlator is smaller. For similar smearing/normalization we expect the amplitudes C_i to be proportional to N, with $1/N^2$ corrections,

$$C_i \approx N \left(a_i + \frac{b_i}{N^2} + \dots\right). \tag{4.31}$$

In particular, we expect the ratio C_1/C_0 to be zero at $N = \infty$, i.e. $a_1 = 0$ and $C_1 \propto N^{-1}$. Indeed we find no evidence of negative contributions at $N = 17$ for the values of the quark masses studied. Moreover, the negative contributions get smaller at higher masses, meaning that C_1 is at least suppressed like m_{PCAC}^{-1} (and vanishes for $m_{a_0} > 2m_\pi$).

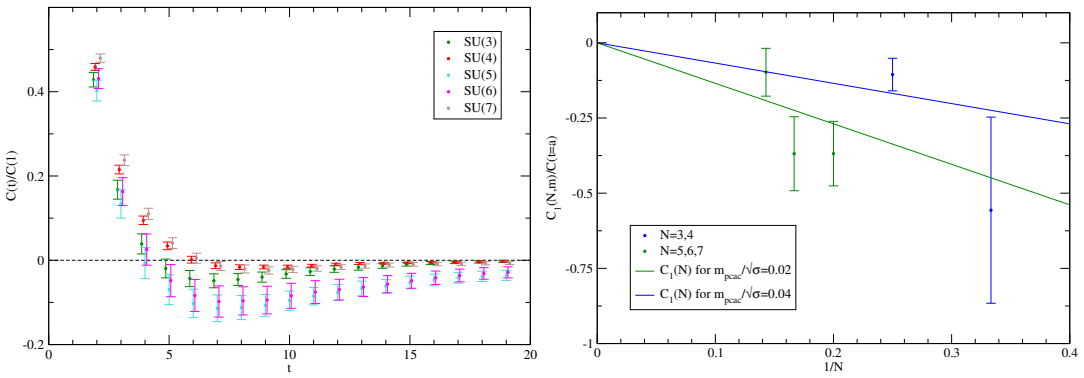

Figure 4.8.: Left: the a_0 two point functions for each $\mathrm{SU}(N)$ group at the lowest mass value. Notice that the smallest PCAC mass for $\mathrm{SU}(3,4)$ is approximately twice the one for $\mathrm{SU}(5,6,7)$ ($m_{\mathrm{PCAC}}/\sqrt{\sigma} \approx 0.04$ vs. 0.02, see tables F.3-F.9). Right: the amplitudes of the negative long range contribution, $C_1(N, m_{\mathrm{PCAC}})$, normalised to $C(t = 1)$ for each group at the lowest quark masses. The solid curves represent their expectation according to the fit of eq. (4.32) for $m_{\mathrm{PCAC}}/\sqrt{\sigma} = 0.02$ and for $m_{\mathrm{PCAC}}/\sqrt{\sigma} = 0.04$.

(Un)fortunately this behaviour is visible only at the very lowest quark mass for each of the groups studied, shown in figure 4.8 (left), so we cannot analyse in detail the amplitude C_1 as a function of m_{PCAC}. The best strategy to give a qualitative estimate of C_1 is to employ a combined (m_{PCAC}, N) fit, where we use data points from all group (figure 4.8 - right). This leads to the preliminary estimate

$$\frac{C_1}{C(t=a)} = -0.0269(53)\frac{\sqrt{\sigma}}{N \cdot m_{\mathrm{PCAC}}}, \tag{4.32}$$

with a reduced χ^2 of 1.4. Note that for $\mathrm{SU}(2)$ (not shown in the figure) we were unable to obtain meaningful results.

The a_0 masses, calculated according to eq. (4.30), are listed in tables F.3-F.9 and their $1/N^2$ expansion (plotted in figure 4.9) reads,

$$\frac{m_{a_0}}{\sqrt{\sigma}} = \left(2.402(34) + \frac{4.25(62)}{N^2}\right) + \left(2.721(53) - \frac{6.84(96)}{N^2}\right)\frac{m_{\mathrm{PCAC}}}{\sqrt{\sigma}}. \tag{4.33}$$

4.6. The remaining mesons

The ground state energies for the remaining states are listed in tables F.3–F.9. The corresponding fits are shown in figures F.1–F.2 of appendix F; in these cases, our fits do

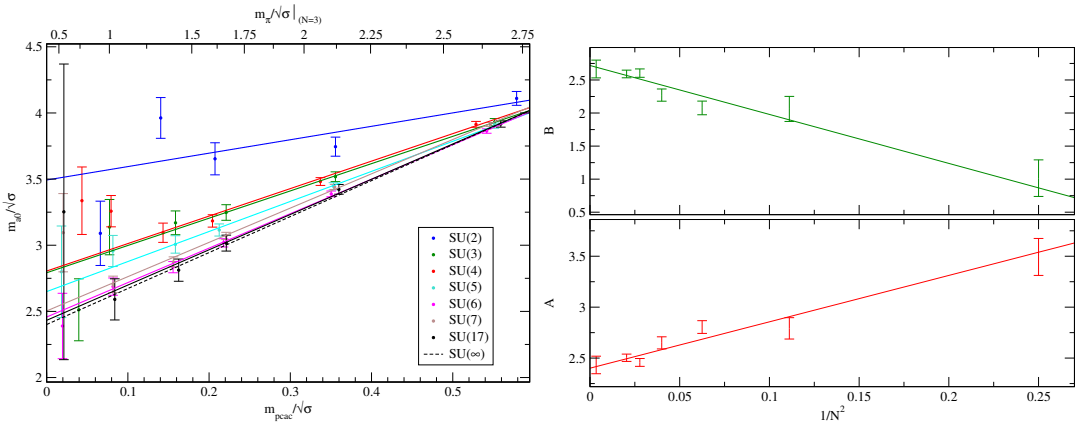

Figure 4.9.: Fit of the a_0 mass to: $m_{a_0}/\sqrt{\sigma} = A + B \cdot m_{\mathrm{PCAC}}/\sqrt{\sigma}$ (left) and $1/N^2$ fit of the parameters A and B (right).

not include quadratic terms, because of the larger uncertainties of the data. We fit the remaining states to the form,

$$\frac{m_X}{\sqrt{\sigma}} = \left(A_{X,1} + \frac{A_{X,2}}{N^2}\right) + \left(B_{X,1} + \frac{B_{X,2}}{N^2}\right) \frac{m_{\mathrm{PCAC}}}{\sqrt{\sigma}} \tag{4.34}$$

and list the results for $A_{X,1}, A_{X,2}, B_{X,1}$ and $B_{X,2}$ in table F.17.

As discussed above, the variational method allows us to extract the first excited states in each channel, although the results for these masses are much noisier than the corresponding ground states. We list the masses in tables F.10–F.16 and plot in figures F.3 to F.7 their quark mass dependences and the $1/N^2$ dependences of the respective fit parameters. The excited states are also fitted to eq. (4.34) and the results are listed in table F.17.

4.7. F_π and f_ρ

We define the lattice meson decay constants[1] F_π^{lat} and f_ρ^{lat} as

$$\langle 0|A_4|\pi\rangle = \sqrt{2}\, m_\pi F_\pi^{\mathrm{lat}}, \tag{4.35}$$

$$\langle 0|V_k|\rho_\lambda\rangle = m_\rho f_\rho^{\mathrm{lat}} e_k(p,\lambda), \tag{4.36}$$

where $A_4 = \bar{u}\gamma_4\gamma_5 d$ and $V_k = \bar{u}\gamma_k d$ are the non-singlet axial and vector currents, respectively, while $e_k(p,\lambda)$ denotes a polarization vector.

[1] Throughout the paper we use the notation $F_\pi = f_\pi/\sqrt{2} \approx 92$ MeV to indicate the pion decay constant. F_π^{lat} is the same quantity calculated on the lattice: $F_\pi = Z_A F_\pi^{\mathrm{lat}}$.

We fit the pion and the axial correlators for large t as:

$$\langle A_4(t)\pi_\alpha(0)\rangle \simeq \frac{1}{2m_\pi}\langle 0|A_4|\pi\rangle\langle\pi|\pi_\alpha^\dagger|0\rangle e^{-tm_\pi} \equiv C_{A_4}e^{-tm_\pi} \tag{4.37}$$

$$\langle \pi_\alpha(t)\pi_\alpha(0)\rangle \simeq \frac{1}{2m_\pi}\langle 0|\pi_\alpha|\pi\rangle\langle\pi|\pi_\alpha^\dagger|0\rangle e^{-tm_\pi} \equiv C_{\pi}e^{-tm_\pi} \tag{4.38}$$

(where π_α is one of the four differently smeared pion interpolators) and then compute F_π^{lat} as:

$$F_\pi^{\mathrm{lat}} = C_{A_4}\sqrt{\frac{1}{m_\pi C_\pi}}. \tag{4.39}$$

In order to better compare large-N to $N = 3$ results, we choose to normalize the decay constants as:

$$\hat{F}_\pi = F_\pi\sqrt{\frac{3}{N}}, \qquad \hat{f}_\rho = f_\rho\sqrt{\frac{3}{N}}. \tag{4.40}$$

For the $\mathrm{SU}(3)$ theory, we find results which are consistent with ref. [48], while for larger gauge groups our measurements show that the expected $\sqrt{N}$ scaling behavior is well satisfied, see figure 4.10 and tables F.18–F.24.

The $1/N^2$ expansion of the (rescaled) pion decay constant reads:

$$\begin{aligned}\frac{\hat{F}_\pi^{\mathrm{lat}}}{\sqrt{\sigma}} &= \left(0.2619(37) - \frac{0.121(56)}{N^2}\right) + \left(0.506(24) - \frac{0.29(30)}{N^2}\right)\frac{m_{\mathrm{PCAC}}}{\sqrt{\sigma}} \\ &\quad + \left(-0.320(31) + \frac{0.28(37)}{N^2}\right)\frac{m_{\mathrm{PCAC}}^2}{\sigma}.\end{aligned} \tag{4.41}$$

In the case of f_ρ^{lat}, we use a similar approach—the main difference being due to presence of the polarization vector $e_k(p,\lambda)$. This satisfies the relation

$$\sum_\lambda e_\mu(p,\lambda)e_\nu(p,\lambda) = g_{\mu\nu} - \frac{p_\mu p_\nu}{p^2}, \tag{4.42}$$

so that for zero momentum and for a fixed direction $\mu = \nu$ the above expression becomes one, and the computation is identical to the previous one (up to a $\sqrt{2}$ factor). To improve the statistical precision, we averaged the results over the three spatial directions. We plot the ρ decay constants for different N in figure 4.11; the $1/N^2$ fits can be summarized as:

$$\begin{aligned}\frac{\hat{f}_\rho^{\mathrm{lat}}}{\sqrt{\sigma}} &= \left(0.8560(56) - \frac{0.20(10)}{N^2}\right) + \left(0.395(38) - \frac{0.41(63)}{N^2}\right)\frac{m_{\mathrm{PCAC}}}{\sqrt{\sigma}} \\ &\quad + \left(-0.287(51) + \frac{0.31(79)}{N^2}\right)\frac{m_{\mathrm{PCAC}}^2}{\sigma}.\end{aligned} \tag{4.43}$$

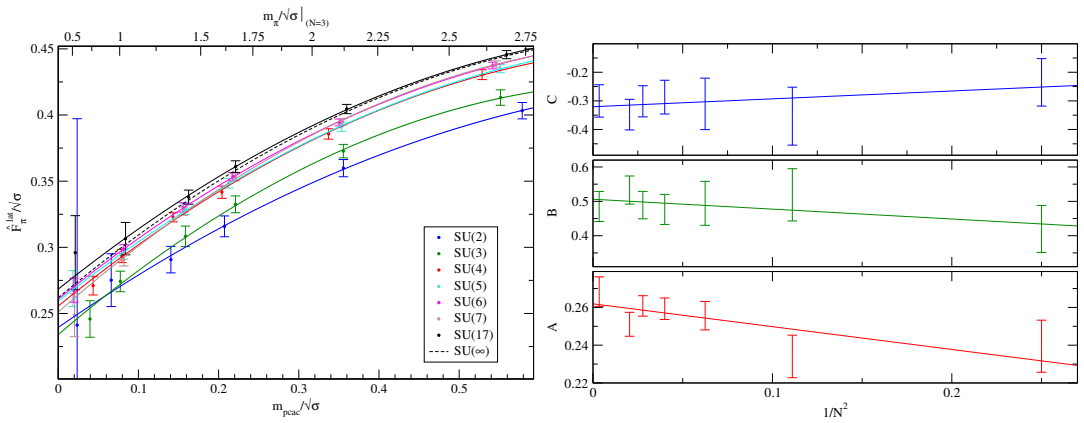

Figure 4.10.: Fit of the rescaled pion decay constant to: $\hat{F}_\pi^{\text{lat}}/\sqrt{\sigma} = A + B \cdot m_{\text{PCAC}}/\sqrt{\sigma} + C \cdot m_{\text{PCAC}}^2/\sigma$, and $1/N^2$ fit of the resulting fit parameters A, B and C.

The decay constants computed on the lattice are related to the ones in the continuum by the renormalization constants Z_A and Z_V,

$$\hat{F}_\pi = Z_A \hat{F}_\pi^{\text{lat}}, \qquad \hat{f}_\rho = Z_V \hat{f}_\rho^{\text{lat}}. \tag{4.44}$$

Prior to this work, Z_A and Z_V had been determined non-perturbatively only for $N = 3$ [40, 49] while two-loop perturbative results are known [50, 51] to converge slowly. In appendix D we discuss in detail the non-perturbative computation of Z_A and Z_V for $N = 3$ and $N \neq 3$ and of their systematics. The results for $\hat{F}_\pi$ and $\hat{f}_\rho$ are listed in tables F.18–F.24.

4.8. Chiral condensate $\langle\overline{\psi}\psi\rangle$

In the massless quark limit, the QCD Lagrangian with N_f flavours is invariant under the chiral transformations,

$$\psi' = e^{i\alpha\gamma_5 T_i}\psi \quad ; \quad \bar{\psi}' = \bar{\psi}e^{i\alpha\gamma_5 T_i} \tag{4.45}$$
$$\psi' = e^{i\alpha\gamma_5 \mathbb{1}}\psi \quad ; \quad \bar{\psi}' = \bar{\psi}e^{i\alpha\gamma_5 \mathbb{1}} \tag{4.46}$$

where T_i are the generators of $\mathrm{SU}(N_f)$. While the axial $U(1)_A$ symmetry is explicitly broken by the measure due to the axial anomaly,

$$\partial_\mu j_\mu^5 = -\frac{n_f}{32\pi^2}\epsilon_{\mu\nu\rho\sigma}F_{\mu\nu}^a F_{\rho\sigma}^a \tag{4.47}$$

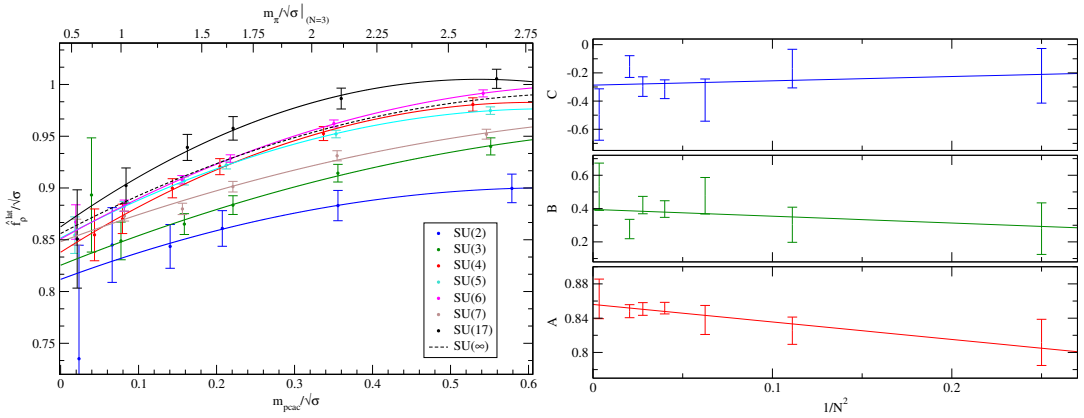

Figure 4.11.: Fit of the rescaled ρ decay constant to: $\hat{f}_\rho^{\text{lat}}/\sqrt{\sigma} = A + B \cdot m_{\text{PCAC}}/\sqrt{\sigma} + C \cdot m_{\text{PCAC}}^2/\sigma$ (left), together with the $1/N^2$ fit of the resulting parameters A, B and C (right).

the remaining of the chiral symmetry is spontaneously broken, giving rise to massless Goldstone bosons (the pions[2]). An order parameter for chiral symmetry breaking is represented by the chiral condensate $\langle\overline{\psi}\psi\rangle$ which is not invariant under chiral rotations. Consequently, a non-vanishing chiral condensate implies a spontaneously broken chiral symmetry.

Using the Gell-Mann Oakes Renner (GMOR) relation [52],

$$m_\pi^2 F_\pi^2 = (m_u + m_d)\langle\overline{\psi}\psi\rangle, \tag{4.48}$$

with the convention $\langle\overline{\psi}\psi\rangle \geq 0$, we can combine the data presented in the previous section to compute,

$$\langle\overline{\psi}\psi\rangle^{\text{lat}} = \frac{m_\pi^2 F_\pi^{\text{lat}\,2}}{2m_q}, \tag{4.49}$$

which is related to the quantity in the continuum by the renormalization constants Z_A and Z_S[3],

$$\langle\overline{\psi}\psi\rangle = Z_A^2 Z_S^{\overline{\text{MS}}}\langle\overline{\psi}\psi\rangle^{\text{lat}} \tag{4.50}$$

[2]In the real world, pions are massive due to the mass term $m\bar{\psi}\psi$ in the Lagrangian, which explicitly breaks chiral symmetry.

[3]The computation of Z_S is discussed in appendix D.

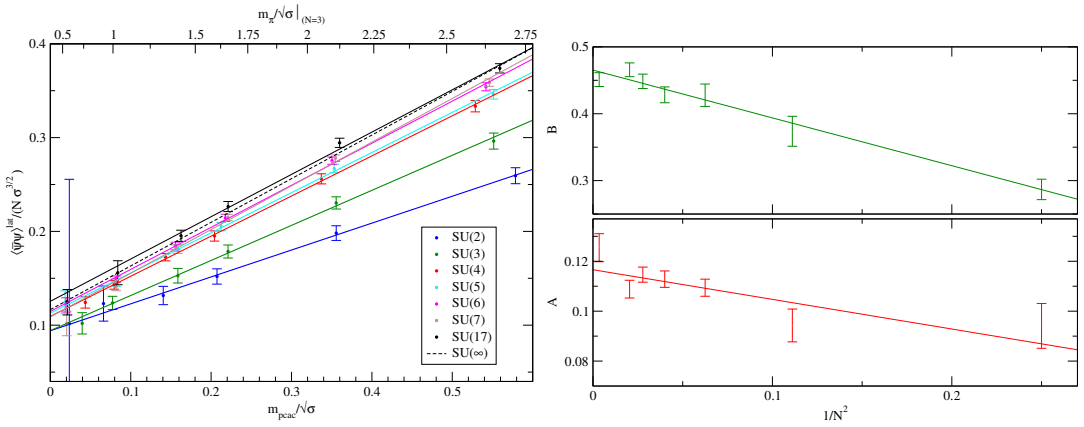

Figure 4.12.: Fit of the chiral condensate to: $\hat{f}_\rho^{\rm lat}/\sqrt{\sigma} = A + B \cdot m_{\rm PCAC}/\sqrt{\sigma} + C \cdot m_{\rm PCAC}^2/\sigma$ (left), together with the $1/N^2$ fit of the resulting parameters A and B (right).

In fig. 4.12, we show the $1/N$ fit of the derived quantity in eq. (4.49), which reads,

$$\frac{\langle\overline{\psi}\psi\rangle^{\rm lat}}{N\sigma^{3/2}} = \left(0.1166(22) - \frac{0.119(36)}{N^2}\right) + \left(0.4653(59) - \frac{0.715(69)}{N^2}\right)\frac{m_{\rm PCAC}}{\sqrt{\sigma}}. \tag{4.51}$$

4.9. Finite volume effects

Finite size effects (FSE) are expected [53] to be zero at infinite N, as long as all lattice dimensions (in physical units) are kept larger than a critical length L_c [54], so that center symmetry is not spontaneously broken.

At finite N, FSE become larger for smaller quark masses and for smaller N [55,56]:

$$m_\pi(L) = m_\pi(\infty)\,[1 + B\exp(-m_\pi(\infty)L))], \tag{4.52}$$

where the parameter B vanishes in the large-N limit. For $N = 2$ and 3, we carried out simulations at three volumes and fitted the pion masses to eq. (4.52), obtaining the results displayed in figure 4.13. As one can see from these plots, FSE are drastically reduced going from 2 to 3 colors, where the data can already be fitted to a constant. For larger N-values we carried out simulations at two volumes only, unsurprisingly, without any evidence of FSE. While one may also carry out a similar analysis for the

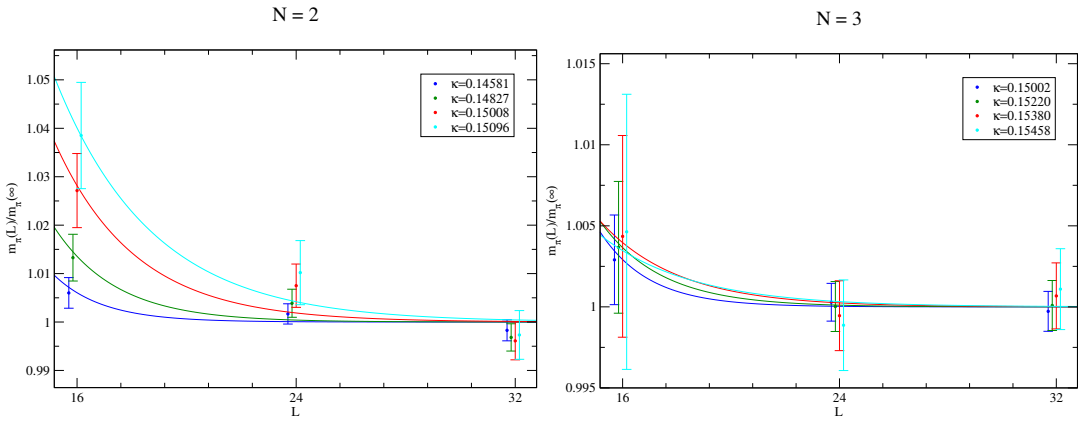

Figure 4.13.: Fit of $m_\pi(L)/m_\pi(\infty)$ according to eq. (4.52) for the $\mathrm{SU}(2)$ (left) and $\mathrm{SU}(3)$ theory (right).

other particles, their finite size corrections are expected to be smaller than for the pion, and thus negligible within our statistical uncertainties.

5
Large-N spectrum

5.1. Results for V=$24^3 \times 48$

We display in table 5.1 the results for the meson spectrum extrapolated to infinite N at different quark masses and for the fixed lattice spacing set by $a\sqrt{\sigma} = 0.2093$. For the decay constants and the chiral condensate we used the renormalization constants in the $\overline{\rm MS}$ scheme obtained as indicated in appendix D. The results are listed in units of $\sqrt{\sigma}$ and in units of the (normalized) pion decay constant in the chiral limit,

$$\hat{F}_\infty = \sqrt{\frac{3}{N}} F_\pi(m_q = 0)\Big|_{N\to\infty}, \tag{5.1}$$

which should be particularly useful for chiral perturbation theory (χPT) applications [57–61] (see section 6.3).

Of phenomenological interest is not only the spectrum at $m_q = 0$ (figure 5.1) but are also the spectra at $m_q = m_{ud}$ and at $m_q = m_s$ where m_{ud} and m_s denote the physical (isospin-averaged) light quark and strange quark masses, respectively. We fix the former imposing at $N = \infty$ the values [62]:

$$\hat{F}_\infty = 85.8 \text{ MeV}, \tag{5.2}$$

$$m_\pi(m_{ud}) = 135 \text{ MeV}. \tag{5.3}$$

The numerical estimate of $\hat{F}_\infty$ obtained in the $24^3 \times 48$ volume fixes the lattice spacing to $a = 0.10$ fm and the string tension to $\sigma = (395 \text{ MeV})^2$. These values however will be corrected in section 5.3, where continuum limit extrapolations are performed.

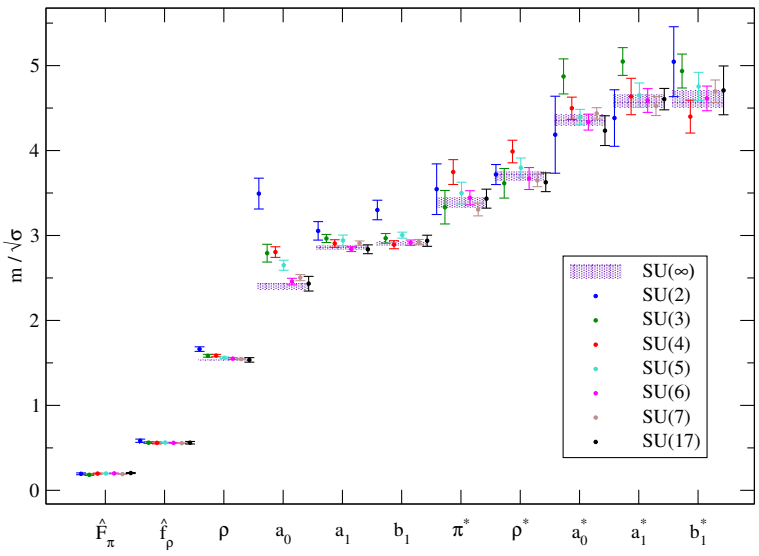

Figure 5.1.: The meson spectrum for different N in the chiral limit. The masses and the decay constants are given in units of the square root of the string tension for each group $\mathrm{SU}(N)$ and the extrapolated $N \to \infty$ values are shown as horizontal bands.

The strange quark mass is obtained by fixing at $N = \infty$ the mass of a (fictitious) strange-antistrange pion to the value

$$m_\pi(m_s) = (m_{K^\pm}^2 + m_{K^0}^2 - m_{\pi^\pm}^2)^{1/2} \approx 686.9\,\mathrm{MeV}. \tag{5.4}$$

Note that our way of fixing m_{ud} and m_s is arbitrary and different choices of input observables of real $N = 3$ QCD may give values that differ by $\mathcal{O}(1/N)$ corrections.

5.2. Continuum limit extrapolations for $\mathrm{SU}(4, 5, 7)$

In this section we discuss the impact of discretization effects on our lattice results, which so far have been obtained only at one value of the lattice spacing. A first step in this direction has been made in ref. [17] (a study carried out at values of a very close to ours), where the authors compared the ρ and π masses with those obtained at a different, coarser, lattice spacing from ref. [18]. In particular, they showed that, in spite of the 60% difference between the two lattice spacings used in the two studies, the ρ meson masses obtained are very close to each other (up to differences of the order of 5%). Since our simulations employ unimproved Wilson fermions, the leading lattice artefacts are

		$m_\infty/\sqrt{\sigma}$			$m_\infty/\hat{F}_\infty$		
Particle	J^{PC}	$m_q = 0$	$m_q = m_{ud}$	$m_q = m_s$	$m_q = 0$	$m_q = m_{ud}$	$m_q = m_s$
π	0^{-+}	0	0.35	1.74	0	1.61	8.00
ρ	1^{--}	1.5382(65)	1.5683(65)	2.216(11)	7.08(10)	7.21(10)	10.20(15)
a_0	0^{++}	2.401(31)	2.428(31)	3.059(33)	11.04(21)	11.17(21)	14.07(25)
a_1	1^{++}	2.860(21)	2.883(21)	3.414(23)	13.16(21)	13.26(21)	15.71(24)
b_1	1^{+-}	2.901(23)	2.924(23)	3.452(24)	13.35(21)	13.45(22)	15.88(25)
$\pi^\star$	0^{-+}	3.392(57)	3.413(57)	3.887(60)	15.61(34)	15.70(34)	17.88(37)
$\rho^\star$	1^{--}	3.696(54)	3.714(54)	4.127(56)	17.00(34)	17.08(34)	18.99(37)
$a_0^\star$	0^{++}	4.356(65)	4.375(65)	4.816(69)	20.04(41)	20.13(41)	22.16(44)
$a_1^\star$	1^{++}	4.587(75)	4.605(75)	5.012(81)	21.10(46)	21.18(46)	23.06(49)
$b_1^\star$	1^{+-}	4.609(99)	4.628(99)	5.06(11)	21.20(54)	21.29(55)	23.29(58)
$\hat{F}_\pi$	–	0.2174(30)	0.2216(30)	0.3035(58)	1	1.020(20)	1.396(33)
$\hat{f}_\rho$	–	0.5992(40)	0.6020(40)	0.6544(79)	2.757(43)	2.769(43)	3.010(56)
		$X_\infty/(N\sigma^{3/2})$			$X_\infty/(N\hat{F}_\infty^3)$		
$\langle\overline{\psi}\psi\rangle^{\overline{\rm MS}}$	–	0.0501(10)	–	–	6.39(42)	–	–

Table 5.1.: The $N = \infty$ meson spectrum and decay constants for $24^3 \times 48$ lattice volume, in units of the square root of the string tension $\sqrt{\sigma}$ and in units of the (normalized) pion decay constant $\hat{F}_\infty$ from eq. (5.1). Three different values of the quark mass are set using the pion masses as inputs. The results have not been extrapolated to the continuum limit.

expected to scale like a (the same holds for refs. [16–18] where the same action was used and ref. [29] where clover-Wilson fermions with tree-level coefficient were employed, resulting in $\mathcal{O}(\alpha a)$ lattice artefacts). Clearly, solid continuum limit results required the reiteration of the entire analysis for all the groups at different lattice spacings, keeping the physical volume $(aN_s)^3$ fixed, followed by fits in a. This unfortunately is too expensive for our computational resources, so our strategy is to split the analysis in two parts: in this section we estimate the discretisation effects for only a few groups, namely $SU(4)$, $SU(5)$ and $SU(7)$, and for four different lattice spacings. In the next section we will employ a, N fits to extrapolate to the combined limit $N \to \infty, a \to 0$.

Due to the limitation of this method, we stress that the results presented in this section should be interpreted as an estimate of the systematics associated to the lattice discretization, rather than a proper continuum limit prediction.

To make the simulations feasible we also dropped the variational method and we extracted the ground state masses using only one choice for the number of steps in the Wuppertal smearing: 80 steps for the coarser lattices and 180 steps for the finer ones.

When we set the scale for volumes of $24^3 \times 48$, we imposed the string tension to be $a\sqrt{\sigma} = 0.2093$ for all groups. In this section we use both coarser lattices, with $N_s = 16, 20$ and $aN_s\sqrt{\sigma}$ fixed, and one finer lattice spacing set by $a\sqrt{\sigma} = 0.15$. Due to computational costs, we employed for the latter a volume of $N_s = 32$ for $SU(4, 5)$ and $N_s = 24$ for $SU(7)$. From the analysis of the finite size effects (section 4.9), we can safely assume as negligible the effect of the volume mismatch in the $N = 7$ case.

To obtain the β-values corresponding to the selected lattice spacings we compute for each $\mathrm{SU}(N)$ group a set of points $\{a\sqrt{\sigma}, a\Lambda(\beta)\}$ using eq. (4.2) and the string tension values of refs. [6, 8]. Then we fit them (fig. 5.2) to the expression,

$$a\sqrt{\sigma} = a\Lambda \left(A + Ba\sqrt{\sigma} + \dots\right), \tag{5.5}$$

with A, B free parameters and we invert numerically the formulae. The β parameters, as well as the κ-values and volumes used for the continuum limit extrapolation are summarised in table 5.2.

In the tables F.25–F.30 we list the results obtained for the three additional lattice spacings in each of the $\mathrm{SU}(4, 5, 7)$ gauge theories. Each particle is fit to their proper quark mass dependence (figs. F.8–F.10), according to the methods detailed in the previous chapter, in order to obtain their chiral limit values.

The chiral limit spectrum for each of the three groups is plotted in fig. 5.3, where we explicitly indicate the percentage of deviation of the $a \to 0$ values from those obtained at $a\sqrt{\sigma} = 0.2093$. Continuum limit corrections look approximately uniform across the various N and are of order 5 to 10%. The scalar and vector particles get the stronger corrections and it is interesting to notice that their masses almost approach each other in the $N = 7$ continuum limit. This behaviour has been recently conjectured by χPT models in [59, 61], where the authors claim an exact equivalence $m_\rho = m_{a0}$ in the large-N limit.

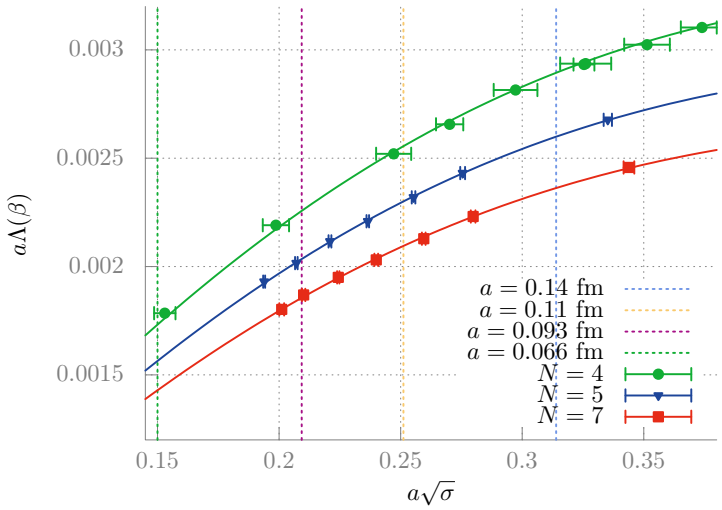

Figure 5.2.: Fit of the Λ-parameter as a function of $a\sqrt{\sigma}$. The vertical lines represent the values of $a\sqrt{\sigma}$ used in this work.

5.3. Continuum limit extrapolation for $\mathrm{SU}(\infty)$

The continuum and large-N limit spectrum for the ground state mesons and decay constants in the chiral limit is estimated by employing for each channel a combined fit to the form:

$$\left.\frac{m_X}{\sqrt{\sigma}}\right|_{m_q=0} = A + B\,a\sqrt{\sigma} + C\,\frac{1}{N^2} + D\,\frac{a\sqrt{\sigma}}{N^2}. \tag{5.6}$$

where we use as inputs both the data presented in chapter 4 and the mass values of the last section, obtained at different lattice spacings. The results are listed in table 5.3. While the fit to eq. (5.6) works well, with $\chi^2/d.o.f.$ of at most 1.4, the $m_q = 0$ results extracted in this way (i.e. column A of table 5.3) tend to have larger errors with respect to those of table 5.1, due to the larger number of parameters.

As done before, we present in table 5.4 the meson spectrum at the three different quark mass values $m_q = 0, m_{ud}, m_s$. For the chiral limit extrapolations, we used also a few $N = 3$ input values (especially for the ρ) from past studies available in literature [48, 63, 64], where the same action was employed. The numbers at the two massive scales instead are obtained by fixing at each N the constraints of eq. (5.2) and (5.4), followed by the fit to eq. (5.6). These results agree within errors with those of table 5.1, with the sole exceptions of the a_0 and ρ mesons, which tend to overlap. While for most channels the overall systematic effects are narrowed down to less than 5%, for the

N	$N_s^3 \times N_t$	β	λ	$10^5\kappa$	n_{conf}
4	$16^3 \times 32$	10.6573	3.00	15318.9, 15708.4, 16022.8, 16160.3, 16307.3, 16408.2	200
	$20^3 \times 40$	10.8485	2.95	15183, 15548, 15745, 15844, 15955, 16032	200
	$32^3 \times 64$	11.4462	2.80	14997, 15135, 15210, 15254, 15307, 15344	200
5	$16^3 \times 32$	16.96	2.95	15400, 15740, 16020, 16173, 16334, 16480	200
	$20^3 \times 40$	17.244	2.90	15330, 15572, 15785, 15864, 16000, 16110	200
	$32^3 \times 64$	18.155	2.75	15061, 15188, 15289, 15330, 15400, 15420	100
7	$16^3 \times 32$	33.7312	2.91	15281.6 , 15496.7 , 15654.7 , 15733.9 15827.3, 15906.2, 16120, 16290, 16460, 16570	200
	$20^3 \times 40$	34.2937	2.86	15281.6, 15496.7, 15654.7, 15733.9, 15827.3, 15906.2, 16020, 16105, 16175	200
	$24^3 \times 48$	36.08775	2.72	15050, 15220, 15310, 15380, 15430, 15465	200

Table 5.2.: Parameters of the continuum limit simulations used in this work.

Particle	A	B	C	D
ρ	1.687(24)	-0.673(98)	1.64(31)	-6.5(13)
a_0	1.81(17)	2.71(79)	13.6(41)	-34(19)
a_1	2.93(11)	-0.32(53)	-3.6(27)	22(13)
b_1	2.97(13)	0.11(60)	-0.4(31)	8(15)
$\hat{F}_\pi$	0.197(20)	0.014(91)	-0.28(46)	0.8(22)
$\hat{f}_\rho$	0.603(18)	-0.177(75)	-0.61(45)	1.7(20)
$\langle\overline{\psi}\psi\rangle^{\overline{\mathrm{MS}}}$	0.0504(77)	0.004(36)	-0.02(18)	0.00(86)

Table 5.3.: Combined large-N and continuum limit fit to eq. (5.6) for the $m_q = 0$ spectrum.

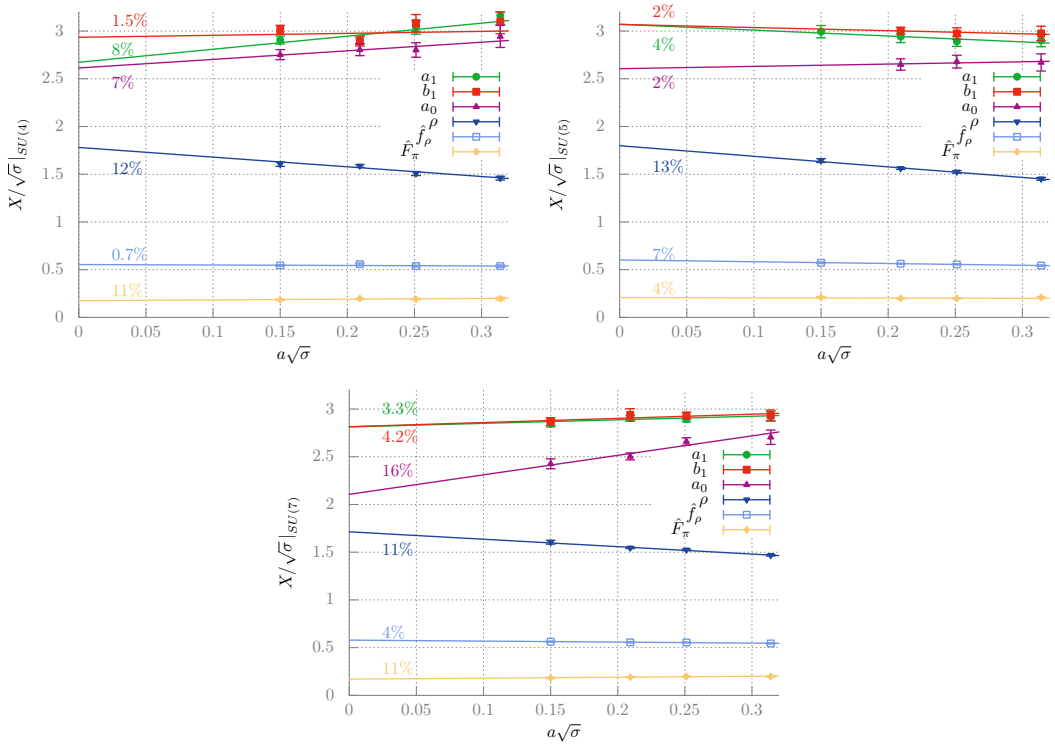

Figure 5.3.: Continuum limit $m_q = 0$ extrapolation of the SU(4) (top left), SU(5) (top right) and SU(7) (bottom) spectrum. The percentages along the lines indicate the discrepancies of such limits with the values at $a = 0.093$ fm (second point from the left) presented in table 5.1.

troublesome a_0 the uncertainties remain high ($\approx 10\%$) due to the "unphysical" negative ghost contributions described in section 4.5. Further simulations with higher statistics will be required in order to check to what extent the aforementioned mass-degeneracy conjectured in [59, 61] is valid.

The estimate $\hat{F}_\infty = 85.8\,\mathrm{MeV}$, together with our lattice value of 0.197(20), sets the $N \to \infty$ continuum limit string tension to be $\sigma = (436\ \mathrm{MeV})^2$, which in turn fixes the lattice spacing $a = 0.09$ fm for the previous simulations in the $24^3 \times 48$ volume. This way of introducing a physical scale, which, as emphasised, is arbitrary, allows us to compare the large-N spectrum to the physical masses from the experiments. As one can see in fig. 5.4, the deviation of QCD from its large-N limit is milder for the lowest lying meson spectrum and decay constants, while it can be larger (up to 20%) for excitations. However, concerning the latter remark, one has to consider that our lattice

		$m_\infty/\sqrt{\sigma}$			$m_\infty/\hat{F}_\infty$		
Particle	J^{PC}	$m_q=0$	$m_q=m_{ud}$	$m_q=m_s$	$m_q=0$	$m_q=m_{ud}$	$m_q=m_s$
ρ	1^{--}	1.687(24)	1.727(33)	2.25(10)	8.46(86)	8.77(82)	11.47(56)
a_0	0^{++}	1.81(17)	1.95(17)	2.65(16)	9.8(17)	9.9(17)	13.5(14)
a_1	1^{++}	2.93(11)	2.97(12)	3.45(13)	14.6(17)	15.1(17)	17.5(14)
b_1	1^{+-}	2.97(13)	3.03(14)	3.55(14)	15.1(18)	15.4(17)	18.0(15)
$\hat{F}_\pi$	–	0.197(20)	0.200(20)	0.270(21)	1	1.018(17)	1.371(41)
$\hat{f}_\rho$	–	0.603(18)	0.636(17)	0.709(12)	3.09(32)	3.23(31)	3.60(30)
		$X_\infty/(N\sigma^{3/2})$			$X_\infty/(N\hat{F}_\infty^3)$		
$\langle\overline{\psi}\psi\rangle^{\overline{\rm MS}}$	–	0.0504(77)	–	–	6.6(22)	–	–

Table 5.4.: The $N=\infty, a\to 0$ ground state meson spectrum and decay constants in units of the square root of the string tension $\sqrt{\sigma}$ and in units of the (normalized) pion decay constant $\hat{F}_\infty$ from eq. (5.1).

computations have less control of systematic errors on excited states, in particular, a minimum of 5% (extra) error should be taken into account due to the (missing) continuum limit extrapolation.

We find the large-N values of $m_\rho = 753(14)\ \mathrm{MeV}$ at $m_q = m_{ud}$ and $981(44)\ \mathrm{MeV}$ at $m_q = m_s$ to be very close to the physical $m_\rho = 775\ \mathrm{MeV}$ and $m_\phi = 1019\ \mathrm{MeV}$ in QCD. Also the ratio,

$$\frac{\hat{F}_\pi(m_{ud})}{\hat{F}_\pi(0)} = 1.018(17)\,, \tag{5.7}$$

compares favorably to the value $F_\pi(m_{ud})/F_\pi(0) = 1.0744(67)$ for $N=3$ QCD with sea quarks [62]. The (normalized) chiral condensate in the $N\to\infty$ limit,

$$\frac{3}{N}\langle\overline{\psi}\psi\rangle^{\overline{\rm MS}}(2\ \mathrm{GeV}) = (232(11)\ \mathrm{MeV})^3 \tag{5.8}$$

is found to be slightly bigger than our $\mathrm{SU}(3)$ value $\langle\overline{\psi}\psi\rangle^{\overline{\rm MS}} = (238(6)\ \mathrm{MeV})^3$, which compares well to $(245(9)\ \mathrm{MeV})^3$ from the past quenched LQCD study in [65]. However a recent LQCD study with sea quarks [66] reports a much bigger value, $\langle\overline{\psi}\psi\rangle^{\overline{\rm MS}} = (283(2)\ \mathrm{MeV})^3$, so the discrepancies with $\mathrm{SU}(\infty)$ might be larger in this case.

Lastly, we remind that in section 4.4 we obtained the slope $A = 0.360(64)$ for the expression,

$$\frac{m_\rho(m_\pi)}{m_\rho(0)} = 1 + A\left(\frac{m_\pi}{m_\rho(0)}\right)^2 + \ldots. \tag{5.9}$$

An attempt to extrapolate a continuum limit of A can be done by computing its value for each a, N combination, followed by a fit to the form eq. (5.6). Unfortunately this

approach fails to give a meaningful value (we get $A = 0.44(30)$) due to the generally higher errors of such combined fits. Alternatively, one can apply the same strategy using eq. (4.26) to fit the rho masses. The drawback of this method, which gives $A = 0.414(12)$, is underestimating the errors by forcefully removing one fit parameter (the $\sqrt{m_q}$ dependency of the quenched rho). For these reasons, we still quote $A = 0.360(64)$ as our best estimate of the slope.

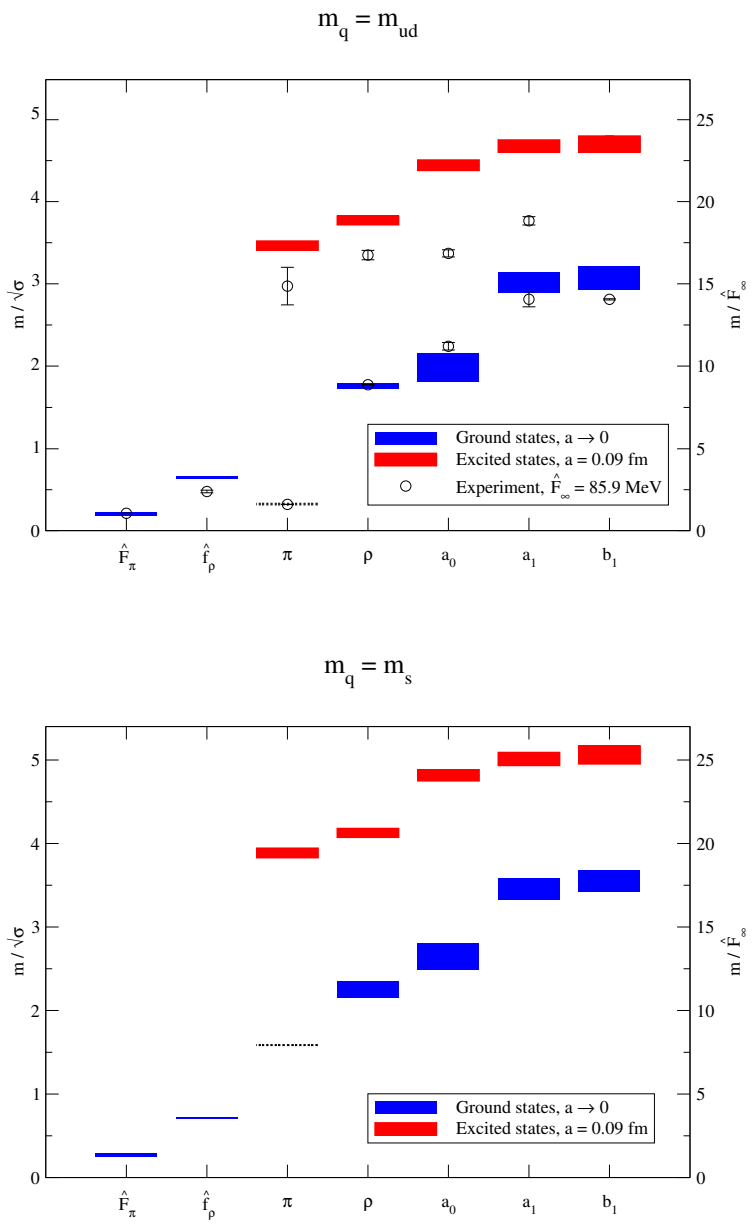

Figure 5.4.: Top: the continuum limit large-N meson spectrum at the $m_q = m_{ud}$ scale compared to the experimental $N = 3$ masses, using the values of the string tension $\sigma = (436\,\mathrm{MeV})^2$, obtained from imposing $\hat{F}_\infty = 85.9\,\mathrm{MeV}$. The pion mass is taken as input to set $m_q = m_{ud}$. Bottom: the large-N meson spectrum at the $m_q = m_s$ scale.

6
Comparison with other studies

6.1. Comparison with lattice studies

Thanks to the dramatic improvements on the computational side, the lattice community has nowadays moved their focus from quenched simulations to almost exclusively computations with sea quarks. Nonetheless, due to computational costs that scale like N^3, none of the large-N studies in the literature has employed dynamical fermions on the lattice as yet. Our $\mathrm{SU}(3)$ results agree with those of [48,49], obtained with the same action, very close lattice spacing and statistics while being compatible with the general $\mathrm{SU}(3)$ picture that emerges from other quenched analyses [63–65]. Before this work, only a few papers [16–20, 29] studied the N dependency of the meson spectrum, with results limited to π, ρ and F_π. Refs. [16–18, 29] used the same conventional techniques described in this work, i.e. extracting the meson masses from the long-distance behavior of the correlators at a relatively low N (up to 7). This method has been well tested and represents the standard way of implementing spectroscopy calculations. Our lattice simulations, which employ higher statistics and lower quark masses, seem to confirm and refine the general picture of refs. [16–18, 29], i.e. the large-N masses are close (within less than 20%) to those of the physical QCD world.

The authors of [19, 20] however extract masses at larger N ($N = 17$ and $N = 19$), using much smaller lattice sizes, from a single pole fit of momentum space correlators which are obtained injecting allowed discrete momenta in the lattice configurations. With this setup, they find in ref. [20] a ρ mass approximately twice as large as ours,

$$m_\rho/\sqrt{\sigma} = 3.50(22)\ , \tag{6.1}$$

while for the pion decay constant one infers from [19]

$$\hat{F}_\infty/\sqrt{\sigma} = 0.277(12)\ , \tag{6.2}$$

where the known value [8] $T_c/\sqrt{\sigma} = 0.5949(17)$ has been used to convert both original results (provided in units of the deconfinement critical temperature T_c) into units of $\sqrt{\sigma}$. The discrepancy between these and our values ($m_\rho/\sqrt{\sigma} = 1.687(24)$ and $\hat{F}_\infty/\sqrt{\sigma} = 0.197(20)$) is evident.

Although the technique used in [19, 20] is less well tested, one cannot exclude a priori the possibility that it gives better results at large N. Also note that the fermion discretizations differ: Wilson fermions were employed in [16–18, 29] and in the present work, overlap fermions in [20]. In order to resolve the causes of this discrepancy, we performed a dedicated $\mathrm{SU}(17)$ calculation at values of the parameters that are very similar to those of ref. [20] ($\beta = 208.45$ vs. $\beta = 208.08$, $12^3 \times 24$ volume vs. 11^4), to enable a direct comparison. Interestingly, setting the scale by the string tension, it turns out that refs. [17, 29] and the present study use a similar lattice spacing as [20]. From this data set, we obtained values of the ρ mass that are compatible with our results at lower N, thus excluding the possibility of some "physical" effect visible only at very large N. We have also monitored the average local value of the Polyakov loop and of the plaquette in the four directions, to check that the whole lattice is in the phase relevant for the continuum limit of the large-N theory. As a consequence of this analysis, the possible sources of the discrepancy can be narrowed down to

- large lattice artifacts in [19, 20]. In fact, while the two simulations use different fermion discretizations for the Dirac operator, the authors of [19, 20] have not performed a continuum limit extrapolation as we did.
- possible contamination from excited states. While we employ a variational method to isolate higher mass resonances, the computation in [19, 20] is based on a single pole fit of the propagator, under the assumption that excited states are removed simply through smearing. If such removal is not complete, the fitted masses might be driven towards higher values. It is interesting to notice that this hypothesis could explain why the discrepancies are more accentuated for their ρ mass (which is very close to our first excited state mass $m_{\rho^\star} = 3.696(54)\sqrt{\sigma}$) than for F_π. In fact, the mass gap between the pion and $\pi^\star$ is higher than between ρ and $\rho^\star$, so that the F_π extraction might be less influenced by excited states.

6.2. Comparison with analytical models

Part of the motivation for studying the meson spectrum in the large-N limit comes from the Maldacena conjecture [3–5], namely from the expectation that gauge theories admit a dual description in terms of string theories, defined in a higher-dimensional

spacetime. In particular, the gauge/gravity duality, also known as "holography", relating quantities between the two types of theories states that, when the number of color charges in the gauge theory tends to infinity, the string coupling g_s in the dual string theory tends to zero. Under these conditions, loop effects on the string side of the correspondence can be neglected, i.e. the theory reduces to its "classical string" limit. Moreover, if the gauge string is strongly coupled, its string dual reduces to a weakly coupled classical gravity theory, which can be treated analytically.

Before reviewing the holographic results to meson spectra in the large-N limit, however, we would like to warn the reader that these types of computations are not yet at a level of accuracy which enables precise comparison with lattice results (or with experimental data). Although the gauge/string correspondence has led to dramatic theoretical progress in several aspects of strongly coupled field theories, its application to *quantitatively* address questions of a direct, phenomenological relevance is still limited and the theoretical predictions discussed in this context should be taken with a grain of salt.

The Sakai-Sugimoto model [67] is one of the most developed top-down holographic approaches, which reproduces many phenomena that characterize low-energy QCD, such as confinement and chiral symmetry breaking, and allows a prediction for meson masses. According to this model, the ratio between the squared masses of the states with the quantum numbers corresponding to the $a_1(1260)$ and the ρ mesons turns out to be:

$$\frac{m^2_{a_1(1260)}}{m^2_\rho} \simeq 2.4, \tag{6.3}$$

which is compatible with the experimental unquenched $N = 3$ value $2.5(1)$ [68]. This value can also be compared to our result for this quantity, extrapolated to the chiral, large-N and continuum limits, which is $3.0(2)$.

A less favorable comparison holds for the ratio of the fundamental and first excited states in the vector channel:

$$\frac{m^2_{\rho(1450)}}{m^2_\rho} \simeq 4.3. \tag{6.4}$$

While the experimentally observed value for this quantity is $3.57(12)$ [68], our $N = \infty$ result reads $4.8(2)$. Regarding the (isovector) scalar channel, the prediction of this model reads:

$$\frac{m^2_{a_0(1450)}}{m^2_\rho} \simeq 4.9, \tag{6.5}$$

to be compared with the real-world value $3.61(9)$ [68]. Our result, extrapolated to vanishing quark mass and for $N \to \infty$, is $6.7(3)$.

The dependence of the ρ vector meson mass on the mass of the pion has been calculated in the holographic study of ref. [69], where the authors find,

$$\frac{m_\rho(m_\pi)}{m_\rho(0)} \simeq 1 + 0.307 \left[\frac{m_\pi}{m_\rho(0)}\right]^2 . \tag{6.6}$$

Our numerical result for the same quantity in the large-N limit, i.e. 0.360(64), reported in eq. (4.28), is remarkably close to the above expectation.

Finally, we mention that a different type of strategy for holographic studies was pioneered in refs. [70, 71]: it goes under the name of "AdS/QCD", and consists of constructing a gravity dual in a curved higher-dimensional (typically: five-dimensional) space, reproducing the known features of QCD. Contrary to the constructions mentioned above, here one follows the so called "bottom-up" approach, which does not care so much about string-theoretic justifications, but provides phenomenological effective models that incorporate the key ingredients of holographic gauge theories and that yield rather accurate predictions for certain physical quantities.

As an example we mention ref. [70], where the authors carry the analysis with two different methods. One possibility is to fix the values of the free parameters of the model, by setting the masses of π and ρ, and the pion decay constant to their physical values. This led to the predictions:

$$m_{a_1(1260)} = 1363\ \text{MeV}, \quad \tilde{F}_\rho = (329\ \text{MeV})^2 \tag{6.7}$$

(note that, upon conversion to our notations, this corresponds to $f_\rho = 198$ MeV). Alternatively, one can perform the best fit for all of the seven parameters simultaneously, which results in:

$$\begin{aligned} m_\pi = 141\ \text{MeV}, \quad m_\rho = 832\ \text{MeV}, \quad m_{a_1(1260)} = \quad 1220\ \text{MeV}, \\ F_\pi = 84\ \text{MeV}, \quad \tilde{F}_\rho = (353\ \text{MeV})^2 \end{aligned} \tag{6.8}$$

(which, in our conventions, would correspond to $f_\rho = 212$ MeV).

In principle, these values can also be compared to our results extrapolated to the large-N limit. Note, however, that, given that the parameters of this model involve input from experimental (i.e. $N = 3$, unquenched) data, the values obtained for $N \to \infty$ are not necessarily expected to be in better agreement than those for $N = 3$. However, our lattice computations at different values of N can provide helpful insights into the consistency of the model. Since the holographic construction is based on the approximation of an infinite number of colors, the lattice results can reveal the quantitative impact of corrections due to the finiteness of N, and therefore provide a non-trivial test of the validity of the model. Our results reveal that, in most cases, the finite-N corrections evaluated at $N = 3$ amount for relative corrections well below 10%.

6.3. Comparison with chiral perturbation theory

Chiral perturbation theory (χPT) [72–77] is an effective low-energy theory describing the dynamics of the lightest mesons in QCD. It relies on the parametric separation of the chiral symmetry breaking scale $\sim 4\pi F_\pi$ and the (nearly) zero mass of the (pseudo-) Goldstone bosons. In the case of a QCD-like theory with n_f flavors of light quarks, χPT describes the fields associated with the light mesons, in terms of the components of a field taking values in $\mathrm{SU}(n_f)$. Its dynamics is governed by an effective Lagrangian (constrained by the symmetries of the theory), which can be organized in a systematic expansion, according to the number of derivatives and of factors involving a possible explicit mass term, in which the coefficients of the different terms are low-energy constants (LECs), whose numerical values can be fixed using phenomenological input, and compared with the expectations from large-N counting rules. In particular, inspection of the terms contributing to the lowest order shows that the effective Lagrangian is proportional to the square of the pion decay constant, i.e. to N. Essentially, this implies that, for $N \to \infty$, the effective theory for light mesons becomes exact at tree level.

While a systematic comparison of large-N χPT predictions with lattice results (including, in particular, the study of the N-scaling of various LECs) is a task that would go way beyond the scope of the present work, for our present purposes it is worthwhile mentioning refs. [57–61], in which the N-dependence of the masses for some of the mesons presented here was investigated in χPT. These studies address the full theory with sea quarks. In this case meson masses tend to increase with the number of colors relative to $\hat{F}_\infty = \sqrt{3/N} F_\pi(0)$, as opposed to our quenched results. The present work and χPT results can be compared by studying ratios of quantities defined at $N = \infty$, where both theories are quenched. Comparing our results shown in table 5.1 and 5.4 with those in refs. [57–61] we find a discrepancy of up to about 30%, although the systematics of their approach are hard to estimate, in particular because experimental data are only available for $N = 3$. Nonetheless, we think the comparison is good enough to discard a purely accidental agreement:

$$\frac{m_\rho}{F_\pi} = \frac{m_{a0}}{F_\pi} = 8.89 \tag{6.9}$$

$$\frac{m_{a1}}{F_\pi} = \frac{m_{\pi\star}}{F_\pi} = 12.57 \tag{6.10}$$

$$\frac{f_\rho}{F_\pi} = 1.99 \tag{6.11}$$

to be compared with our $m_\rho/F_\infty = 8.77(82)$, $m_{a0}/F_\infty = 9.9(17)$, $m_{a1}/F_\infty = 15.1(17)$, $m_{\pi\star}/F_\infty = 15.70(34)$ and $f_\rho/F_\infty = 3.23(31)$. Interestingly, their prediction on the mass degeneracy of (ρ, a_0) and $(a_1, \pi^\star)$ seems to be compatible with our lattice result, although further simulations are required to verify this statement.

7 Conclusion

The large-N limit of QCD is an interesting approach to the theory of strong interaction, where one studies the physical $N = 3$ case as a $1/N$ expansion around the $N \to \infty$ case. Although many simplifications occur in the theory, the limit is still far from trivial and an analytical determination of non-perturbative observables is still an open issue. Lattice QCD is by now a mature field that provides a first-principles framework for numerical predictions and it can easily be extended to the study of a generic $\mathrm{SU}(N)$ gauge group. The results obtained from numerical simulations are crucial to test the validity of the entire large-N approach, employed by many effective field theories and models. These in fact are based on the main assumptions that the large-N limit is close to the $N = 3$ case and $1/N$ corrections are small.

In this work we refine the state-of-the-art for large-N meson spectrum computations: while previous works were limited to a few gauge groups at coarse lattice spacings, addressing mainly pions and rho mesons, we have computed decay constants, the chiral condensate as well as the ground and first excited state masses of mesons by simulating on the lattice the $N = 2, 3, 4, 5, 6, 7$ and 17 quenched theories. Extrapolating our quenched results to $N \to \infty$, we provide results in the chiral limit as well as at physical light and strange quark masses. In all channels but the scalar the dependence on the number of colors for $N \geq 3$ is mild, and the corrections are well parameterised by an expansion in $1/N^2$. The deviations from real-world QCD are found to be minor for the ground states, while they reach up to 20% for the excited states.

We detect statistically significant quenched chiral logarithms of the pion mass for $N \leq 4$ which can be described by a δ-parameter [42]: $m_\pi^2 \propto m_q^{1/(1+\delta)}$ as $m_q \to 0$. The observed rapid decay of δ towards large N-values suggests in this case the subleading

$1/N^3$ contribution to dominate over the leading $1/N$ contribution at $N = 3$.

Sources of possible systematic errors, like finite size effects, continuum limit deviations and non-perturbative values of the renormalization constants, are for the first time under control and allow us to extract combined large-N, $a \to 0$ results for the ground state meson spectrum. We find strong $O(a)$ corrections to the rho and the scalar channels, which lead the latter to be almost degenerate with the vector particle. This is of particular relevance to the phenomenology of scalar mesons [57–61]. Lattice spacing corrections to heavier particles seems to be milder.

We also clarified a discrepancy among previous studies: our results for the ρ meson mass for $\mathrm{SU}(17)$ are compatible with the large-N extrapolation of studies carried out for smaller values of N [16–18,29], and are in contrast to the findings obtained in ref. [20] at $N = 17, 19$ using different techniques. After ruling out the possible sources of systematic errors, we conclude that the disagreement of ref. [20] with the rest of the literature is due to technical aspects of that study.

Finally, we compared our numerical results with analytical predictions, including some derived from holographic models, finding qualitative agreement. Our results for the masses of various states (expressed in units of the ρ meson mass) exhibit a systematic tendency towards values which are larger than those obtained from holographic computations. Most of these models, which are based on the $N = \infty$ approach, take however as input the physical $N = 3$ experimental mass values. We believe that instead our results should be used as inputs to constrain and improve such models.

This work has been supported by the EU ITN STRONGnet (grant 238353) and by the German DFG (SFB/TR 55). The simulations were performed on the Athene and iDataCool clusters in Regensburg, at LRZ Munich and on the Swansea BlueGene/P system.

A
Grassmann variables

Grassmann variables are defined as anticommuting numbers, i.e. for a given set of $\eta_1, \ldots, \eta_n$ Grassmann numbers and a generic z complex number we have the following rule:

$$\eta_i \eta_j = -\eta_j \eta_i \quad ; \quad \eta_i z = z \eta_i \tag{A.1}$$

from which it derives that $\eta_i^2 = 0$ and that the Taylor expansion of a generic function $f(\eta_1, \ldots, \eta_n)$ is finite:

$$f(\eta_1, \ldots, \eta_n) = z^{(0)} + \sum_{i=1}^{n} z_i^{(1)} \eta_i + \sum_{i=1}^{n} z_{ij}^{(2)} \eta_i \eta_j + \cdots + z^{(n)} \eta_1 \eta_2 \ldots \eta_n \tag{A.2}$$

For example,

$$\exp(z\eta) = \sum_{n=0}^{\infty} \frac{(z\eta)^n}{n!} = 1 + z\eta \tag{A.3}$$

Partial differentiation is defined as,

$$\frac{\partial}{\partial \eta_i} \eta_j = \delta_{ij} \quad ; \quad \frac{\partial}{\partial \eta_i} z = 0 \quad ; \quad \frac{\partial}{\partial \eta_k} \eta_i \eta_j = \delta_{ik} \eta_j - \delta_{kj} \eta_i \tag{A.4}$$

while integration also follows similar rules,

$$\int d\eta_i \eta_j = \delta_{ij} \quad ; \quad \int d\eta_i z = 0 \quad ; \quad \int d\eta_k \eta_i \eta_j = \delta_{ik} \eta_j - \delta_{kj} \eta_i \tag{A.5}$$

the latter of which could be interpreted as an integration by parts. Under these definitions, given two sets of anticommuting variables $\bar{\eta}_i$ and η_i one can derive the integration formula,

$$I[M] = \prod_i^n \int d\eta_i d\bar{\eta}_i \exp\left(-\bar{\eta}_j M_{jk} \eta_k\right) = \det M \tag{A.6}$$

in fact, in the expansion of the exponential only the nth term $\left(\bar{\eta}_j M_{jk} \eta_k\right)^n / n!$ survives. This in turn can be expanded and only the terms which are linear in every $\bar{\eta}$ and η contribute. The latter can be reorganized to the form:

$$\begin{aligned} I[M] &= \prod_i^n \int d\eta_i d\bar{\eta}_i \left(\bar{\eta}_i \eta_i\right) \sum_{\{\alpha,\beta\}} \epsilon_{\alpha_1 \ldots \alpha_n} \epsilon_{\beta_1 \ldots \beta_n} M_{\alpha_1 \beta_1} \ldots M_{\alpha_n \beta_n} \\ &= \det M \end{aligned} \tag{A.7}$$

where the ϵ's give the sign of the permutation required to put the products $(\bar{\eta}_i \eta_i)$ in the right order.

Lastly, we want to introduce the concept of the trace of operators when Grassmann variables are involved. For this we first introduce a convenient basis for the Hilbert space, given by the vacuum state $|0\rangle$ and the one particle state $|1\rangle$, on which the operators of creation and annihilation ($a^\dagger$ and a) act according the usual rules:

$$a|0\rangle = 0 \quad ; \quad a|1\rangle = |0\rangle \quad ; \quad a^\dagger|1\rangle = 0 \quad ; \quad a^\dagger|0\rangle = |1\rangle \tag{A.8}$$

We then introduce the coherent states,

$$|\eta\rangle = \exp(-\eta a^\dagger)|0\rangle = (1 - \eta a^\dagger)|0\rangle = |0\rangle - \eta|1\rangle \tag{A.9}$$

named this way for being eigenstates of the annihilation operator:

$$a|\eta\rangle = a|0\rangle - a\eta|1\rangle = \eta a|1\rangle = \eta|0\rangle = \eta|0\rangle - \eta^2|1\rangle = \eta|\eta\rangle. \tag{A.10}$$

For consinstency we define as well $\langle\eta| = \langle 0| - \langle 1|\bar{\eta}$.

Under this definitions, we can define the identity operator,

$$\begin{aligned} \mathbb{1} &= \int d\bar{\eta} d\eta \exp(-\bar{\eta}\eta) |\eta\rangle\langle\eta| = \int d\bar{\eta} d\eta (1 - \bar{\eta}\eta) \left(|0\rangle - \eta|1\rangle\right) \left(\langle 0| - \langle 1|\bar{\eta}\right) \\ &= |0\rangle\langle 0| + |1\rangle\langle 1| \end{aligned} \tag{A.11}$$

and the trace of a given operator A,

$$\begin{aligned} \mathrm{Tr}\, A &= \int d\bar{\eta} d\eta \exp(-\bar{\eta}\eta) \langle -\eta | A | \eta \rangle \\ &= \int d\bar{\eta} d\eta (1 - \bar{\eta}\eta) \left(\langle 0| + \langle 1|\bar{\eta}\right) A \left(|0\rangle - \eta|1\rangle\right) \\ &= \langle 0|A|0\rangle + \langle 1|A|1\rangle \end{aligned} \tag{A.12}$$

The need of the minus sign in $\langle -\eta | A | \eta \rangle$ in order to reproduce the correct trace is at the origin of the anti-periodic boundary conditions in the time direction.

B
Updating methods

B.1. Heatbath

The heatbath algorithm is a generic term for any method which selects a new link U' with a probability $P_c(U')$ in a way which only depends on the other degrees of freedom of the system (that act as a heat bath for the variable being updated, hence the name of the algorithm), but not on the previous value U of the link variable itself. Heatbath updates are more efficient than the Metropolis steps method, because they reduce the correlation between the new and the old value for a given degree of freedom that is updated, therefore heat bath update methods give more rapid equilibration and shorter correlation times.

In order to update a configuration of link variables in lattice gauge theory, one replaces each element $U_\mu(n)$ with a new element $U'_\mu(n)$, which is chosen random according the distribution

$$dP(U') \propto e^{-\beta S(U')} dU', \tag{B.1}$$

where dU is the Haar measure and S_U is the contribute of the link U to the action. In this way any new link is taken with the correct Boltzmann weight and the detailed balance equation is automatically satisfied.

For a generic SU(N) group we can write the contribution of a link U to the action as:

$$S_U = -\frac{1}{N}\mathrm{ReTr}(U \sum_\alpha \widetilde{U}_\alpha) = -\frac{1}{N}\mathrm{ReTr}(U\Sigma) \tag{B.2}$$

Where $\widetilde{U}_\alpha$ are called "staples" and are given by the ordered product of the links around the U-shaped contour around the plaquette, taken with the correct orientation.

The heat bath update can be easily done for $\mathrm{SU}(2)$ gauge group, using the Creutz algorithm described in ref. [78], due to the property,

$$\Sigma = \sum_{\alpha} \widetilde{U}_{\alpha} = k\,\overline{U} \quad \text{with} \quad \widetilde{U}_{\alpha}, \overline{U} \in SU(2) \tag{B.3}$$

$$k = \sqrt{\det \Sigma}, \quad \text{with} \quad k \in \mathbb{R} \tag{B.4}$$

This allows to rearrange the the probability distribution as,

$$dP(U) \propto dU\, e^{-\beta S_U} = dU\, e^{\frac{1}{2}\beta k\, \mathrm{ReTr}(U\overline{U})} \tag{B.5}$$

and use the invariance of the Haar measure under group transformation:

$$\int dP(U) = \int dP(U\overline{U}^{-1}) \tag{B.6}$$

By parametrizing the U link in terms of the Pauli matrices σ_k,

$$U = a_0\, \mathbb{1} + i\, a_k \sigma_k \quad ; \quad a_0^2 + |\vec{a}|^2 = 1 \quad ; \quad a_\mu \in \mathbb{R} \tag{B.7}$$

we can then write:

$$dP(U) = dP(U\overline{U}^{-1}) \propto dU\, e^{\frac{1}{2}\beta k\, \mathrm{ReTr}U} = \frac{1}{2\pi^2}\delta(1-a^2) d^4a\, e^{\beta\, k\, a_0} \tag{B.8}$$

The integration over $|\vec{a}|$ can be done using the δ distribution:

$$\delta(1-a^2) d^4a\, e^{\beta\, k\, a_0} = \frac{1}{2} da_0 d\Omega \sqrt{1-a_0^2}\, e^{\beta\, k\, a_0} \tag{B.9}$$

Thus we need to generate a_0 stochastically in the interval [-1,+1] with probability:

$$P(a_0) \sim \sqrt{1-a_0^2}\, e^{\beta\, k\, a_0} \tag{B.10}$$

To do so, we take a random number x from a uniform distribution in the interval $e^{-2\beta k} < x < 1$ and generate a trial a_0:

$$a_0 = 1 + \frac{1}{\beta k} \log(x) \tag{B.11}$$

a_0 is then rejected with probability $1 - \sqrt{1-a_0^2}$, and the process is reiterated until an a_0 is accepted.

The direction of $\vec{a}$ is taken randomly on a S^2 sphere, and can be defined in terms of two random numbers θ and ϕ uniformly distributed in the $0 \leq \theta < 2\pi$ and $-1 \leq \phi \leq 1$ intervals; we set each a_k as:

$$a_1 = \sqrt{(1-a_0^2)(1-\phi^2)} \cos\theta; \tag{B.12}$$

$$a_2 = \sqrt{(1-a_0^2)(1-\phi^2)}\sin\theta; \tag{B.13}$$

$$a_3 = \phi\sqrt{1-a_0^2} \tag{B.14}$$

Now that we have all four a_μ parameters we have determined univocally U and we can update the old link on the lattice with the new link:

$$U'_\mu = U\overline{U} \tag{B.15}$$

As one can notice, no information from the old link has been used to get the new one; yet, the new link matrix is not completely uncorrelated from the old one, since both of them are correlated to the neighbouring links.

Since this method has a high rejection rate for big values of a_0, an improved version of this algorithm has been developed in refs. [79] [80], to increase the acceptance rate at the price of using more random numbers and computer-operations.

B.2. Updates for SU(N) with $N \geq 3$

For $N = 3$ a heat bath method has been developed by Pietarinen in ref. [81], but its extension to $N > 3$ seems to be difficult to implement. What is commonly used instead (even in $\mathrm{SU}(3)$ computations) is the Cabibbo-Marinari algorithm [85], which consists of updating each link $U \in SU(N)$ by multiplying it by a matrix taken from an SU(2) subset of SU(N). One selects a set,

$$F : \{SU(2)_k, k = 1, \ldots, m\} \tag{B.16}$$

such that there is no left ideal, i.e. no subset of SU(N) which is invariant under left multiplication by F. A minimal set F can be the one obtained by taking elements of the form :

$$g_k = \begin{pmatrix} 1 & & & & 0 \\ & \ddots & & & \\ & & \boxed{a_k} & & \\ & & & \ddots & \\ 0 & & & & 1 \end{pmatrix}, \tag{B.17}$$

where $g_k \in$ SU(N) while $a_k \in$ SU(2) is a 2x2 matrix. Then at each step of the iteration the old link U is multiplied by the g_k matrices,

$$U' = \prod_k g_k U \tag{B.18}$$

and then replaced by U'. In this way the contribution to the action of a single matrix g_k is

$$S(g_k) = -\frac{1}{N}\mathrm{ReTr}(g_k\Sigma) \tag{B.19}$$

and the g_k matrices can be generated with the same $\mathrm{SU}(2)$ heatbath method discussed above (after extracting only the components involved in the heatbath).

B.3. Overrelaxation

In order to further reduce the autocorrelation time, we use four overrelaxation steps at the end of each heatbath sweep. The overrelaxation algorithm consists in replacing each matrix link with another one that preserves the action. In case of the SU(2) gauge group each link U_{old} contributes as:

$$S_{U_{old}} = \frac{1}{2}\,\mathrm{ReTr}(U_{old}\Sigma) \tag{B.20}$$

This term does not change if we replace U_{old} with:

$$U_{new} = \frac{\Sigma^\dagger}{\sqrt{\det\Sigma}} U_{old}^\dagger \frac{\Sigma^\dagger}{\sqrt{\det\Sigma}}. \tag{B.21}$$

since $\Sigma^\dagger/\sqrt{\det\Sigma} \in$ SU(2). For larger SU(N) groups, the overrelaxation updates can be generalized according to the Cabibbo-Marinari method, or using more refined approaches [86].

An overrelaxation step involves the largest change in the link matrix that leaves the action invariant, so it is plausible that it will increase the rate at which the system spans the phase space. In ref. [87], Teper showed that for physical quantities, such as masses, a mix of overrelaxation and heatbath sweeps decorrelates field configurations significantly faster than pure heatbath steps. Besides, it is convenient to use overrelaxation sweeps to decorrelate the system because one overrelaxation step is faster than an heatbath step.

With a mix of heatbath and overrelaxation steps we could reduce the autocorrelation time [88] of the plaquette to a value of $\tau = 5 - 10$ sweeps, where larger correlations were found for bigger N-values. For safety reasons we saved one configurations every 200 sweeps and we checked afterwards that binning data into blocks of different size during the jackknife procedure leads to comparable error estimates for the masses, thus checking that the configurations are indeed decorrelated.

C
Inverters

Two vectors p_j, p_k are conjugate with respect to a matrix A if $p_j^t A p_k = 0$. Let's assume that we can construct a basis of conjugate vectors,

$$\left\{ p_k \quad / \quad p_j^t A p_k = 0 \quad ; \quad \forall j \neq k \right\} \tag{C.1}$$

such that the solution x to the equation $A\,x = b$ can be written as,

$$x = \sum_k \alpha_k p_k. \tag{C.2}$$

Then inverting A (i.e. finding x) is equivalent to computing all the α_k. These can be simply extracted as,

$$p_j^t A\,x = p_j^t \sum_k \alpha_k p_k = \delta_{jk} p_j^t \alpha_k A p_k = p_j^t b \tag{C.3}$$

$$\alpha_j = \frac{p_j^t b}{p_j^t A p_j}. \tag{C.4}$$

In order to construct a basis of conjugate vectors one employs a method similar to Gram-Schmidt orthonormalization, i.e. starting from an initial guess solution $x_0 = 0$ and an initial vector $p_0 = b$, one defines the residual

$$r_k = b - A x_k \tag{C.5}$$

and generates in succession,

$$p_k = r_k - \sum_{j<k} \frac{p_j^t A r_k}{p_j^t A p_j} p_j \tag{C.6}$$

Calculating eq. (C.6) requires the creation of a Krilov subspace,

$$\mathcal{K}_r(A, b) = \left\{b, Ab, A^2b, \ldots, A^{r-1}b\right\} \tag{C.7}$$

and since A is a large matrix, this is usually very expensive. For this reason one sets a target precision ε and stops the algorithm once

$$|r_k|^2 < \varepsilon. \tag{C.8}$$

The method described so far takes the name of Conjugate Gradient, as it requires minimizing the functional

$$Q(x) = \frac{1}{2}x^t Ax - x^t b, \tag{C.9}$$

i.e. finding the point $x^\star$ for which its gradient vanishes:

$$\partial Q(x^\star) = Ax^\star - b = 0. \tag{C.10}$$

Strictly speaking, this method works only for positive definite[1] Hermitian matrices A, however an extension of this method (called BiCGStab [89, 90]) can be applied to the Dirac matrix case.

[1] Positive definiteness requires $z^\dagger Mz = r$ with $r \in \mathbb{R}$ and $r > 0$ for any non-zero z.

D
Renormalization constants

D.1. The Rome-Southampton method

To calculate the renormalization constants we used the so-called Rome-Southampton method [91], which we briefly summarize below, following the notation of ref. [49]. Given a generic bilinear operator $O^\Gamma = \bar{\psi}\Gamma\psi$ we compute the renormalization constant Z_Γ by imposing the condition,

$$\frac{1}{4N} Z_\Gamma \, \mathrm{Tr} \, \left[\langle p|O^\Gamma|p\rangle \langle p|O^\Gamma|p\rangle_0^{-1} \right] = 1 \tag{D.1}$$

for vanishing quark masses at $p^2 = \mu^2$ where μ is the renormalization scale. The element $\langle p|O^\Gamma|p\rangle$ is computed from the lattice using the non-amputated Green function $G(p)$ and the quark propagator $S(p)$ in momentum space as,

$$\langle p|O^\Gamma|p\rangle = \frac{1}{Z_\psi} S^{-1}(p) G_\Gamma(p) S^{-1}(p), \tag{D.2}$$

while $\langle p|O^\Gamma|p\rangle_0 = \Gamma$ is the tree level matrix element. The $4N \times 4N$ matrices $G(p)$ and $S(p)$ are obtained by,

$$G(p) = \frac{1}{V} \sum_{x,y,z} e^{-ip(x-y)} \left\langle q(x) O^\Gamma(z) \bar{q}(y) \right\rangle \tag{D.3}$$

$$S(p) = \frac{1}{V} \sum_{x,y} e^{-ip(x-y)} \left\langle q(x) \bar{q}(y) \right\rangle \tag{D.4}$$

Finally, Z_ψ is the quark field renormalization constant given by,

$$Z_\psi = \frac{\mathrm{Tr}\,\left[-i\sum_\nu \gamma_\nu \sin(ap_\nu) S^{-1}(p)\right]}{4N\sum_\lambda \sin^2(ap_\lambda)}. \tag{D.5}$$

Ideally the procedure described above should be implemented in the window,

$$\frac{1}{L^2}\,,\ \Lambda^2_{QCD} \ll \mu^2 \ll \frac{1}{a^2} \tag{D.6}$$

where $\Lambda^2_{QCD} \ll \mu^2$ ensures that non perturbative effects are suppressed, while $\mu^2 \ll 1/a^2$ should keep the lattice artifacts small. In practice the latter inequality is often [92, 93] violated and lattice artefacts need to be subtracted in the fits (see below). It is important to perform gauge fixing of our lattice configurations, in order to compare our results to the corresponding continuum quantities calculated in the same gauge. In this work we calculate the renormalization constants in the Landau gauge, which has been fixed using the methods described in Appendix E.

We studied the following bilinear operators (scalar, pseudoscalar, vector, axial):

$$O^S = \bar\psi\psi \tag{D.7}$$
$$O^P_\mu = \bar\psi\gamma_5\psi \tag{D.8}$$
$$O^V_\mu = \bar\psi\gamma_\mu\psi \tag{D.9}$$
$$O^A_\mu = \bar\psi\gamma_\mu\gamma_5\psi \tag{D.10}$$

for all the $\mathrm{SU}(N)$ groups and for the four central κ-values listed in table 4.2. In the case of $N = 4, 5$ and 7, we also studied these bilinears for the three extra lattice spacings listed in table 5.2 that have been used in the continuum limit extrapolations. We used 20 gauge fixed configurations for each N and each κ and we chose a set of 17 different momenta in the range $a^2p^2 \in [0, 6]$, which were selected minimizing $\sum_\mu (ap_\mu)^4 / \sum_\nu (ap_\nu)^2$ in order to reduce lattice artifacts. Nonetheless, after carrying the analysis, we found huge lattice artefacts for $\mathrm{SU}(17)$, due to the smallest volume employed, so we preferred to use $1/N^2$ extrapolations for $N = 17$ and we omit these results.

For each momentum p^2 we extrapolate the result for $Z_{A,V,S}$ to the chiral limit with a linear fit,

$$Z_{A,V,S}(m_q) = Z_0 + Z_1 m_q \tag{D.11}$$

using a jackknife method for the statistical errors. In the case of Z_P we follow the procedure detailed in [92], where the data are fitted to the expression,

$$\frac{1}{Z_P(m_q)} = \frac{Z_0}{m_q} + Z_1 + Z_2 m_q, \tag{D.12}$$

which takes into account the pole in $m_q = 0$ [94]. Then the inverse of Z_1 is used as the chiral limit extrapolation of Z_P.

Although we used only a small number of configurations, the statistical errors associated to this method are known to be extremely tiny compared to possible systematical errors (for instance, lattice artefacts). This is particularly evident in the case of Z_P; even if we get very precise results, we believe that fitting the pole with only four κ-values, of whom only one in small mass region, is unreliable, with systematics that are hard to assess. To get a quantitative idea of the discrepancies we can combine the results for $A \approx Z_P/(Z_A Z_S)$ of eq. (4.13) from the PCAC mass fit with the ones for Z_A and Z_S obtained from eq. (D.11) in order to obtain a different estimate of Z_P, which we label Z_P^{AWI} (from axial Ward identity). This quantity isn't necessarily a better estimate of Z_P, since in principle eq. (4.13) is affected by m_q^2 corrections. As shown in table D.1, the two estimates of Z_P differ by $\mathcal{O}(10\%)$ and non-perturbative studies for $\mathrm{SU}(3)$ [40] suggest that indeed our Z_P from eq. (D.12) is overestimated (while the other Z_X are indeed consistent). We think that a dedicated work with more points is required in order to get a proper estimate of Z_P, nonetheless, we include for completeness our results. We stress however that we did not use this renormalization constant in any quantity studied.

D.2. Lattice artefacts subtraction for the renormalization constants

In fig. D.1 we show the lattice results of $Z^{lat}_{S,P,A,V}$, calculated on the lattice with the method above, for different values of the momentum $p^2 = \mu^2$. The reader can see from the plots that these quantities show a linear dependence (and logarithmic in the case of $Z_{S,P}$) in the momentum p^2. To get rid of these contributions we follow the procedure indicated in [92, 93] and we fit $Z^{lat}_{A,V}$ to,

$$Z_X^{lat} = Z_X + z_0 S^2(p) + z_1 \frac{S^4(p)}{S^2(p)}, \tag{D.13}$$

with $S^n(p) = \sum_\mu p_\mu^n$ and z_i free parameters. A similar fit is performed for $Z^{lat}_{S,P}$, where in this case we included also a logarithmic term, which is fixed by perturbation theory [50],

$$Z_X^{lat} = Z_X + \frac{3g^2}{16\pi^2}\left(\frac{N^2-1}{2N}\right)\log S^2(p) + z_0 S^2(p) + z_1 \frac{S^4(p)}{S^2(p)}. \tag{D.14}$$

We omit from the fits the points at $\mu^2 < 2a^2$ and we plot in fig. D.2 the values of Z_X^{lat} after the subtraction of the p-dependent terms. As already stated, the statistical errors tend to be extremely small and unreliable, thus we indicate as errors the absolute value of the maximal difference between each of the subtracted points and the plateau constant Z_X. This leads to the results shown in table D.1.

We then proceed into studying the $1/N^2$ dependence of the renormalization constants by use of linear fits, which match well the behaviour (fig.D.3). The fit results at

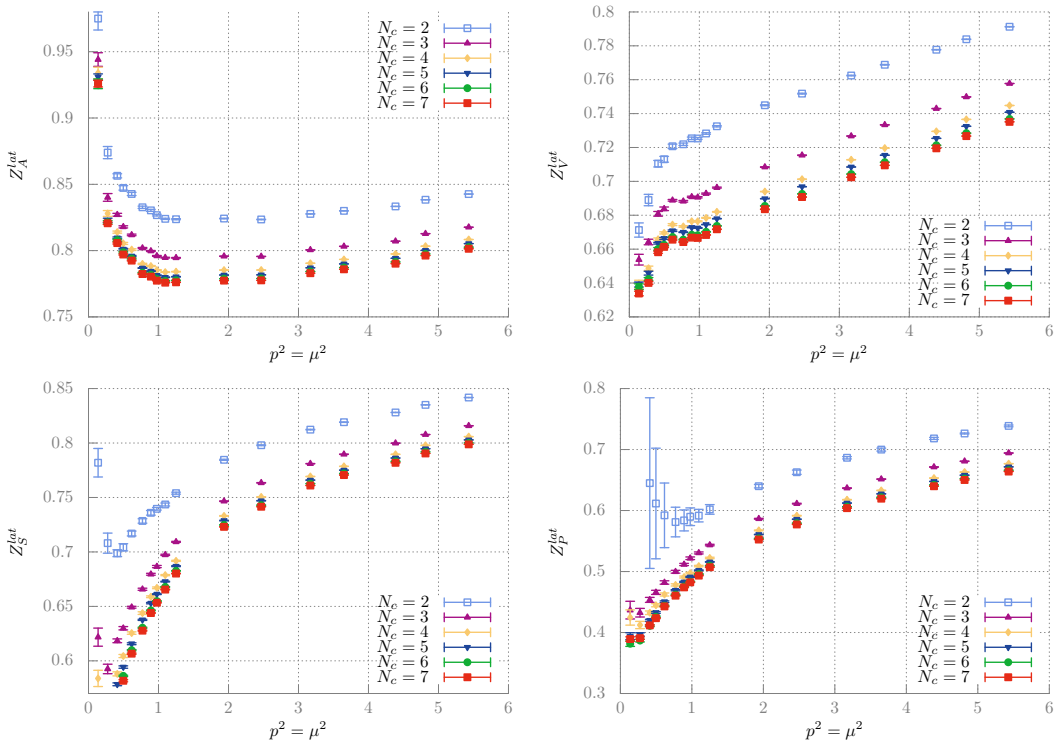

Figure D.1.: Z_X^{lat} results from the lattice at different momenta p^2.

the lattice spacing $a \approx 0.09$ fm are,

$$Z_A(N) = 0.75788(98) + 0.21501(93)/N^2 \quad \text{(D.15)}$$
$$Z_V(N) = 0.64933(40) + 0.28027(43)/N^2 \quad \text{(D.16)}$$
$$Z_S(N) = 0.6790(26) + 0.303(18)/N^2 \quad \text{(D.17)}$$
$$Z_P(N) = 0.4817(27) + 0.425(23)/N^2 \quad \text{(D.18)}$$
$$Z_P^{AWI}(N) = 0.4256(21) - 0.041(23)/N^2 \quad \text{(D.19)}$$

Perturbation theory [50, 51] predicts $Z_X = \alpha_0 + \alpha_1/N^2$ with α_i positive, however its results are known to be quite far (about 25%) from the non-perturbative ones.

We conclude this section by reminding that in order to use the constants $Z_{S,P}$ in the $\overline{\text{MS}}$ scheme (as listed in table D.1) one has to divide by a further conversion factor,

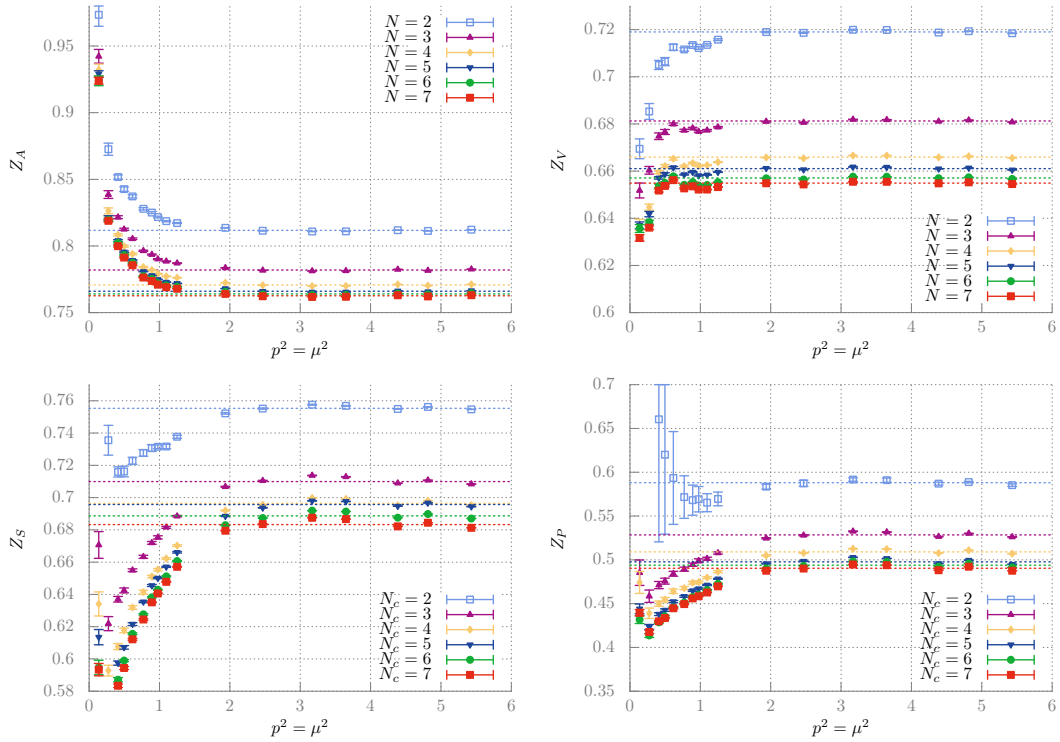

Figure D.2.: Z_X after the $\mathcal{O}(a)$ artifacts subtraction.

$Z_{S,P}^{\overline{\text{MS}}} = Z/C_{S,P}$, where $C_{S,P}$ is listed in [95] as,

$$
\begin{aligned}
g^2 &= \frac{2N}{\beta} \quad ; \quad c_F = \frac{N^2-1}{2N} \quad ; \quad d_1(a\mu) = -\frac{11N}{6\pi}\log(a\mu) - \frac{\pi}{2N} + 2.13573007N \\
d_2(a\mu) &= d_1^2(a\mu) - \frac{34N^2}{24\pi^2}\log(a\mu) + \frac{3\pi^2}{8N^2} - 2.8626216 + 1.2491158N^2 \\
g^\star &= \frac{g^2}{4\pi} + d_1(a\mu)\left(\frac{g^2}{4\pi}\right)^2 + d_2(a\mu)\left(\frac{g^2}{4\pi}\right)^3 \\
C_{S,P} &= 1 - 4c_F\frac{g^\star}{4\pi} + ((57 - 288\zeta(3))c_F - (1285 - 432\zeta(3))N)\frac{c_F}{24}\left(\frac{g^\star}{4\pi}\right)^2
\end{aligned}
\tag{D.20}
$$

In addition to this, one has to evolve Z_S from a scale of $a\mu = 1$ to a (conventional) scale of $\mu = 2$ GeV for a comparison with perturbative results obtained at a similar scale. To

N	Z_A	Z_V	Z_S	$Z_S^{\overline{\rm MS}}(2\,{\rm GeV})$	Z_P	Z_P^{AWI}
2	0.8117(19)	0.71903(92)	0.7553(31)	0.8092(33)	0.5880(45)	0.4188(50)
3	0.7820(16)	0.68126(66)	0.7099(38)	0.7664(41)	0.5285(41)	0.4174(33)
4	0.7707(16)	0.66596(66)	0.6964(45)	0.7533(48)	0.5091(41)	0.4193(34)
5	0.7660(20)	0.66107(71)	0.6957(42)	0.7527(46)	0.4977(52)	0.4290(31)
6	0.7640(16)	0.65709(66)	0.6887(58)	0.7453(63)	0.4939(43)	0.4261(39)
7	0.7626(14)	0.65491(60)	0.6833(42)	0.7396(46)	0.4904(44)	0.4238(29)

Table D.1.: The renormalization constants for different N-values, for $a\sqrt{\sigma} = 0.2093$ ($a \approx 0.09$ fm).

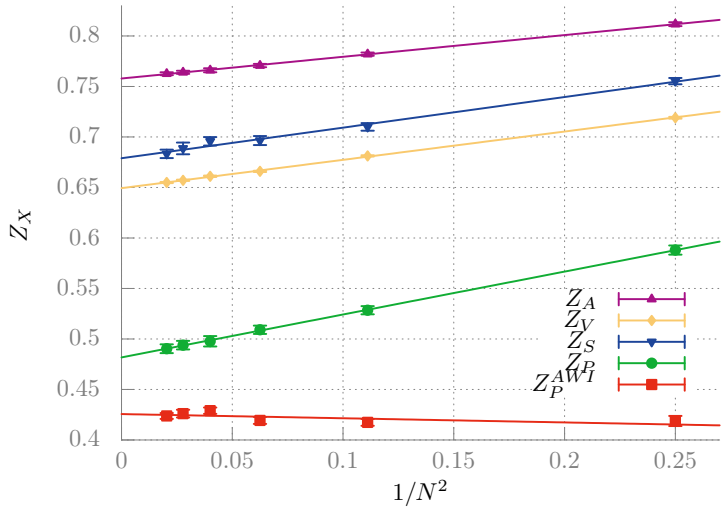

Figure D.3.: $1/N^2$ expansion of the Z_X constants.

achieve this, we use the following equations from ref. [95] for each lattice spacing,

$$Z_S^{\overline{\rm MS}}(\mu) = R(\mu,\mu_0) Z_S^{\overline{\rm MS}}(\mu_0) \tag{D.21}$$

$$R(\mu,\mu_0) = \frac{\exp F\left(\frac{\bar{g}^2(\mu^2)}{16\pi^2}\right)}{\exp F\left(\frac{\bar{g}^2(\mu_0^2)}{16\pi^2}\right)} \tag{D.22}$$

$$\begin{aligned} F(x) = {} & \frac{\gamma_0}{2\beta_0}\log(x) + \frac{\beta_0\gamma_2 - \beta_2\gamma_0}{4\beta_0\beta_2}\log(\beta_0 + \beta_1 x + \beta_2 x^2) + \\ & + \frac{2\beta_0\beta_2\gamma_1 - \beta_1\beta_2\gamma_0 - \beta_0\beta_1\gamma_2}{2\beta_0\beta_2\sqrt{4\beta_0\beta_2 - \beta_1^2}} \arctan\left(\frac{\beta_1 + 2\beta_2 x}{\sqrt{4\beta_0\beta_2 - \beta_1^2}}\right) \end{aligned} \tag{D.23}$$

with the 3-loop quantities,

$$\begin{aligned}\frac{\bar{g}^2(\mu_0^2)}{16\pi^2} &= \frac{1}{\beta_0 \log(\mu^2/\Lambda^2)} - \frac{\beta_1}{\beta_0^3}\frac{\log(\log(\mu^2/\Lambda^2))}{\log^2(\mu^2/\Lambda^2)} + \\ &\quad + \frac{\beta_1^2 \log^2(\log(\mu^2/\Lambda^2)) - \beta_1^2 \log(\log(\mu^2/\Lambda^2)) + \beta_2\beta_0 - \beta_1^2}{\beta_0^5 \log^3(\mu^2/\Lambda^2)} \qquad \text{(D.24)}\\ \beta_0 &= 11N/3 \quad ; \quad \beta_1 = 34N^2/3 \quad ; \quad \beta_2 = \frac{2857N^3}{54} \qquad \text{(D.25)}\\ \gamma_0 &= -\frac{3c_F}{2} \quad ; \quad \gamma_1 = -2\left(\frac{3}{2}c_F^2 + \frac{97}{6}Nc_F\right) \qquad \text{(D.26)}\\ \gamma_2 &= -2\left(\frac{129}{2}c_F^3 - \frac{129}{4}Nc_F^2 + \frac{11413}{108}N^2c_F\right) \qquad \text{(D.27)}\end{aligned}$$

and the $\Lambda^{\overline{\rm MS}}$ given by ref. [7]

$$\frac{\Lambda^{\overline{\rm MS}}}{\sqrt{\sigma}} = 0.515(3) + \frac{0.34(1)}{N^2} \qquad \text{(D.28)}$$

The above procedure has been repeated for each lattice spacings and N-value used in the continuum limit calculation. The renormalization constants thus exctracted are listed in table D.2.

N	β	$a\sqrt{\sigma}$	Z_A	Z_V	Z_S	$Z_S^{\overline{\rm MS}}(2\,\text{GeV})$
4	10.6573	0.31395	0.75578(98)	0.60801(20)	0.65951(73)	0.74543(82)
4	10.8485	0.25116	0.76043(72)	0.64626(28)	0.69258(71)	0.76297(78)
4	11.4462	0.15	0.78455(41)	0.70261(61)	0.7351(17)	0.7718(18)
5	16.96	0.31395	0.74945(92)	0.60621(10)	0.6522(11)	0.7376(12)
5	17.244	0.25116	0.75676(88)	0.64154(25)	0.68763(54)	0.75791(59)
5	18.155	0.15	0.78075(57)	0.69823(24)	0.73804(41)	0.77510(43)
7	33.7312	0.31395	0.7476(15)	0.59855(11)	0.65019(68)	0.73585(76)
7	34.2937	0.25116	0.75202(78)	0.63490(21)	0.68058(95)	0.7505(10)
7	36.08775	0.15	0.77967(90)	0.69151(67)	0.7147(38)	0.7506(40)

Table D.2.: The renormalization constants used in continuum limits calculations.

E
Landau gauge fixing

E.1. Relaxation method

The Landau gauge is defined in the continuum by the local condition,

$$\partial_\mu A_\mu(x) = 0. \tag{E.1}$$

Using the correspondence $U_\mu(x) = \exp(iaA_\mu(x))$, which becomes exact in the continuum limit, the $O(a^2)$ equivalent of eq. (E.1) can be constructed on the lattice as

$$\theta(x) = \frac{1}{N}\mathrm{Tr}\,\Delta(x)\Delta^\dagger(x) = 0, \tag{E.2}$$

where:

$$\Delta(x) = \sum_\mu (A_\mu(x) - A_\mu(x-\hat{\mu})), \tag{E.3}$$

$$A_\mu(x) = U_\mu(x) - U_\mu^\dagger(x) - \frac{1}{N}\mathrm{Tr}\left(U_\mu(x) - U_\mu^\dagger(x)\right). \tag{E.4}$$

In practice a gauge configuration is fixed by means of iterative methods (see ref. [96] for a review) which gradually converge to eq. (E.2) and stop when a desired precision is reached. We required such precision to be $\theta(x) < 10^{-9}$ in each site x, which corresponds (empirically) to an average precision of $\frac{1}{V}\sum_x \theta(x) \approx 10^{-14}$.

One way of fulfilling eq. (E.2) is by iteratively performing the gauge transformation $U'_\mu(x) = g(x)U_\mu(x)g(x+\hat{\mu})^\dagger$ which maximizes the functional,

$$\begin{aligned} F[U,g] &= \frac{1}{NV}\mathrm{ReTr}\sum_x g(x)\sum_\mu \left[U_\mu(x)g(x+\hat{\mu})^\dagger + U_\mu(x-\hat{\mu})^\dagger g(x-\hat{\mu})^\dagger\right] \\ &= \sum_x g(x)K(x) \end{aligned} \tag{E.5}$$

where one obtains $g(x)$ in each step by applying for each $\mathrm{SU}(2)$ subgroup,

$$\begin{aligned} h &= \mathrm{Proj}_{\mathrm{SU(2)}}(\mathrm{g_{old}K}), \\ g_{\mathrm{new}} &= h^\dagger g_{\mathrm{old}}. \end{aligned} \tag{E.6}$$

.

However the loop over the $\mathrm{SU}(2)$ subgroups becomes computationally too expensive in the large-N limit; this rules out the possibility of using over-relaxation techniques where h is replaced by h^ω. In alternative one could skip such loop employing a different projector,

$$\mathrm{Proj}_{\mathrm{SU(N)}}(\mathrm{A}) = \frac{\mathrm{A}}{\sqrt{\mathrm{A}^\dagger\mathrm{A}}}\left[\det\left(\frac{\mathrm{A}}{\sqrt{\mathrm{A}^\dagger\mathrm{A}}}\right)\right]^{1/\mathrm{N}} \tag{E.7}$$

and can obtain $g(x)$ directly as,

$$\begin{aligned} h &= \mathrm{Proj}_{\mathrm{SU(N)}}(\mathrm{K}), \\ g_{\mathrm{new}} &= h^\dagger. \end{aligned} \tag{E.8}$$

.

While this method works fine for $\mathrm{SU}(3)$, we found it to be still too slow for bigger groups at the lattice sizes and at the precision required.

E.2. Fourier accelerated method

In this section we explain an alternative way to tackle the problem, the so called Fourier accelerated method [97], which we implemented and used in this work.

Starting from the continuum, the gauge transformation on the $A_\mu(x)$ field reads,

$$A^g_\mu(x) = A_\mu(x) + \partial_\mu\chi(x). \tag{E.9}$$

By repeating n times this procedure, choosing each time $\chi^{(n)}(x) = \alpha\partial_\nu A^{(n)}_\nu(x)$, one derives the following iterative expression,

$$\partial_\mu A^{(n)}_\mu(x) = \left(1+\alpha\partial^2\right)A^{(n-1)}_\mu(x) \tag{E.10}$$

which can be solved in momentum space with a Fourier transformation $B(p) = \hat{\mathcal{F}}\left(\partial_\mu A_\mu(x)\right)$ and with the substitution $\partial^2 \to -p^2$:

$$B^{(n)}(p) = \left(1 - \alpha p^2\right) B^{(n-1)}(p) = \left(1 - \alpha p^2\right)^n B^{(0)}(p) \tag{E.11}$$

It is clear that if $\alpha < 1/p^2_{\max}$ this procedure will lead to eq. (E.1) for $n \to \infty$ steps,

$$\partial_\mu A_\mu^{(n\to\infty)}(x) = \hat{\mathcal{F}}^{-1}\left(\left(1 - \alpha p^2\right)^\infty B^{(0)}(p)\right) = 0 \tag{E.12}$$

however the components $B(p)$ associated to p^2-values close to zero will converge slowly. A naive way of porting this method to the lattice would be choosing a gauge transformation matrix $g(x)$ as

$$g(x) = \exp\left(\frac{\alpha}{2}\Delta(x)\right), \tag{E.13}$$

however to accelerate the convergence of the slower components, one takes advantage of the Fourier transformation and replaces $\alpha \to \alpha(p) = \alpha/p^2$, i.e.:

$$g(x) = \exp\left[\hat{\mathcal{F}}^{-1}\left(\frac{\alpha}{2}\frac{1}{p^2}\hat{\mathcal{F}}\left(\Delta(x)\right)\right)\right]. \tag{E.14}$$

Then at each step the gauge field is transformed as $U_\mu(x) \to g(x)U_\mu(x)g^\dagger(x+\hat{\mu})$ and the method reiterated until the convergence is reached. For numerical purposes it is faster and sufficient to truncate $g(x)$ at first order in α and project it back to the gauge group. For all the $\mathrm{SU}(N)$ gauge groups we used the recommended [97] $SU(3)$ value $\alpha = 0.08$, as we found times sufficiently small and therefore could not justify a fine tuning of α for each N.

The Fourier accelerated method scales well across the various $\mathrm{SU}(N)$ groups, with the number of iterations in the same order of magnitude across the N-values (see fig. E.1). The only drawback of this method is the implementation of the Fourier transformation, which may become a bottleneck in the case of a large number of CPUs. In our case, due to the small number of configurations, this was not a limiting factor, otherwise it would be recommendable [98] to gauge fix on GPU hardware, where optimized Fourier transform libraries are provided.

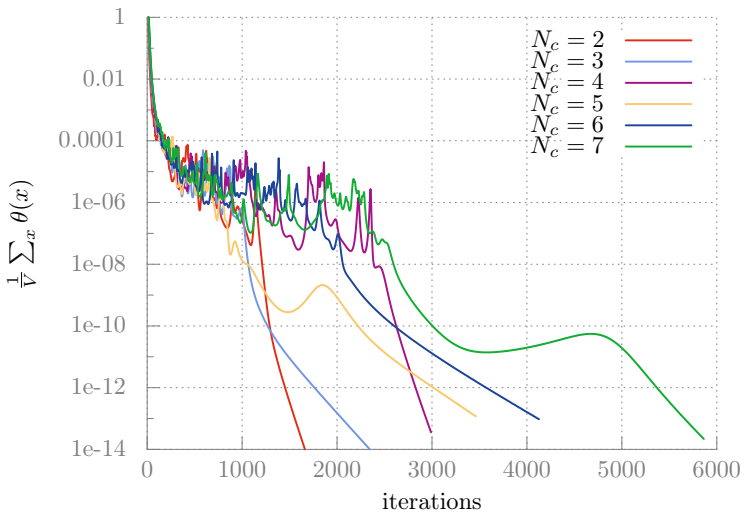

Figure E.1.: Volume-averaged value of $\theta(x)$ for the different $\mathrm{SU}(N)$ groups, with a $24^3 \times 48$ lattice volume. While the convergence depends strongly on the configuration used, for each N we selected a case where the iteration count was close to the respective average.

F

Additional tables and figures

This appendix includes additional tables and figures.

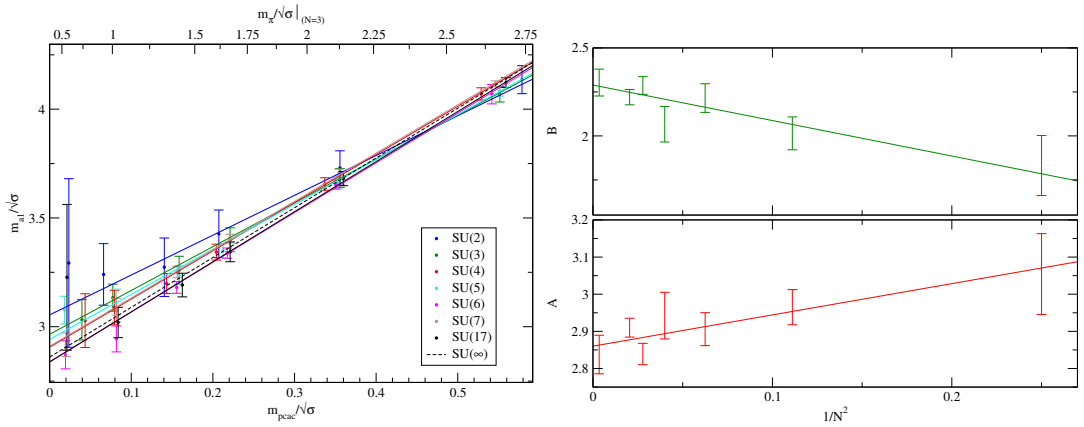

Figure F.1.: Fit of the a_1 mass to: $m_{a_1}/\sqrt{\sigma} = A + B \cdot m_{\mathrm{PCAC}}/\sqrt{\sigma}$ (left) and $1/N^2$ fit of the parameters A and B (right).

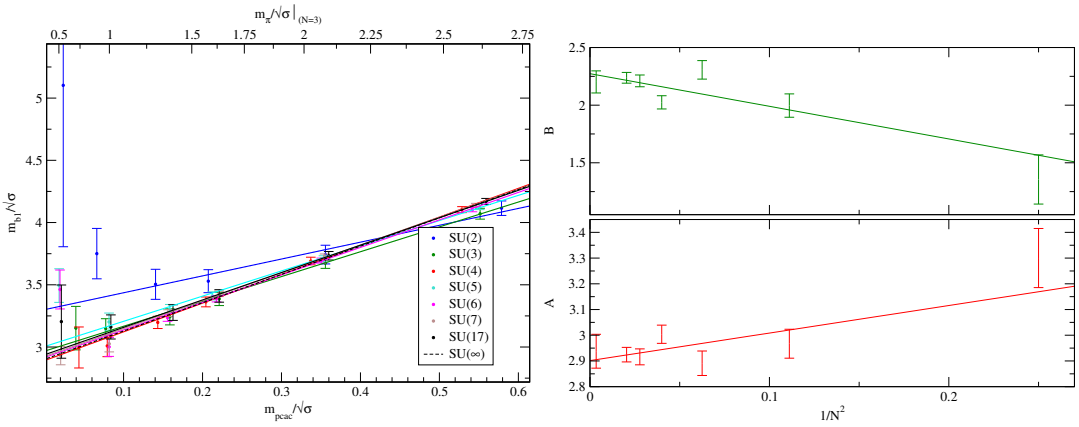

Figure F.2.: Same as figure F.1, but for the mass of the b_1 state.

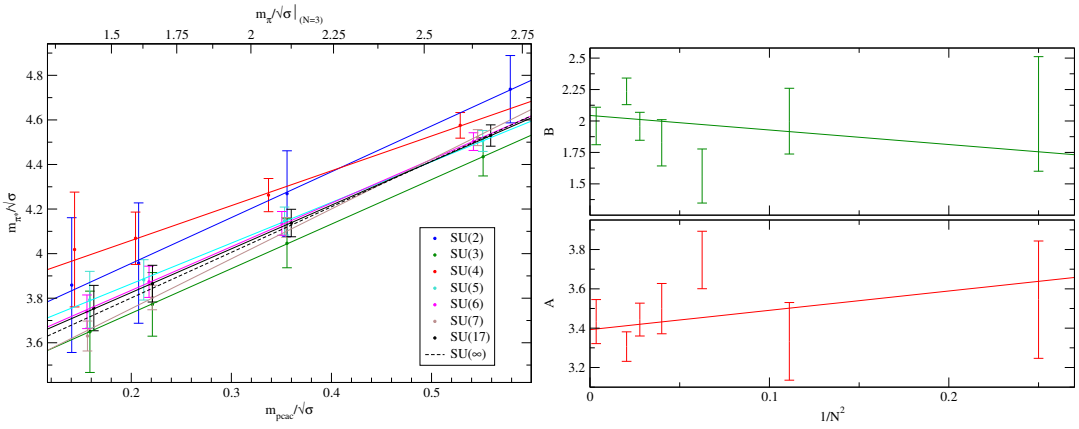

Figure F.3.: Same as figure F.1, but for the mass of the $\pi^\star$ state.

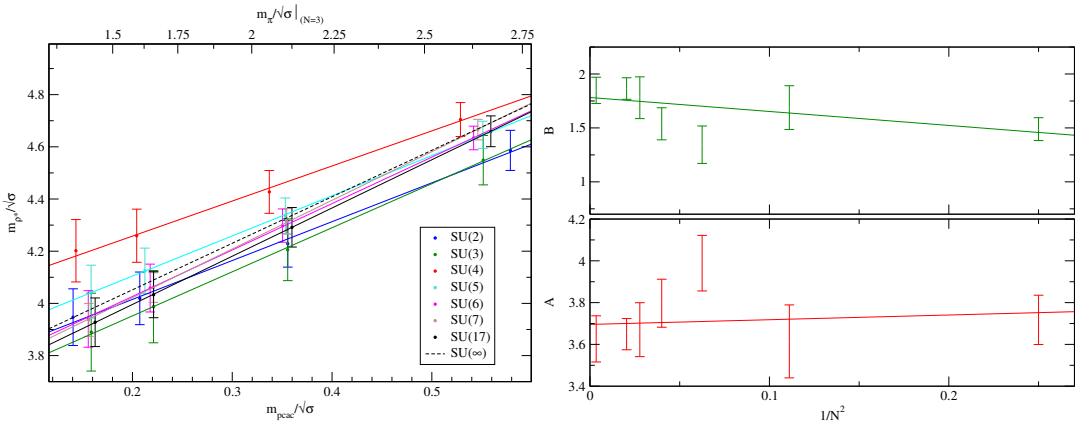

Figure F.4.: Same as figure F.1, but for the mass of the $\rho^\star$ state.

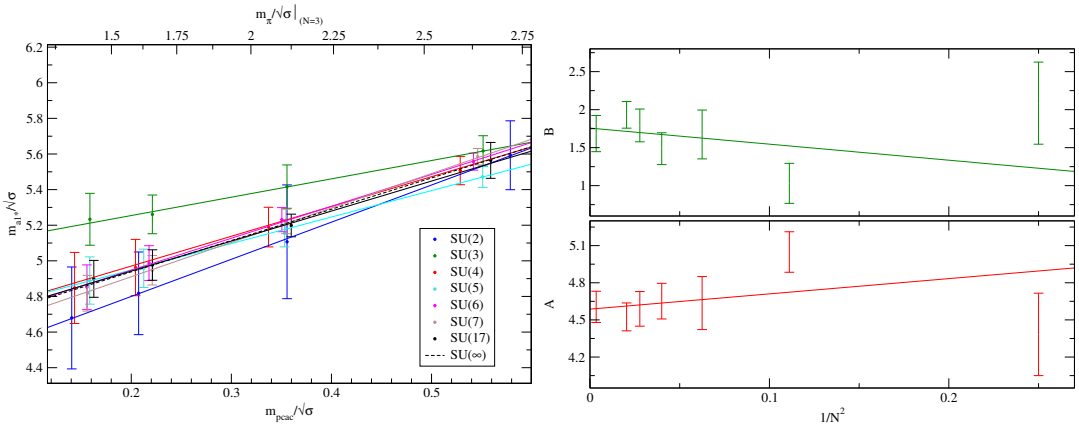

Figure F.5.: Same as figure F.1, but for the mass of the $a_1^\star$ state.

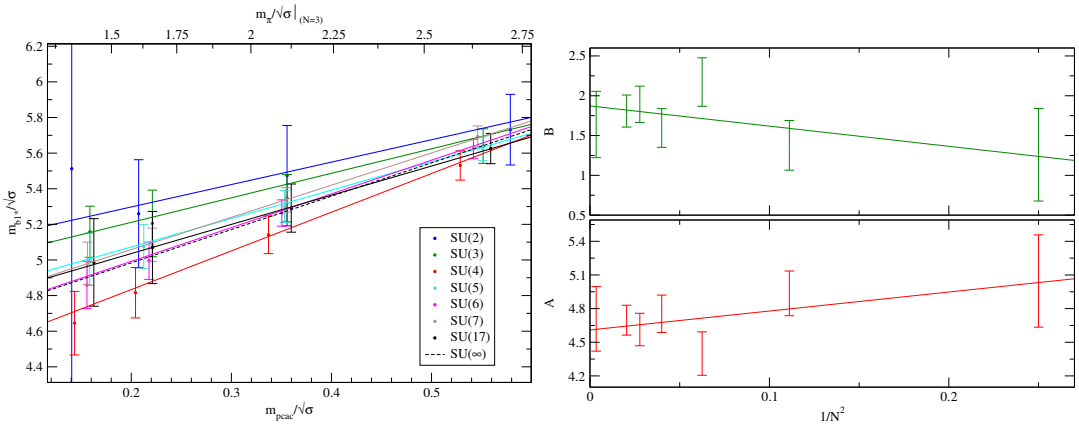

Figure F.6.: Same as figure F.1, but for the mass of the $b_1^\star$ state.

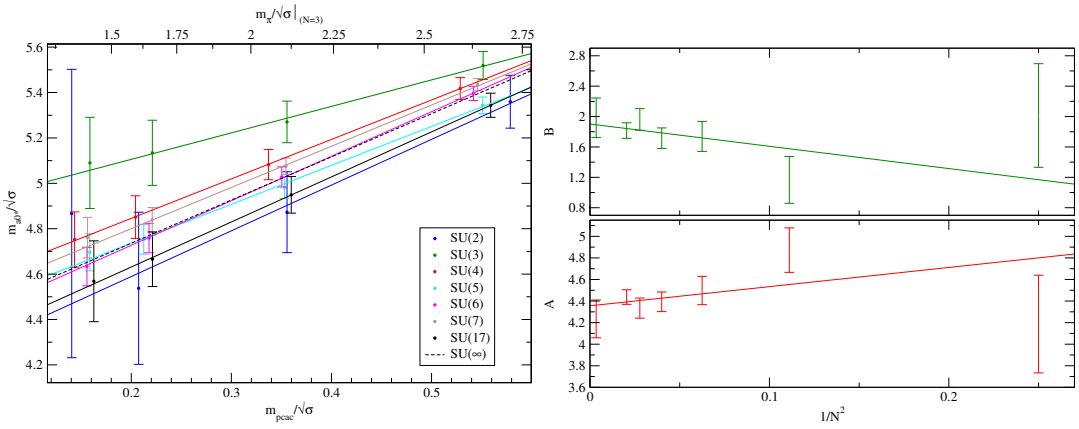

Figure F.7.: Same as figure F.1, but for the mass of the $a_0^\star$ state.

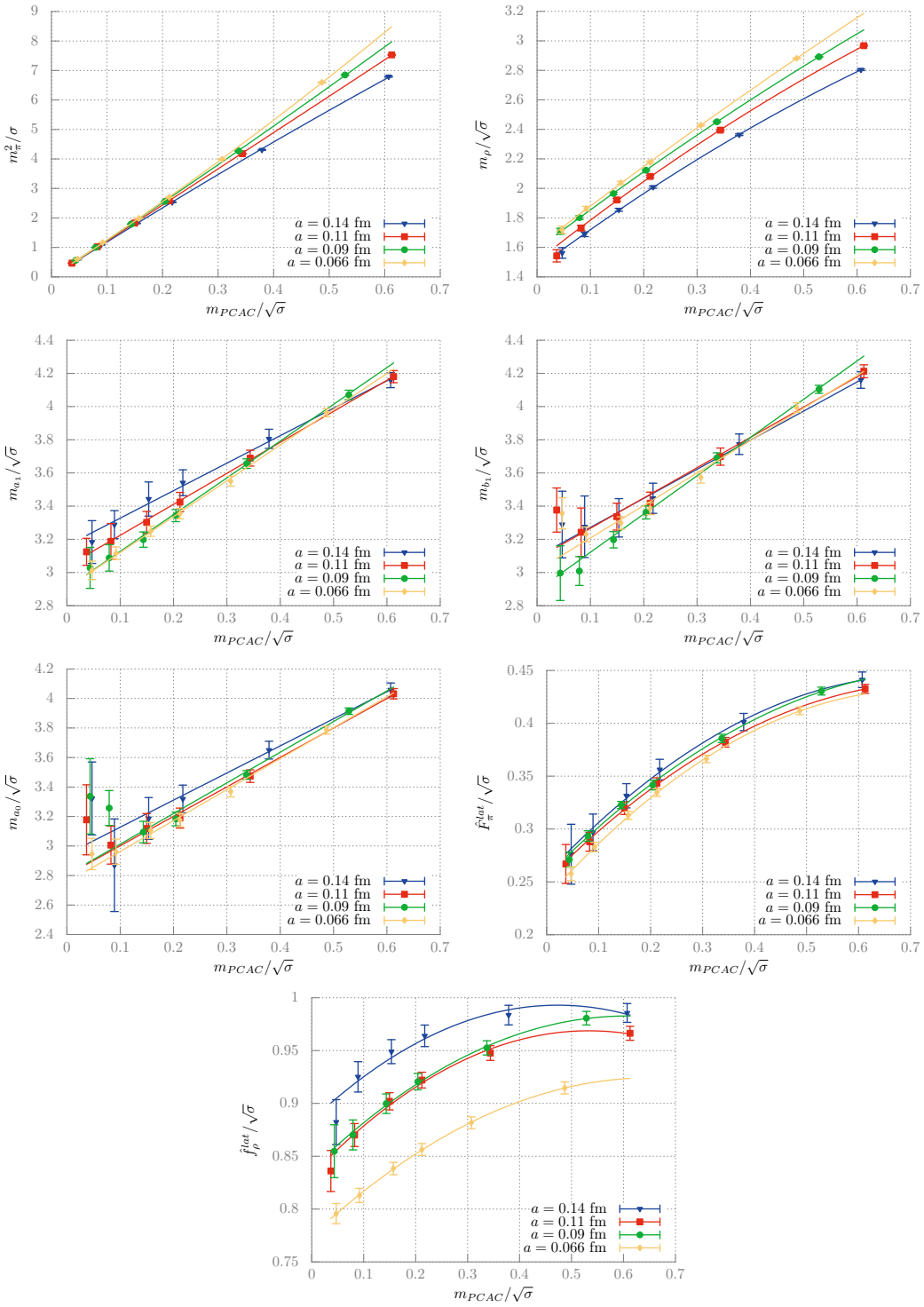

Figure F.8.: Plot of the SU(4) masses and decay constants as a function of m_{PCAC} for different lattice spacings.

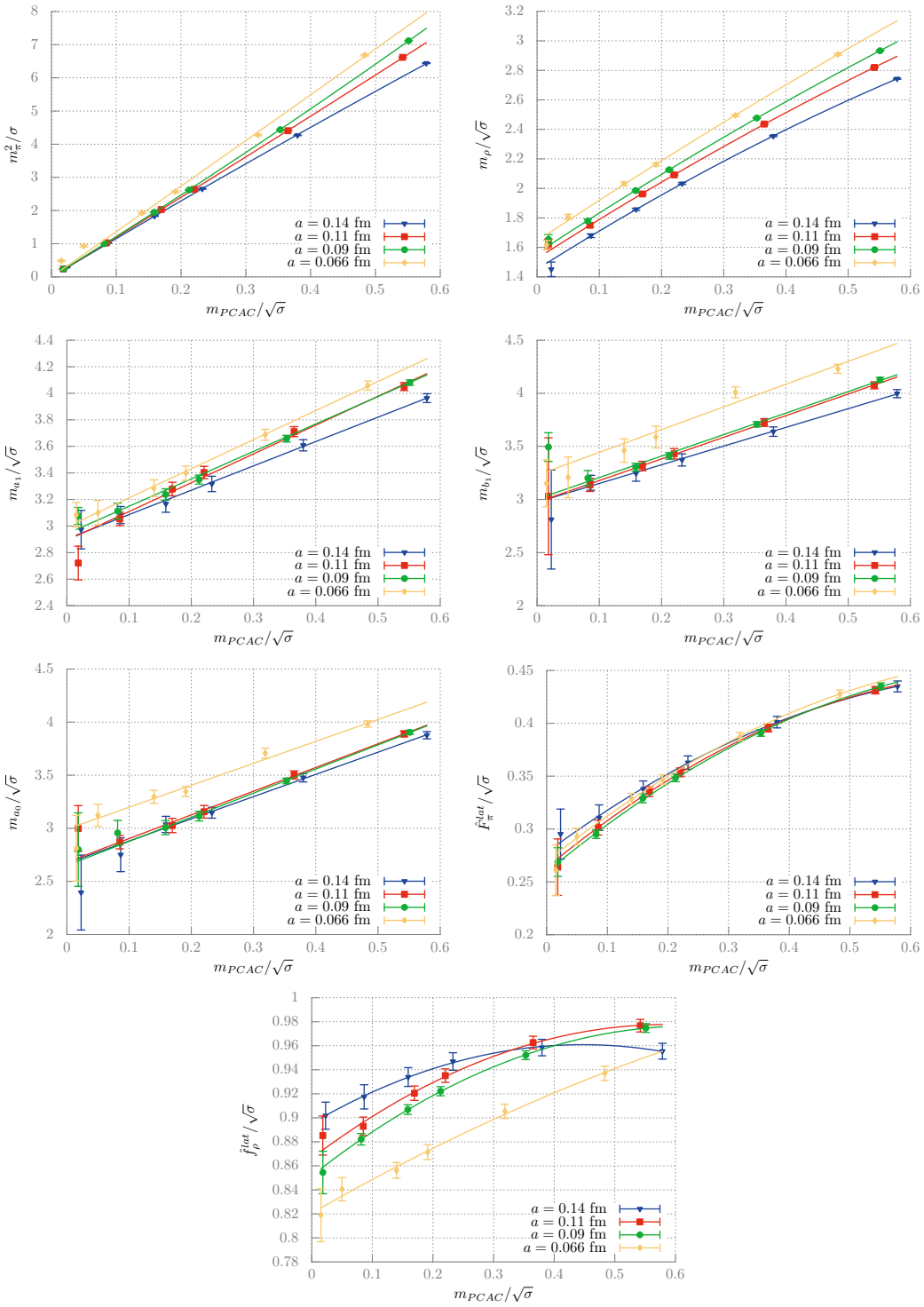

Figure F.9.: Plot of the SU(5) masses and decay constants as a function of m_{PCAC} for different lattice spacings.

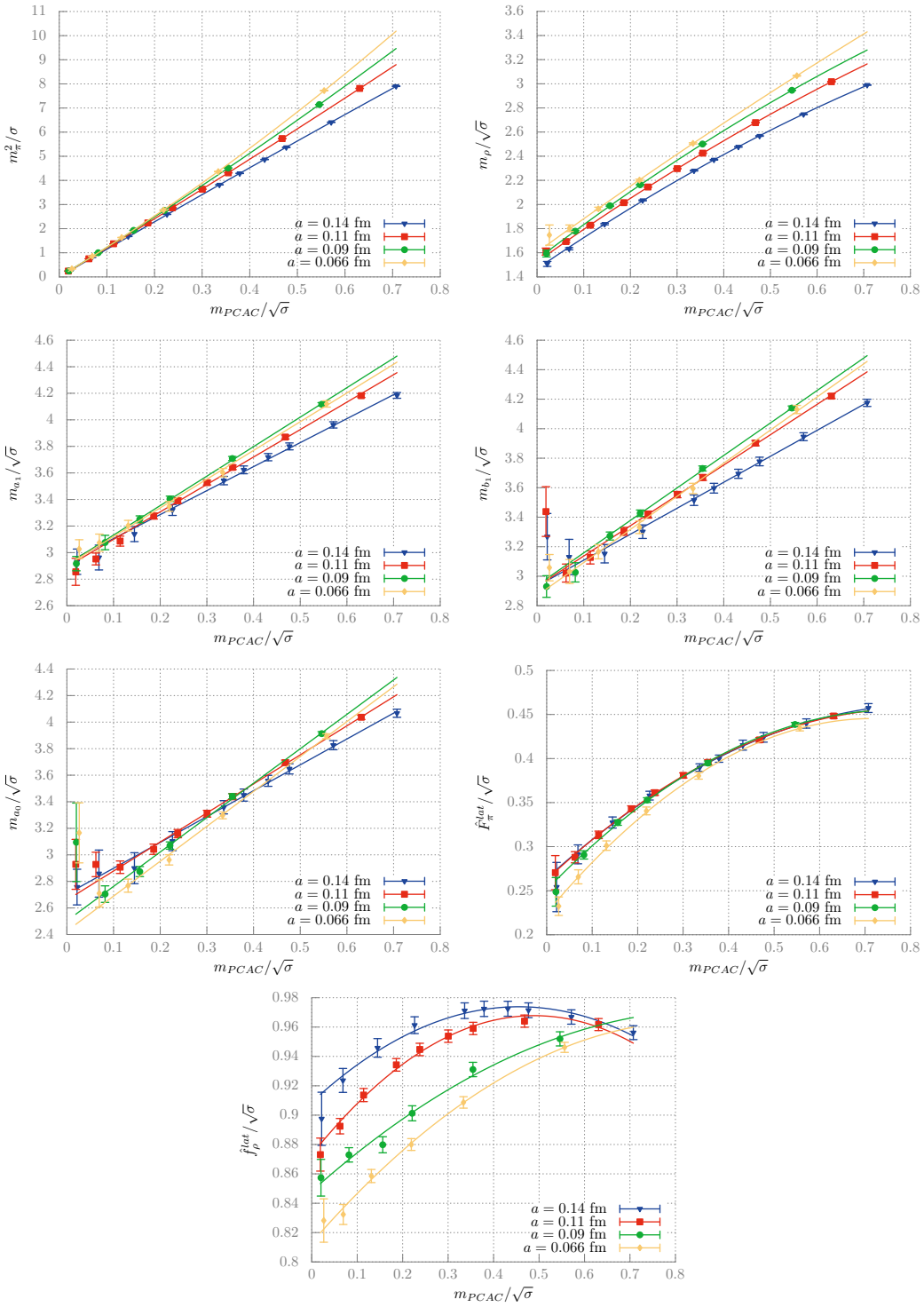

Figure F.10.: Plot of the SU(7) masses and decay constants as a function of m_{PCAC} for different lattice spacings.

N	A	B	κ_c
2	0.6831(75)	0.972(74)	0.152880(22)(81)
3	0.7519(42)	0.739(38)	0.156670(8)(86)
4	0.7812(36)	0.607(32)	0.158218(7)(87)
5	0.8050(25)	0.483(21)	0.158596(5)(87)
6	0.8098(22)	0.462(18)	0.159103(4)(87)
7	0.8133(19)	0.447(16)	0.159326(4)(87)
17	0.8286(55)	0.370(42)	0.159590(12)(87)

Table F.1.: Fit parameters of the PCAC mass.

N	$\Delta\kappa_c/\Delta\beta$	$\Delta\beta/\Delta(a\sqrt{\sigma})$	$\delta(a\sqrt{\sigma})$	$\delta\kappa_c$
2	0.0588172	1.37097	0.001	0.0000806
3	0.033977	2.54391	0.001	0.0000864
4	0.019335	4.4773	0.001	0.0000866
6	0.00891258	9.78578	0.001	0.0000872

Table F.2.: Systematic errors of κ_c and its dependencies, according to eq. (4.12).

κ	$N_s^3 \times N_t$	$m_{\mathrm{PCAC}}/\sqrt{\sigma}$	$m_\pi/\sqrt{\sigma}$	$m_\rho/\sqrt{\sigma}$	$m_{a_1}/\sqrt{\sigma}$	$m_{b_1}/\sqrt{\sigma}$	$m_{a_0}/\sqrt{\sigma}$
0.14581	$16^3 \times 32$	0.5786(11)	2.7042(85)	2.931(13)	4.038(50)	4.043(49)	3.952(59)
	$24^3 \times 48$	0.57866(90)	2.6926(56)	2.9110(82)	4.136(64)	4.115(58)	4.110(52)
	$32^3 \times 64$	0.5776(12)	2.6835(58)	2.9122(93)	4.133(76)	4.125(70)	4.085(76)
0.14827	$16^3 \times 32$	0.3551(12)	2.131(10)	2.464(18)	3.622(72)	3.602(69)	3.565(75)
	$24^3 \times 48$	0.35564(84)	2.1116(61)	2.438(10)	3.730(79)	3.743(75)	3.745(72)
	$32^3 \times 64$	0.3548(11)	2.0968(59)	2.431(11)	3.707(92)	3.679(78)	3.71(11)
0.15008	$16^3 \times 32$	0.2054(14)	1.664(12)	2.134(24)	3.33(11)	3.29(10)	3.49(11)
	$24^3 \times 48$	0.20732(83)	1.6322(72)	2.104(16)	3.43(11)	3.529(92)	3.65(12)
	$32^3 \times 64$	0.2065(10)	1.6138(63)	2.086(18)	3.40(11)	3.353(94)	3.57(20)
0.15096	$16^3 \times 32$	0.1363(17)	1.400(15)	1.977(29)	3.18(16)	3.14(15)	3.97(22)
	$24^3 \times 48$	0.14047(88)	1.3617(89)	1.947(23)	3.27(13)	3.50(12)	3.96(15)
	$32^3 \times 64$	0.13964(99)	1.3444(68)	1.933(26)	3.25(14)	3.22(12)	3.68(39)
0.151959	$24^3 \times 48$	0.0661(15)	0.960(15)	1.818(32)	3.24(14)	3.75(20)	1.97(36)
	$32^3 \times 64$	0.0660(11)	0.9558(100)	1.813(40)	3.17(16)	3.38(20)	3.67(16)
0.152496	$24^3 \times 48$	0.0236(23)	0.639(39)	1.812(71)	3.29(39)	5.1(1.3)	
	$32^3 \times 64$	0.0186(18)	0.538(30)	1.730(60)	3.18(15)	3.64(26)	2.88(32)

Table F.3.: Ground state meson masses of $\mathrm{SU}(2)$ gauge theory.

κ	$N_s^3 \times N_t$	$m_{\text{PCAC}}/\sqrt{\sigma}$	$m_\pi/\sqrt{\sigma}$	$m_\rho/\sqrt{\sigma}$	$m_{a_1}/\sqrt{\sigma}$	$m_{b_1}/\sqrt{\sigma}$	$m_{a_0}/\sqrt{\sigma}$
0.15002	$16^3 \times 32$	0.5514(11)	2.6597(73)	2.915(11)	4.081(35)	4.090(33)	3.938(37)
	$24^3 \times 48$	0.55154(55)	2.6528(31)	2.9066(47)	4.068(36)	4.071(44)	3.930(27)
	$32^3 \times 64$	0.55138(58)	2.6513(33)	2.9033(58)	4.117(57)	4.129(54)	3.982(43)
0.1522	$16^3 \times 32$	0.3555(11)	2.1186(86)	2.476(13)	3.678(42)	3.684(42)	3.512(50)
	$24^3 \times 48$	0.35558(52)	2.1109(32)	2.4642(57)	3.684(43)	3.674(42)	3.518(37)
	$32^3 \times 64$	0.35558(51)	2.1111(32)	2.4631(70)	3.739(68)	3.769(65)	3.577(67)
0.1538	$16^3 \times 32$	0.2209(12)	1.669(10)	2.156(16)	3.390(55)	3.415(56)	3.266(83)
	$24^3 \times 48$	0.22105(49)	1.6606(36)	2.1362(76)	3.400(55)	3.386(53)	3.248(59)
	$32^3 \times 64$	0.22132(47)	1.6626(34)	2.1399(92)	3.464(86)	3.529(83)	3.299(91)
0.15458	$16^3 \times 32$	0.1582(13)	1.418(12)	2.006(20)	3.260(68)	3.323(73)	3.25(12)
	$24^3 \times 48$	0.15864(48)	1.4099(40)	1.9781(98)	3.259(64)	3.242(64)	3.169(90)
	$32^3 \times 64$	0.15907(44)	1.4130(35)	1.979(13)	3.32(10)	3.422(98)	3.163(98)
0.155638	$24^3 \times 48$	0.07741(50)	0.9993(56)	1.788(19)	3.134(62)	3.148(80)	3.51(21)
	$32^3 \times 64$	0.07818(42)	1.0030(39)	1.796(24)	3.064(87)	3.26(10)	3.20(26)
0.15613	$24^3 \times 48$	0.03958(69)	0.7306(86)	1.710(25)	3.032(93)	3.15(18)	2.51(23)
	$32^3 \times 64$	0.04128(43)	0.7411(54)	1.749(26)	2.88(11)	3.23(17)	3.07(61)

Table F.4.: $\mathrm{SU}(3)$ ground state meson masses.

κ	$N_s^3 \times N_t$	$m_{\text{PCAC}}/\sqrt{\sigma}$	$m_\pi/\sqrt{\sigma}$	$m_\rho/\sqrt{\sigma}$	$m_{a_1}/\sqrt{\sigma}$	$m_{b_1}/\sqrt{\sigma}$	$m_{a_0}/\sqrt{\sigma}$
0.15184	$16^3 \times 32$	0.52889(72)	2.6147(71)	2.882(11)	3.999(41)	4.050(44)	3.855(39)
	$24^3 \times 48$	0.52863(38)	2.6168(24)	2.8921(38)	4.070(28)	4.104(24)	3.914(22)
0.154	$16^3 \times 32$	0.33716(70)	2.0641(83)	2.437(16)	3.575(56)	3.639(60)	3.406(56)
	$24^3 \times 48$	0.33710(36)	2.0665(24)	2.4513(46)	3.656(29)	3.691(30)	3.482(29)
0.15559	$16^3 \times 32$	0.20413(73)	1.5965(97)	2.106(25)	3.235(80)	3.331(91)	3.137(65)
	$24^3 \times 48$	0.20423(35)	1.5993(25)	2.1227(64)	3.343(37)	3.363(40)	3.184(47)
0.15635	$16^3 \times 32$	0.14303(77)	1.337(11)	1.954(31)	3.04(10)	3.19(13)	3.03(11)
	$24^3 \times 48$	0.14332(35)	1.3390(26)	1.9651(85)	3.198(46)	3.198(49)	3.095(73)
0.157173	$24^3 \times 48$	0.07935(36)	1.0001(32)	1.802(13)	3.088(80)	3.009(87)	3.26(12)
0.15764	$24^3 \times 48$	0.04350(39)	0.7498(40)	1.709(20)	3.03(12)	3.00(16)	3.34(26)

Table F.5.: $\mathrm{SU}(4)$ ground state meson masses.

κ	$N_s^3 \times N_t$	$m_{\text{PCAC}}/\sqrt{\sigma}$	$m_\pi/\sqrt{\sigma}$	$m_\rho/\sqrt{\sigma}$	$m_{a_1}/\sqrt{\sigma}$	$m_{b_1}/\sqrt{\sigma}$	$m_{a_0}/\sqrt{\sigma}$
0.15205	$16^3 \times 32$	0.55192(54)	2.6736(37)	2.9321(55)	4.070(28)	4.114(31)	3.872(30)
	$24^3 \times 48$	0.55112(33)	2.6680(18)	2.9331(28)	4.080(20)	4.127(23)	3.904(20)
0.15426	$16^3 \times 32$	0.35403(54)	2.1156(43)	2.4774(72)	3.671(36)	3.711(43)	3.420(47)
	$24^3 \times 48$	0.35314(31)	2.1065(20)	2.4769(36)	3.658(25)	3.708(25)	3.446(27)
0.15592	$16^3 \times 32$	0.21349(56)	1.6322(54)	2.1292(100)	3.374(54)	3.402(67)	3.095(61)
	$24^3 \times 48$	0.21247(29)	1.6192(22)	2.1263(54)	3.350(33)	3.411(32)	3.115(46)
0.15658	$16^3 \times 32$	0.15960(58)	1.4102(61)	1.989(12)	3.257(69)	3.276(90)	3.021(98)
	$24^3 \times 48$	0.15852(29)	1.3954(24)	1.9851(69)	3.238(43)	3.304(37)	3.006(66)
0.157548	$24^3 \times 48$	0.08158(29)	1.0017(29)	1.779(13)	3.113(60)	3.201(72)	2.96(12)
0.158355	$24^3 \times 48$	0.01833(38)	0.4869(68)	1.655(32)	3.076(64)	3.49(14)	2.80(35)

Table F.6.: $\mathrm{SU}(5)$ ground state meson masses.

κ	$N_s^3 \times N_t$	$m_{\text{PCAC}}/\sqrt{\sigma}$	$m_\pi/\sqrt{\sigma}$	$m_\rho/\sqrt{\sigma}$	$m_{a_1}/\sqrt{\sigma}$	$m_{b_1}/\sqrt{\sigma}$	$m_{a_0}/\sqrt{\sigma}$
0.15264	$16^3 \times 32$	0.54200(48)	2.6579(35)	2.9299(51)	4.064(29)	4.091(27)	3.910(29)
	$24^3 \times 48$	0.54185(26)	2.6574(16)	2.9279(25)	4.069(44)	4.104(17)	3.863(17)
0.15479	$16^3 \times 32$	0.35056(49)	2.1079(42)	2.4868(67)	3.630(40)	3.664(38)	3.456(42)
	$24^3 \times 48$	0.35042(24)	2.1086(17)	2.4832(30)	3.654(21)	3.694(20)	3.388(22)
0.15636	$16^3 \times 32$	0.21769(51)	1.6436(50)	2.1549(90)	3.355(39)	3.392(35)	3.127(72)
	$24^3 \times 48$	0.21774(23)	1.6464(18)	2.1504(42)	3.338(24)	3.387(24)	3.018(31)
0.15712	$16^3 \times 32$	0.15545(53)	1.3820(57)	1.990(12)	3.206(51)	3.232(47)	3.00(11)
	$24^3 \times 48$	0.15570(22)	1.3867(20)	1.9864(54)	3.180(27)	3.235(29)	2.834(42)
0.158051	$24^3 \times 48$	0.08177(22)	1.0013(25)	1.7819(100)	2.944(60)	3.001(76)	2.687(65)
0.158845	$24^3 \times 48$	0.01948(50)	0.4989(55)	1.569(36)	2.871(65)	3.46(16)	2.39(25)

Table F.7.: $\mathrm{SU}(6)$ ground state meson masses.

κ	$N_s^3 \times N_t$	$m_{\text{PCAC}}/\sqrt{\sigma}$	$m_\pi/\sqrt{\sigma}$	$m_\rho/\sqrt{\sigma}$	$m_{a_1}/\sqrt{\sigma}$	$m_{b_1}/\sqrt{\sigma}$	$m_{a_0}/\sqrt{\sigma}$
0.152816	$16^3 \times 32$	0.54657(39)	2.6767(31)	2.9489(47)	4.105(26)	4.117(27)	3.913(36)
	$24^3 \times 48$	0.54604(22)	2.6727(13)	2.9461(20)	4.117(13)	4.140(14)	3.913(15)
0.154967	$16^3 \times 32$	0.35511(39)	2.1322(34)	2.5100(55)	3.689(32)	3.712(33)	3.464(25)
	$24^3 \times 48$	0.35455(21)	2.1242(14)	2.5009(25)	3.709(16)	3.730(17)	3.441(19)
0.156547	$16^3 \times 32$	0.22147(41)	1.6689(40)	2.1781(75)	3.356(46)	3.412(51)	3.147(30)
	$24^3 \times 48$	0.22093(20)	1.6599(16)	2.1631(36)	3.405(20)	3.427(22)	3.070(28)
0.157339	$16^3 \times 32$	0.15669(42)	1.3983(45)	2.0096(98)	3.171(61)	3.262(72)	3.013(47)
	$24^3 \times 48$	0.15619(20)	1.3892(17)	1.9895(48)	3.251(26)	3.272(27)	2.874(38)
0.158273	$24^3 \times 48$	0.08183(20)	1.0007(19)	1.7785(81)	3.076(54)	3.026(65)	2.704(62)
0.159062	$24^3 \times 48$	0.02034(24)	0.4960(40)	1.594(28)	2.917(54)	2.930(73)	3.09(30)

Table F.8.: $\mathrm{SU}(7)$ ground state meson masses.

κ	$N_s^3 \times N_t$	$m_{\mathrm{PCAC}}/\sqrt{\sigma}$	$m_\pi/\sqrt{\sigma}$	$m_\rho/\sqrt{\sigma}$	$m_{a_1}/\sqrt{\sigma}$	$m_{b_1}/\sqrt{\sigma}$	$m_{a_0}/\sqrt{\sigma}$
0.15298	$12^3 \times 24$	0.55913(42)	2.7030(56)	2.9633(77)	4.122(23)	4.170(24)	3.917(24)
0.15521	$12^3 \times 24$	0.35983(44)	2.1356(69)	2.499(10)	3.681(33)	3.733(34)	3.423(37)
0.15684	$12^3 \times 24$	0.22114(46)	1.6545(86)	2.148(14)	3.344(46)	3.410(50)	3.016(60)
0.15755	$12^3 \times 24$	0.16257(47)	1.4104(99)	1.992(17)	3.191(54)	3.277(63)	2.812(84)
0.158531	$12^3 \times 24$	0.08390(68)	0.998(12)	1.776(22)	3.019(70)	3.161(97)	2.59(16)
0.15931	$12^3 \times 24$	0.0212(11)	0.474(38)	1.580(66)	3.23(34)	3.20(29)	3.3(11)

Table F.9.: $\mathrm{SU}(17)$ ground state meson masses.

κ	$N_s^3 \times N_t$	$m_{\pi^\star}/\sqrt{\sigma}$	$m_{\rho^\star}/\sqrt{\sigma}$	$m_{a_1^\star}/\sqrt{\sigma}$	$m_{b_1^\star}/\sqrt{\sigma}$	$m_{a_0^\star}/\sqrt{\sigma}$
0.14581	$16^3 \times 32$	4.56(11)	4.67(13)	5.56(12)	5.61(11)	5.51(13)
	$24^3 \times 48$	4.74(15)	4.586(77)	5.59(19)	5.73(20)	5.36(12)
	$32^3 \times 64$	4.69(13)	4.86(14)	5.62(12)	5.84(14)	5.34(14)
0.14827	$16^3 \times 32$	4.16(15)	4.35(16)	5.24(18)	5.32(14)	5.28(21)
	$24^3 \times 48$	4.27(19)	4.229(90)	5.11(32)	5.47(28)	4.87(18)
	$32^3 \times 64$	4.28(16)	4.52(17)	5.26(15)	5.61(18)	4.87(18)
0.15008	$16^3 \times 32$	3.85(20)	4.20(19)	4.96(27)	5.17(19)	4.92(36)
	$24^3 \times 48$	3.96(27)	4.02(10)	4.82(23)	5.26(30)	4.54(34)
	$32^3 \times 64$	3.95(19)	4.27(18)	5.06(21)	5.31(22)	4.59(25)
0.15096	$16^3 \times 32$	3.71(27)	4.16(21)	4.73(31)	5.08(24)	5.09(67)
	$24^3 \times 48$	3.86(30)	3.95(11)	4.68(29)	5.5(1.4)	4.87(64)
	$32^3 \times 64$	3.75(23)	4.14(20)	5.00(27)	5.50(34)	4.51(35)

Table F.10.: First excited state meson masses of $\mathrm{SU}(2)$ gauge theory.

κ	$N_s^3 \times N_t$	$m_{\pi^\star}/\sqrt{\sigma}$	$m_{\rho^\star}/\sqrt{\sigma}$	$m_{a_1^\star}/\sqrt{\sigma}$	$m_{b_1^\star}/\sqrt{\sigma}$	$m_{a_0^\star}/\sqrt{\sigma}$
0.15002	$16^3 \times 32$	4.599(78)	4.73(13)	5.666(80)	5.821(82)	5.535(95)
	$24^3 \times 48$	4.435(86)	4.549(95)	5.617(85)	5.639(97)	5.519(62)
	$32^3 \times 64$	4.417(82)	4.504(79)	5.39(11)	5.51(13)	5.134(96)
0.1522	$16^3 \times 32$	4.239(98)	4.39(16)	5.43(11)	5.66(11)	5.26(14)
	$24^3 \times 48$	4.05(11)	4.21(12)	5.42(12)	5.35(13)	5.270(92)
	$32^3 \times 64$	4.07(11)	4.195(100)	5.11(16)	5.21(16)	4.70(14)
0.1538	$16^3 \times 32$	3.99(13)	4.18(18)	5.33(16)	5.70(14)	5.12(24)
	$24^3 \times 48$	3.77(14)	3.99(14)	5.26(11)	5.20(19)	5.13(14)
	$32^3 \times 64$	3.81(17)	4.01(12)	4.96(16)	5.02(21)	4.34(20)
0.15458	$16^3 \times 32$	3.88(15)	4.11(20)	5.35(20)	5.82(15)	5.22(37)
	$24^3 \times 48$	3.65(18)	3.89(15)	5.23(15)	5.16(14)	5.09(20)
	$32^3 \times 64$	3.68(23)	3.95(14)	4.86(20)	4.96(26)	4.44(18)

Table F.11.: $\mathrm{SU}(3)$ first excited state meson masses.

κ	$N_s^3 \times N_t$	$m_{\pi^\star}/\sqrt{\sigma}$	$m_{\rho^\star}/\sqrt{\sigma}$	$m_{a_1^\star}/\sqrt{\sigma}$	$m_{b_1^\star}/\sqrt{\sigma}$	$m_{a_0^\star}/\sqrt{\sigma}$
0.15184	$16^3 \times 32$	4.84(11)	4.67(17)	5.65(17)	5.72(21)	5.51(17)
	$24^3 \times 48$	4.576(58)	4.705(65)	5.507(80)	5.531(82)	5.418(48)
0.154	$16^3 \times 32$	4.57(13)	4.39(21)	5.35(22)	5.45(27)	5.20(22)
	$24^3 \times 48$	4.263(74)	4.427(82)	5.19(11)	5.14(11)	5.082(66)
0.15559	$16^3 \times 32$	4.37(16)	4.23(26)	5.08(27)	5.16(31)	4.92(32)
	$24^3 \times 48$	4.07(12)	4.26(10)	4.96(16)	4.82(14)	4.851(94)
0.15635	$16^3 \times 32$	4.26(20)	4.17(30)	4.93(32)	5.00(36)	4.71(43)
	$24^3 \times 48$	4.02(26)	4.20(12)	4.85(20)	4.64(18)	4.75(12)

Table F.12.: $\mathrm{SU}(4)$ first excited state meson masses.

κ	$N_s^3 \times N_t$	$m_{\pi^\star}/\sqrt{\sigma}$	$m_{\rho^\star}/\sqrt{\sigma}$	$m_{a_1^\star}/\sqrt{\sigma}$	$m_{b_1^\star}/\sqrt{\sigma}$	$m_{a_0^\star}/\sqrt{\sigma}$
0.15205	$16^3 \times 32$	4.646(62)	4.795(71)	5.586(89)	5.671(88)	5.36(10)
	$24^3 \times 48$	4.505(47)	4.646(52)	5.471(58)	5.624(67)	5.344(37)
0.15426	$16^3 \times 32$	4.282(79)	4.484(88)	5.32(17)	5.38(13)	4.91(17)
	$24^3 \times 48$	4.146(63)	4.336(68)	5.155(77)	5.300(90)	4.981(48)
0.15592	$16^3 \times 32$	4.00(10)	4.28(10)	5.04(12)	5.18(12)	4.41(25)
	$24^3 \times 48$	3.882(90)	4.125(87)	4.96(11)	5.08(12)	4.754(66)
0.15658	$16^3 \times 32$	3.88(12)	4.20(11)	4.93(15)	5.09(15)	4.10(30)
	$24^3 \times 48$	3.79(13)	4.05(10)	4.89(13)	5.00(15)	4.696(82)

Table F.13.: $\mathrm{SU}(5)$ first excited state meson masses.

κ	$N_s^3 \times N_t$	$m_{\pi^\star}/\sqrt{\sigma}$	$m_{\rho^\star}/\sqrt{\sigma}$	$m_{a_1^\star}/\sqrt{\sigma}$	$m_{b_1^\star}/\sqrt{\sigma}$	$m_{a_0^\star}/\sqrt{\sigma}$
0.15264	$16^3 \times 32$	4.494(62)	4.644(72)	5.519(52)	5.674(58)	5.22(16)
	$24^3 \times 48$	4.503(40)	4.634(45)	5.557(48)	5.623(54)	5.396(31)
0.15479	$16^3 \times 32$	4.131(78)	4.329(91)	5.130(73)	5.291(80)	4.83(24)
	$24^3 \times 48$	4.136(53)	4.298(64)	5.231(68)	5.264(74)	5.028(44)
0.15636	$16^3 \times 32$	3.90(10)	4.14(12)	4.846(99)	5.00(11)	4.59(12)
	$24^3 \times 48$	3.874(70)	4.059(92)	4.987(98)	5.00(10)	4.759(65)
0.15712	$16^3 \times 32$	3.82(13)	4.08(14)	4.71(12)	4.85(13)	4.17(28)
	$24^3 \times 48$	3.739(75)	3.94(11)	4.85(13)	4.86(13)	4.633(85)

Table F.14.: $\mathrm{SU}(6)$ first excited state meson masses.

κ	$N_s^3 \times N_t$	$m_{\pi^\star}/\sqrt{\sigma}$	$m_{\rho^\star}/\sqrt{\sigma}$	$m_{a_1^\star}/\sqrt{\sigma}$	$m_{b_1^\star}/\sqrt{\sigma}$	$m_{a_0^\star}/\sqrt{\sigma}$
0.152816	$16^3 \times 32$	4.588(38)	4.743(40)	5.630(43)	5.701(52)	5.386(50)
	$24^3 \times 48$	4.520(36)	4.666(39)	5.585(46)	5.694(59)	5.435(27)
0.154967	$16^3 \times 32$	4.181(49)	4.356(53)	5.297(57)	5.431(57)	5.024(63)
	$24^3 \times 48$	4.118(44)	4.315(49)	5.221(69)	5.338(69)	5.075(36)
0.156547	$16^3 \times 32$	3.928(62)	4.143(64)	5.075(79)	5.190(81)	4.753(92)
	$24^3 \times 48$	3.803(55)	4.061(57)	4.947(83)	5.085(94)	4.839(54)
0.157339	$16^3 \times 32$	3.814(75)	4.054(72)	4.972(100)	5.07(10)	4.63(12)
	$24^3 \times 48$	3.630(67)	3.937(63)	4.82(10)	4.98(12)	4.761(89)

Table F.15.: $\mathrm{SU}(7)$ first excited state meson masses.

κ	$N_s^3 \times N_t$	$m_{\pi^\star}/\sqrt{\sigma}$	$m_{\rho^\star}/\sqrt{\sigma}$	$m_{a_1^\star}/\sqrt{\sigma}$	$m_{b_1^\star}/\sqrt{\sigma}$	$m_{a_0^\star}/\sqrt{\sigma}$
0.15298	$12^3 \times 24$	4.530(48)	4.660(59)	5.56(10)	5.625(85)	5.344(53)
0.15521	$12^3 \times 24$	4.137(62)	4.292(76)	5.199(64)	5.29(14)	4.949(81)
0.15684	$12^3 \times 24$	3.865(82)	4.033(88)	4.976(86)	5.07(20)	4.67(12)
0.15755	$12^3 \times 24$	3.76(10)	3.928(93)	4.90(10)	4.99(25)	4.57(18)

Table F.16.: $\mathrm{SU}(17)$ first excited state meson masses.

State X	$A_{X,1}$	$A_{X,2}$	$B_{X,1}$	$B_{X,2}$
a_0	2.402(34)	4.25(62)	2.721(53)	-6.84(96)
a_1	2.860(21)	0.84(36)	2.289(35)	-2.02(61)
b_1	2.901(23)	1.07(40)	2.273(38)	-2.83(72)
$\pi^\star$	3.392(57)	1.0(1.1)	2.044(80)	-1.2(1.6)
$\rho^\star$	3.696(54)	0.23(55)	1.782(67)	-1.30(54)
$a_0^\star$	4.356(65)	1.8(1.4)	1.902(98)	-2.9(2.1)
$a_1^\star$	4.587(75)	1.2(1.2)	1.76(12)	-2.1(19)
$b_1^\star$	4.609(99)	1.7(1.5)	1.87(15)	-2.5(2.2)

Table F.17.: Coefficients for the expansion of the particle masses as $m_X/\sqrt{\sigma} = \left(A_{X,1} + A_{X,2}/N^2\right) + \left(B_{X,1} + B_{X,2}/N^2\right) m_{\mathrm{PCAC}}/\sqrt{\sigma}$.

κ	$N_s^3 \times N_t$	$\hat{F}_\pi^{\mathrm{lat}}/\sqrt{\sigma}$	$\hat{F}_\pi/\sqrt{\sigma}$	$\hat{f}_\rho^{\mathrm{lat}}/\sqrt{\sigma}$	$\hat{f}_\rho/\sqrt{\sigma}$
0.14581	$24^3 \times 48$	0.4033(62)	0.3273(50)	0.900(14)	0.6469(99)
0.14827	$24^3 \times 48$	0.3598(65)	0.2921(53)	0.883(15)	0.635(10)
0.15008	$24^3 \times 48$	0.3159(79)	0.2564(64)	0.861(17)	0.619(12)
0.15096	$24^3 \times 48$	0.291(10)	0.2360(81)	0.844(21)	0.607(15)
0.151959	$24^3 \times 48$	0.275(20)	0.223(16)	0.845(36)	0.608(26)
0.152496	$24^3 \times 48$	0.24(16)	0.20(13)	0.74(11)	0.529(79)

Table F.18.: Decay constants for the $\mathrm{SU}(2)$ theory.

κ	$N_s^3 \times N_t$	$\hat{F}_\pi^{\mathrm{lat}}/\sqrt{\sigma}$	$\hat{F}_\pi/\sqrt{\sigma}$	$\hat{f}_\rho^{\mathrm{lat}}/\sqrt{\sigma}$	$\hat{f}_\rho/\sqrt{\sigma}$
0.15002	$24^3 \times 48$	0.4132(58)	0.3231(46)	0.9402(83)	0.6405(56)
0.1522	$24^3 \times 48$	0.3727(51)	0.2914(40)	0.9143(85)	0.6229(58)
0.1538	$24^3 \times 48$	0.3325(64)	0.2600(50)	0.8835(91)	0.6019(62)
0.15458	$24^3 \times 48$	0.3083(78)	0.2411(61)	0.865(10)	0.5894(68)
0.155638	$24^3 \times 48$	0.2742(78)	0.2144(61)	0.849(18)	0.578(12)
0.15613	$24^3 \times 48$	0.246(14)	0.192(11)	0.893(55)	0.609(38)

Table F.19.: Decay constants for the $\mathrm{SU}(3)$ theory.

κ	$N_s^3 \times N_t$	$\hat{F}_\pi^{\mathrm{lat}}/\sqrt{\sigma}$	$\hat{F}_\pi/\sqrt{\sigma}$	$\hat{f}_\rho^{\mathrm{lat}}/\sqrt{\sigma}$	$\hat{f}_\rho/\sqrt{\sigma}$
0.15184	$24^3 \times 48$	0.4305(37)	0.3318(29)	0.9807(64)	0.6531(43)
0.154	$24^3 \times 48$	0.3857(39)	0.2973(30)	0.9526(67)	0.6344(45)
0.15559	$24^3 \times 48$	0.3417(46)	0.2633(36)	0.9206(77)	0.6131(52)
0.15635	$24^3 \times 48$	0.3227(34)	0.2487(26)	0.8998(92)	0.5992(62)
0.157173	$24^3 \times 48$	0.2934(49)	0.2261(38)	0.870(14)	0.5795(94)
0.15764	$24^3 \times 48$	0.2710(71)	0.2089(54)	0.855(25)	0.569(17)

Table F.20.: Decay constants for the $\mathrm{SU}(4)$ theory.

κ	$N_s^3 \times N_t$	$\hat{F}_\pi^{\mathrm{lat}}/\sqrt{\sigma}$	$\hat{F}_\pi/\sqrt{\sigma}$	$\hat{f}_\rho^{\mathrm{lat}}/\sqrt{\sigma}$	$\hat{f}_\rho/\sqrt{\sigma}$
0.15205	$24^3 \times 48$	0.4350(31)	0.3333(24)	0.9748(36)	0.6444(24)
0.15426	$24^3 \times 48$	0.3909(32)	0.2994(24)	0.9521(36)	0.6294(24)
0.15592	$24^3 \times 48$	0.3484(37)	0.2669(28)	0.9222(38)	0.6096(25)
0.15658	$24^3 \times 48$	0.3291(42)	0.2521(32)	0.9069(40)	0.5995(26)
0.157548	$24^3 \times 48$	0.2951(39)	0.2260(30)	0.8821(48)	0.5832(32)
0.158355	$24^3 \times 48$	0.269(14)	0.206(10)	0.854(18)	0.565(12)

Table F.21.: Decay constants for the $\mathrm{SU}(5)$ theory.

κ	$N_s^3 \times N_t$	$\hat{F}_\pi^{\mathrm{lat}}/\sqrt{\sigma}$	$\hat{F}_\pi/\sqrt{\sigma}$	$\hat{f}_\rho^{\mathrm{lat}}/\sqrt{\sigma}$	$\hat{f}_\rho/\sqrt{\sigma}$
0.15264	$24^3 \times 48$	0.4374(25)	0.3342(19)	0.9914(34)	0.6514(22)
0.15479	$24^3 \times 48$	0.3944(26)	0.3013(20)	0.9623(34)	0.6323(23)
0.15636	$24^3 \times 48$	0.3536(30)	0.2702(23)	0.9284(36)	0.6101(24)
0.15712	$24^3 \times 48$	0.3302(35)	0.2523(27)	0.9080(40)	0.5967(26)
0.158051	$24^3 \times 48$	0.2987(34)	0.2282(26)	0.8829(54)	0.5802(36)
0.158845	$24^3 \times 48$	0.2676(91)	0.2044(69)	0.867(17)	0.570(11)

Table F.22.: Decay constants for the $\mathrm{SU}(6)$ theory.

κ	$N_s^3 \times N_t$	$\hat{F}_\pi^{\mathrm{lat}}/\sqrt{\sigma}$	$\hat{F}_\pi/\sqrt{\sigma}$	$\hat{f}_\rho^{\mathrm{lat}}/\sqrt{\sigma}$	$\hat{f}_\rho/\sqrt{\sigma}$
0.152816	$24^3 \times 48$	0.4386(23)	0.3345(18)	0.9520(48)	0.6235(31)
0.154967	$24^3 \times 48$	0.3949(24)	0.3011(18)	0.9311(49)	0.6098(32)
0.156547	$24^3 \times 48$	0.3529(27)	0.2691(20)	0.9013(51)	0.5902(34)
0.157339	$24^3 \times 48$	0.3273(31)	0.2496(24)	0.8798(55)	0.5762(36)
0.158273	$24^3 \times 48$	0.2906(47)	0.2216(36)	0.8729(49)	0.5717(32)
0.159062	$24^3 \times 48$	0.249(16)	0.190(12)	0.857(12)	0.5615(82)

Table F.23.: Decay constants for the $\mathrm{SU}(7)$ gauge theory.

κ	$N_s^3 \times N_t$	$\hat{F}_\pi^{\mathrm{lat}}/\sqrt{\sigma}$	$\hat{F}_\pi/\sqrt{\sigma}$	$\hat{f}_\rho^{\mathrm{lat}}/\sqrt{\sigma}$	$\hat{f}_\rho/\sqrt{\sigma}$
0.15298	$12^3 \times 24$	0.4456(31)	0.3381(23)	1.0055(92)	0.6539(60)
0.15521	$12^3 \times 24$	0.4045(35)	0.3069(27)	0.986(10)	0.6415(66)
0.15684	$12^3 \times 24$	0.3610(44)	0.2739(34)	0.958(11)	0.6227(74)
0.15755	$12^3 \times 24$	0.3379(53)	0.2564(40)	0.939(13)	0.6108(82)
0.158531	$12^3 \times 24$	0.307(12)	0.2326(93)	0.902(17)	0.587(11)
0.15931	$12^3 \times 24$	0.296(28)	0.225(21)	0.851(48)	0.553(31)

Table F.24.: Decay constants for the $\mathrm{SU}(17)$ theory.

β and $N_s^3 \times N_t$	κ	$m_{\mathrm{PCAC}}/\sqrt{\sigma}$	$m_\pi/\sqrt{\sigma}$	$m_\rho/\sqrt{\sigma}$	$m_{a_1}/\sqrt{\sigma}$	$m_{b_1}/\sqrt{\sigma}$	$m_{a_0}/\sqrt{\sigma}$
10.6573	0.153189	0.60704(68)	2.6059(35)	2.8038(48)	4.059(46)	4.159(45)	4.160(50)
$16^3 \times 32$	0.157084	0.37899(62)	2.0754(36)	2.3637(57)	3.650(60)	3.806(58)	3.773(62)
	0.160228	0.21749(60)	1.5907(38)	2.0085(77)	3.319(94)	3.541(78)	3.447(91)
	0.161603	0.15335(59)	1.3465(41)	1.8549(99)	3.19(14)	3.44(10)	3.33(12)
	0.163073	0.08915(60)	1.0397(49)	1.689(16)	2.87(31)	3.288(85)	3.28(18)
	0.164082	0.04711(65)	0.7673(73)	1.562(36)	3.32(25)	3.18(13)	3.29(20)
10.8485	0.15183	0.61261(49)	2.7441(28)	2.9675(40)	4.032(35)	4.180(36)	4.213(39)
$20^3 \times 40$	0.15548	0.34376(44)	2.0442(28)	2.3947(47)	3.474(42)	3.689(48)	3.698(52)
	0.15745	0.21204(42)	1.6062(30)	2.0812(67)	3.189(68)	3.424(58)	3.417(67)
	0.15844	0.14958(42)	1.3524(32)	1.9217(96)	3.12(10)	3.302(66)	3.337(81)
	0.15955	0.08261(43)	1.0119(40)	1.732(18)	3.01(13)	3.19(11)	3.24(15)
	0.16032	0.03681(55)	0.6836(72)	1.543(41)	3.18(24)	3.125(81)	3.38(13)
11.4462	0.14997	0.48690(30)	2.5682(25)	2.8820(44)	3.786(27)	3.963(25)	3.994(29)
$32^3 \times 64$	0.15135	0.30713(27)	1.9976(26)	2.4281(57)	3.368(35)	3.550(30)	3.573(34)
	0.1521	0.21200(26)	1.6437(27)	2.1774(75)	3.176(46)	3.355(31)	3.385(36)
	0.15254	0.15714(26)	1.4095(30)	2.0380(95)	3.105(54)	3.249(31)	3.298(37)
	0.15307	0.09208(26)	1.0784(36)	1.863(15)	2.961(85)	3.116(38)	3.230(44)
	0.15344	0.04707(30)	0.7807(54)	1.719(25)	2.95(11)	3.013(56)	3.356(94)

Table F.25.: Ground states masses for different β-values for the $\mathrm{SU}(4)$ theory.

β and $N_s^3 \times N_t$	κ	$m_{\mathrm{PCAC}}/\sqrt{\sigma}$	$m_\pi/\sqrt{\sigma}$	$m_\rho/\sqrt{\sigma}$	$m_{a_1}/\sqrt{\sigma}$	$m_{b_1}/\sqrt{\sigma}$	$m_{a_0}/\sqrt{\sigma}$
16.96	0.154	0.57856(51)	2.5380(24)	2.7432(37)	3.876(34)	3.963(33)	3.997(38)
$16^3 \times 32$	0.1574	0.37978(47)	2.0659(24)	2.3549(44)	3.477(40)	3.608(42)	3.639(44)
	0.1602	0.23292(46)	1.6291(27)	2.0328(58)	3.147(51)	3.317(58)	3.372(57)
	0.16173	0.15911(46)	1.3547(30)	1.8576(76)	3.036(76)	3.167(63)	3.246(74)
	0.16334	0.08646(47)	1.0081(38)	1.679(12)	2.75(16)	3.083(64)	3.157(70)
	0.1648	0.02285(83)	0.536(13)	1.451(49)	2.40(35)	2.97(14)	2.81(47)
17.244	0.1533	0.54200(36)	2.5723(20)	2.8198(31)	3.889(29)	4.051(30)	4.075(33)
$20^3 \times 40$	0.15572	0.36511(34)	2.0994(20)	2.4361(38)	3.502(39)	3.711(37)	3.725(36)
	0.15785	0.22040(33)	1.6255(22)	2.0914(51)	3.156(59)	3.403(46)	3.431(49)
	0.15864	0.16937(33)	1.4247(24)	1.9622(63)	3.027(67)	3.279(51)	3.316(44)
	0.16	0.08504(34)	1.0142(29)	1.750(12)	2.870(63)	3.054(50)	3.138(62)
	0.1611	0.01828(52)	0.4884(80)	1.623(33)	3.00(22)	2.72(13)	3.03(55)
18.155	0.15061	0.48355(44)	2.5860(45)	2.9087(64)	3.982(30)	4.058(34)	4.230(42)
$32^3 \times 64$	0.15188	0.31879(47)	2.0688(56)	2.4943(78)	3.707(48)	3.688(41)	4.009(52)
	0.15289	0.19111(50)	1.6026(77)	2.1626(99)	3.346(47)	3.398(54)	3.59(10)
	0.1533	0.13998(49)	1.3901(94)	2.032(11)	3.296(61)	3.284(64)	3.46(11)
	0.154	0.04993(40)	0.966(14)	1.807(18)	3.12(10)	3.100(92)	3.21(19)
	0.1542	0.01520(66)	0.699(15)	1.616(31)	2.81(31)	3.086(91)	3.15(22)

Table F.26.: Ground states masses for different β-values for the $\mathrm{SU}(5)$ theory.

β and $N_s^3 \times N_t$	κ	$m_{\text{PCAC}}/\sqrt{\sigma}$	$m_\pi/\sqrt{\sigma}$	$m_\rho/\sqrt{\sigma}$	$m_{a_1}/\sqrt{\sigma}$	$m_{b_1}/\sqrt{\sigma}$	$m_{a_0}/\sqrt{\sigma}$
33.7312	0.152816	0.70737(42)	2.8113(19)	2.9896(26)	4.067(30)	4.184(22)	4.175(24)
$16^3 \times 32$	0.154967	0.57104(39)	2.5315(19)	2.7468(27)	3.826(34)	3.962(24)	3.946(27)
	0.156547	0.47676(37)	2.3172(19)	2.5674(28)	3.648(38)	3.800(26)	3.778(29)
	0.157339	0.43131(36)	2.2061(19)	2.4771(29)	3.558(41)	3.719(27)	3.694(31)
	0.158273	0.37903(32)	2.0714(19)	2.3703(30)	3.450(46)	3.623(29)	3.597(33)
	0.159062	0.33632(31)	1.9537(20)	2.2799(32)	3.359(50)	3.543(32)	3.515(36)
	0.1612	0.22631(30)	1.6100(21)	2.0339(41)	3.103(72)	3.321(41)	3.302(46)
	0.1629	0.14481(29)	1.2949(24)	1.8373(60)	2.90(12)	3.140(57)	3.152(62)
	0.1646	0.06871(30)	0.8998(32)	1.6331(90)	2.86(18)	2.963(94)	3.13(12)
	0.1657	0.02181(35)	0.5175(55)	1.507(21)	2.76(13)	2.931(95)	3.27(16)
34.2937	0.152816	0.63084(25)	2.7951(14)	3.0170(25)	4.036(17)	4.182(14)	4.221(17)
$20^3 \times 40$	0.154967	0.46808(24)	2.3944(14)	2.6780(28)	3.695(19)	3.870(15)	3.902(18)
	0.156547	0.35503(23)	2.0770(14)	2.4251(32)	3.439(23)	3.642(17)	3.669(20)
	0.157339	0.30038(22)	1.9069(15)	2.2970(34)	3.310(26)	3.527(18)	3.553(21)
	0.158273	0.23764(22)	1.6928(15)	2.1448(38)	3.160(31)	3.391(20)	3.418(24)
	0.159062	0.18609(22)	1.4961(16)	2.0153(44)	3.042(39)	3.275(22)	3.304(27)
	0.1602	0.11411(22)	1.1714(20)	1.8279(59)	2.907(47)	3.086(38)	3.127(44)
	0.16105	0.06218(23)	0.8671(24)	1.6929(93)	2.928(92)	2.952(45)	3.021(61)
	0.16175	0.01903(36)	0.4916(71)	1.610(29)	2.93(19)	2.86(10)	3.44(17)
36.08775	0.1505	0.55621(25)	2.7789(23)	3.0637(34)	3.894(19)	4.107(17)	4.138(20)
$24^3 \times 48$	0.1522	0.33382(24)	2.0894(25)	2.5028(44)	3.297(26)	3.582(22)	3.606(24)
	0.1531	0.21907(25)	1.6650(29)	2.1981(58)	2.962(39)	3.307(28)	3.327(31)
	0.1538	0.13117(26)	1.2777(34)	1.9653(96)	2.768(49)	3.154(32)	3.162(34)
	0.1543	0.06934(26)	0.9251(45)	1.797(18)	2.71(10)	3.013(52)	3.032(59)
	0.15465	0.02647(30)	0.5792(81)	1.705(56)	3.17(23)	2.997(53)	3.108(69)

Table F.27.: Ground states masses for different β-values for the $\mathrm{SU}(7)$ theory.

β and $N_s^3 \times N_t$	κ	$\hat{F}_\pi^{\mathrm{lat}}/\sqrt{\sigma}$	$\hat{F}_\pi/\sqrt{\sigma}$	$\hat{f}_\rho^{\mathrm{lat}}/\sqrt{\sigma}$	$\hat{f}_\rho/\sqrt{\sigma}$
10.6573	0.153189	0.4411(74)	0.3334(56)	0.9856(89)	0.5992(54)
$16^3 \times 32$	0.157084	0.4012(81)	0.3032(61)	0.9836(93)	0.5980(56)
	0.160228	0.3562(97)	0.2692(74)	0.964(10)	0.5861(62)
	0.161603	0.331(12)	0.2505(87)	0.949(11)	0.5770(69)
	0.163073	0.297(17)	0.224(13)	0.925(14)	0.5625(87)
	0.164082	0.276(28)	0.209(21)	0.882(21)	0.536(13)
10.8485	0.15183	0.4326(43)	0.3290(33)	0.9664(66)	0.6245(43)
$20^3 \times 40$	0.15548	0.3821(45)	0.2905(34)	0.9477(69)	0.6124(45)
	0.15745	0.3433(52)	0.2610(39)	0.9221(74)	0.5959(48)
	0.15844	0.3198(60)	0.2432(46)	0.9020(81)	0.5829(53)
	0.15955	0.2879(89)	0.2189(68)	0.870(11)	0.5623(70)
	0.16032	0.267(18)	0.203(14)	0.836(19)	0.540(12)
11.4462	0.14997	0.4118(37)	0.3231(29)	0.9146(57)	0.6426(40)
$32^3 \times 64$	0.15135	0.3663(35)	0.2874(28)	0.8817(56)	0.6195(39)
	0.1521	0.3345(36)	0.2625(28)	0.8563(56)	0.6017(40)
	0.15254	0.3129(38)	0.2455(30)	0.8384(58)	0.5890(41)
	0.15307	0.2830(45)	0.2221(35)	0.8129(67)	0.5712(47)
	0.15344	0.2577(66)	0.2022(51)	0.7957(95)	0.5591(67)

Table F.28.: Decay constants for different β-values for the $\mathrm{SU}(4)$ theory.

β and $N_s^3 \times N_t$	κ	$\hat{F}_\pi^{\mathrm{lat}}/\sqrt{\sigma}$	$\hat{F}_\pi/\sqrt{\sigma}$	$\hat{f}_\rho^{\mathrm{lat}}/\sqrt{\sigma}$	$\hat{f}_\rho/\sqrt{\sigma}$
16.96	0.154	0.4348(52)	0.3259(39)	0.9554(66)	0.5792(40)
$16^3 \times 32$	0.1574	0.4011(54)	0.3006(41)	0.9585(69)	0.5811(42)
	0.1602	0.3629(63)	0.2719(47)	0.9469(73)	0.5740(44)
	0.16173	0.3378(77)	0.2532(58)	0.9340(78)	0.5662(48)
	0.16334	0.311(12)	0.2329(91)	0.917(10)	0.5562(61)
	0.1648	0.295(24)	0.221(18)	0.902(11)	0.5467(68)
17.244	0.1533	0.4313(35)	0.3264(26)	0.9767(52)	0.6266(34)
$20^3 \times 40$	0.15572	0.3955(36)	0.2993(28)	0.9627(53)	0.6176(34)
	0.15785	0.3536(42)	0.2676(32)	0.9351(56)	0.5999(36)
	0.15864	0.3355(47)	0.2539(36)	0.9205(60)	0.5905(38)
	0.16	0.3014(71)	0.2281(53)	0.8929(76)	0.5728(49)
	0.1611	0.264(27)	0.200(20)	0.885(16)	0.568(10)
18.155	0.15061	0.4279(37)	0.3341(29)	0.9371(59)	0.6543(42)
$32^3 \times 64$	0.15188	0.3875(39)	0.3025(30)	0.9054(60)	0.6322(42)
	0.15289	0.3469(45)	0.2709(35)	0.8714(62)	0.6084(43)
	0.1533	0.3287(50)	0.2566(39)	0.8562(65)	0.5978(46)
	0.154	0.2929(79)	0.2287(62)	0.8405(97)	0.5869(68)
	0.1542	0.261(24)	0.204(19)	0.819(22)	0.572(15)

Table F.29.: Decay constants for different β-values for the $\mathrm{SU}(5)$ theory.

β and $N_s^3 \times N_t$	κ	$\hat{F}_\pi^{\mathrm{lat}}/\sqrt{\sigma}$	$\hat{F}_\pi/\sqrt{\sigma}$	$\hat{f}_\rho^{\mathrm{lat}}/\sqrt{\sigma}$	$\hat{f}_\rho/\sqrt{\sigma}$
33.7312	0.152816	0.4573(51)	0.3419(38)	0.9562(47)	0.5723(28)
$16^3 \times 32$	0.154967	0.4398(52)	0.3288(39)	0.9669(49)	0.5787(29)
	0.156547	0.4241(55)	0.3170(41)	0.9715(50)	0.5815(30)
	0.157339	0.4152(56)	0.3104(42)	0.9725(51)	0.5821(31)
	0.158273	0.3999(41)	0.2989(31)	0.9724(52)	0.5821(31)
	0.159062	0.3897(42)	0.2913(32)	0.9712(53)	0.5813(32)
	0.1612	0.3579(50)	0.2675(37)	0.9613(57)	0.5754(34)
	0.1629	0.3274(63)	0.2447(47)	0.9458(63)	0.5661(38)
	0.1646	0.291(11)	0.2177(80)	0.9237(82)	0.5529(49)
	0.1657	0.254(28)	0.190(21)	0.898(18)	0.537(11)
34.2937	0.152816	0.4483(26)	0.3371(20)	0.9617(41)	0.6106(26)
$20^3 \times 40$	0.154967	0.4212(27)	0.3168(20)	0.9641(42)	0.6121(26)
	0.156547	0.3957(28)	0.2976(21)	0.9591(42)	0.6089(27)
	0.157339	0.3808(29)	0.2864(22)	0.9538(42)	0.6056(27)
	0.158273	0.3613(31)	0.2717(23)	0.9448(42)	0.5998(27)
	0.159062	0.3430(34)	0.2579(25)	0.9343(43)	0.5932(27)
	0.1602	0.3134(42)	0.2357(32)	0.9137(45)	0.5801(28)
	0.16105	0.2880(63)	0.2165(48)	0.8925(52)	0.5666(33)
	0.16175	0.270(19)	0.203(14)	0.873(11)	0.5543(71)
36.08775	0.1505	0.4323(22)	0.3371(18)	0.9462(34)	0.6543(24)
$24^3 \times 48$	0.1522	0.3797(26)	0.2961(20)	0.9087(39)	0.6284(27)
	0.1531	0.3411(30)	0.2660(23)	0.8800(40)	0.6085(28)
	0.1538	0.3012(46)	0.2348(36)	0.8585(45)	0.5937(31)
	0.1543	0.2703(72)	0.2107(56)	0.8323(68)	0.5756(47)
	0.15465	0.242(16)	0.189(12)	0.828(15)	0.573(10)

Table F.30.: Decay constants for different β-values for the $\mathrm{SU}(7)$ theory.

Bibliography

[1] K. G. Wilson, Phys. Rev. D **10** (1974) 2445.

[2] G. 't Hooft, Nucl. Phys. B **72**, 461 (1974).

[3] J. M. Maldacena, Adv. Theor. Math. Phys. **2**, 231 (1998) [Int. J. Theor. Phys. **38**, 1113 (1999)] [arXiv:hep-th/9711200].

[4] S. S. Gubser, I. R. Klebanov and A. M. Polyakov, Phys. Lett. B **428**, 105 (1998) [arXiv:hep-th/9802109].

[5] E. Witten, Adv. Theor. Math. Phys. **2**, 253 (1998) [arXiv:hep-th/9802150].

[6] B. Lucini, M. Teper and U. Wenger, JHEP **0502** (2005) 033 [arXiv:hep-lat/0502003].

[7] C. Allton, M. Teper and A. Trivini, JHEP **0807** (2008) 021 [arXiv:0803.1092 [hep-lat]].

[8] B. Lucini, A. Rago and E. Rinaldi, Phys. Lett. B **712** (2012) 279 [arXiv:1202.6684 [hep-lat]].

[9] B. Lucini, M. Teper and U. Wenger, JHEP **0406** (2004) 012 [arXiv:hep-lat/0404008].

[10] B. Lucini, A. Rago and E. Rinaldi, JHEP **1008**, 119 (2010) [arXiv:1007.3879 [hep-lat]].

[11] M. Panero, Phys. Rev. Lett. **103** (2009) 232001 [arXiv:0907.3719 [hep-lat]];

[12] S. Datta and S. Gupta, Phys. Rev. D **82**, 114505 (2010) [arXiv:1006.0938 [hep-lat]].

[13] M. Caselle, L. Castagnini, A. Feo, F. Gliozzi and M. Panero, JHEP **1106**, 142 (2011) [arXiv:1105.0359 [hep-lat]].

[14] M. Caselle, L. Castagnini, A. Feo, F. Gliozzi, U. Gürsoy, M. Panero and A. Schäfer, JHEP **1205** (2012) 135 [arXiv:1111.0580 [hep-th]].

[15] B. Lucini and M. Panero, Phys. Rept. **526**, 93 (2013) [arXiv:1210.4997 [hep-th]].

[16] G. Bali and F. Bursa, PoS LAT **2007**, 050 (2007) [arXiv:0708.3427 [hep-lat]].

[17] G. S. Bali and F. Bursa, JHEP **0809**, 110 (2008) [arXiv:0806.2278 [hep-lat]].

[18] L. Del Debbio, B. Lucini, A. Patella and C. Pica, JHEP **0803**, 062 (2008) [arXiv:0712.3036 [hep-th]].

[19] R. Narayanan and H. Neuberger, Phys. Lett. B **616**, 76 (2005) [hep-lat/0503033].

[20] A. Hietanen, R. Narayanan, R. Patel and C. Prays, Phys. Lett. B **674**, 80 (2009) [arXiv:0901.3752 [hep-lat]].

[21] G. Bali, L. Castagnini, S. Collins, F. Bursa, L. Del Debbio, B. Lucini and M. Panero, PoS ConfinementX , 278 (2012) [arXiv:1302.1502 [hep-lat]].

[22] G. S. Bali, F. Bursa, L. Castagnini, S. Collins, L. Del Debbio, B. Lucini and M. Panero, JHEP **1306** (2013) 071 [arXiv:1304.4437 [hep-lat]].

[23] G. S. Bali, L. Castagnini, B. Lucini and M. Panero, PoS LATTICE **2013**, 100 (2014) [arXiv:1311.7559 [hep-lat]].

[24] E. Witten, Nucl. Phys. B **160**, 57 (1979).

[25] S. Coleman, "1/N, Aspects of Symmetry" Cambridge University Press (1985).

[26] A. V. Manohar, hep-ph/9802419.

[27] G. S. Adkins, C. R. Nappi and E. Witten, Nucl. Phys. B **228**, 552 (1983).

[28] E. E. Jenkins, Phys. Lett. B **315**, 441 (1993) [hep-ph/9307244].

[29] T. DeGrand, Phys. Rev. D **86**, 034508 (2012) [arXiv:1205.0235 [hep-lat]].

[30] M. Caselle, Int. J. Mod. Phys. A **15** (2000) 3901 [hep-th/0003119].

[31] R. G. Edwards and B. Joó [SciDAC Collaboration and LHPC Collaboration and UKQCD Collaboration], Nucl. Phys. Proc. Suppl. **140** (2005) 832 [arXiv:hep-lat/0409003].

[32] S. Güsken, Nucl. Phys. Proc. Suppl. **17** (1990) 361.

[33] M. Falcioni, M. L. Paciello, G. Parisi and B. Taglienti, Nucl. Phys. B **251** (1985) 624.

[34] C. Michael, Nucl. Phys. B **259** (1985) 58.

[35] M. Lüscher and U. Wolff, Nucl. Phys. B **339** (1990) 222.

[36] T. Burch et al. [Bern-Graz-Regensburg Collaboration], Phys. Rev. D **70** (2004) 054502 [hep-lat/0405006].

[37] A. Bode and H. Panagopoulos, Nucl. Phys. B **625** (2002) 198 [hep-lat/0110211].

[38] M. Lüscher and P. Weisz, Nucl. Phys. B **452** (1995) 234 [hep-lat/9505011].

[39] W. A. Bardeen, A. Duncan, E. Eichten, G. Hockney and H. Thacker, Phys. Rev. D **57** (1998) 1633 [hep-lat/9705008].

[40] V. Giménez, L. Giusti, F. Rapuano and M. Talevi, Nucl. Phys. B **531** (1998) 429 [hep-lat/9806006].

[41] S. R. Sharpe, Phys. Rev. D **46** (1992) 3146 [hep-lat/9205020].

[42] Y. Chen, S. J. Dong, T. Draper, I. Horvath, F. X. Lee, K. F. Liu, N. Mathur and J. B. Zhang, Phys. Rev. D **70** (2004) 034502 [hep-lat/0304005].

[43] W. A. Bardeen, A. Duncan, E. Eichten and H. Thacker, Phys. Rev. D **62** (2000) 114505 [hep-lat/0007010].

[44] M. Booth, G. Chiladze and A. F. Falk, Phys. Rev. D **55** (1997) 3092 [hep-ph/9610532].

[45] N. R. Constable and R. C. Myers, JHEP **9911** (1999) 020 [hep-th/9905081].

[46] J. Erdmenger, N. Evans, I. Kirsch and E. Threlfall, Eur. Phys. J. A **35**, 81 (2008) [arXiv:0711.4467 [hep-th]].

[47] W. A. Bardeen, A. Duncan, E. Eichten, N. Isgur and H. Thacker, Phys. Rev. D **65** (2001) 014509 [hep-lat/0106008].

[48] M. Göckeler, R. Horsley, H. Perlt, P. E. L. Rakow, G. Schierholz, A. Schiller and P. Stephenson, Phys. Rev. D **57** (1998) 5562 [hep-lat/9707021].

[49] M. Göckeler, R. Horsley, H. Oelrich, H. Perlt, D. Petters, P. E. L. Rakow, A. Schäfer and G. Schierholz et al., Nucl. Phys. B **544** (1999) 699 [hep-lat/9807044].

[50] A. Skouroupathis and H. Panagopoulos, Phys. Rev. D **76** (2007) 094514 [Erratum-ibid. D **78** (2008) 119901] [arXiv:0707.2906 [hep-lat]];

[51] A. Skouroupathis and H. Panagopoulos, Phys. Rev. D **79** (2009) 094508 [arXiv:0811.4264 [hep-lat]].

[52] M. Gell-Mann, R. J. Oakes and B. Renner, Phys. Rev. **175**, 2195 (1968).

[53] T. Eguchi and H. Kawai, Phys. Rev. Lett. **48** (1982) 1063.

[54] J. Kiskis, R. Narayanan and H. Neuberger, Phys. Lett. B **574** (2003) 65 [hep-lat/0308033].

[55] G. Colangelo and S. Dürr, Eur. Phys. J. C **33** (2004) 543 [hep-lat/0311023].

[56] G. Colangelo, A. Fuhrer and C. Haefeli, Nucl. Phys. Proc. Suppl. **153** (2006) 41 [hep-lat/0512002].

[57] J. R. Peláez and G. Ríos, Phys. Rev. Lett. **97** (2006) 242002 [hep-ph/0610397].

[58] L. S. Geng, E. Oset, J. R. Peláez and L. Roca, Eur. Phys. J. A **39** (2009) 81 [arXiv:0811.1941 [hep-ph]].

[59] J. Nieves and E. Ruiz Arriola, Phys. Rev. D **80** (2009) 045023 [arXiv:0904.4344 [hep-ph]].

[60] J. Nieves, A. Pich and E. Ruiz Arriola, Phys. Rev. D **84** (2011) 096002 [arXiv:1107.3247 [hep-ph]].

[61] T. Ledwig, J. Nieves, A. Pich, E. Ruiz Arriola and J. Ruiz de Elvira, Phys. Rev. D **90**, no. 11, 114020 (2014) [arXiv:1407.3750 [hep-ph]].

[62] S. Aoki, Y. Aoki, C. Bernard, T. Blum, G. Colangelo, M. Della Morte, S. D§rr and A. X. El Khadra *et al.*, Eur. Phys. J. C **74**, no. 9, 2890 (2014) [arXiv:1310.8555 [hep-lat]].

[63] S. Aoki *et al.* [CP-PACS Collaboration], Phys. Rev. D **67** (2003) 034503 [hep-lat/0206009].

[64] F. Butler, H. Chen, J. Sexton, A. Vaccarino and D. Weingarten, Nucl. Phys. B **430** (1994) 179 [hep-lat/9405003].

[65] L. Giusti, F. Rapuano, M. Talevi and A. Vladikas, Nucl. Phys. B **538**, 249 (1999) [hep-lat/9807014].

[66] C. McNeile, A. Bazavov, C. T. H. Davies, R. J. Dowdall, K. Hornbostel, G. P. Lepage and H. D. Trottier, Phys. Rev. D **87**, no. 3, 034503 (2013) [arXiv:1211.6577 [hep-lat]].

[67] T. Sakai and S. Sugimoto, Prog. Theor. Phys. **113** (2005) 843 [hep-th/0412141].

[68] K. Nakamura et al. [Particle Data Group Collaboration], J. Phys. G G **37** (2010) 075021.

[69] J. Babington, J. Erdmenger, N. J. Evans, Z. Guralnik and I. Kirsch, Phys. Rev. D **69** (2004) 066007 [hep-th/0306018].

[70] J. Erlich, E. Katz, D. T. Son and M. A. Stephanov, Phys. Rev. Lett. **95** (2005) 261602 [hep-ph/0501128].

[71] L. Da Rold and A. Pomarol, Nucl. Phys. B **721** (2005) 79 [hep-ph/0501218]; JHEP **0601** (2006) 157 [hep-ph/0510268].

[72] J. Gasser and H. Leutwyler, Annals Phys. **158** (1984) 142;

[73] J. Gasser and H. Leutwyler, Nucl. Phys. B **250** (1985) 465.

[74] H. Leutwyler, Annals Phys. **235** (1994) 165 [hep-ph/9311274].

[75] G. Ecker, Prog. Part. Nucl. Phys. **35** (1995) 1 [hep-ph/9501357].

[76] A. Pich, Rept. Prog. Phys. **58** (1995) 563 [hep-ph/9502366].

[77] S. Scherer and M. R. Schindler, hep-ph/0505265.

[78] M. Creutz, Phys. Rev. D **21**, 2308 (1980);

[79] K. Fabricius and O. Haan, Phys. Lett. B **143** (1984) 459.

[80] A. D. Kennedy and B. J. Pendleton, Phys. Lett. B **156**, 393 (1985).

[81] E. Pietarinen, Nucl. Phys. B **190** (1981) 349.

[82] N. Cabibbo and E. Marinari, Phys. Lett. B **119**, 387 (1982).

[83] S. L. Adler, Phys. Rev. D **23** (1981) 2901;

[84] F. R. Brown and T. J. Woch, Phys. Rev. Lett. **58** (1987) 2394.

[85] N. Cabibbo and E. Marinari, Phys. Lett. B **119**, 387 (1982).

[86] P. de Forcrand and O. Jahn, arXiv:hep-lat/0503041.

[87] M. J. Teper, Phys. Rev. D **59** (1999) 014512 [arXiv:hep-lat/9804008].

[88] U. Wolff [ALPHA Collaboration], Comput. Phys. Commun. **156** (2004) 143 [Erratum-ibid. **176** (2007) 383] [hep-lat/0306017].

[89] H. A. van der Vorst, SIAM J. Sci. Statist. Comput. **13**, 631 (1992) 140

[90] M. H. Gutknecht, SIAM J. Sci. Statist. Comput. **14**, 1020 (1993) 140, 141

[91] G. Martinelli, C. Pittori, C. T. Sachrajda, M. Testa and A. Vladikas, Nucl. Phys. B **445** (1995) 81 [hep-lat/9411010].

[92] M. Gockeler, R. Horsley, Y. Nakamura, H. Perlt, D. Pleiter, P. E. L. Rakow, A. Schafer and G. Schierholz *et al.*, Phys. Rev. D **82** (2010) 114511 [Erratum-ibid. D **86** (2012) 099903] [arXiv:1003.5756 [hep-lat]].

[93] M. Constantinou, M. Costa, M. Gockeler, R. Horsley, H. Panagopoulos, H. Perlt, P. E. L. Rakow and G. Schierholz *et al.*, arXiv:1303.6776 [hep-lat].

[94] J. -R. Cudell, A. Le Yaouanc and C. Pittori, Phys. Lett. B **454** (1999) 105 [hep-lat/9810058].

[95] C. Alexandrou, M. Constantinou, T. Korzec, H. Panagopoulos and F. Stylianou, Phys. Rev. D **86** (2012) 014505 [arXiv:1201.5025 [hep-lat]].

[96] L. Giusti, M. L. Paciello, C. Parrinello, S. Petrarca and B. Taglienti, Int. J. Mod. Phys. A **16** (2001) 3487 [hep-lat/0104012].

[97] C. T. H. Davies, G. G. Batrouni, G. R. Katz, A. S. Kronfeld, G. P. Lepage, K. G. Wilson, P. Rossi and B. Svetitsky, Phys. Rev. D **37** (1988) 1581.

[98] N. Cardoso, P. Bicudo, P. J. Silva and O. Oliveira, Acta Phys. Polon. Supp. **5** (2012) 1135 [arXiv:1208.1186 [hep-lat]].